



DEPARTMENT OF PHYSICS

UNIVERSITY OF CAPE TOWN

IYUNIVESITHI YASEKAPA • UNIVERSITEIT VAN KAAPSTAD

Search for tWZ production in the Full Run 2 ATLAS
dataset using events with four leptons

Jake Reich

Student Number: RCHJAK001

Supervisor: Dr. James Keaveney

Co-Supervisor: Dr. Sahal Yacoob

October 2021

Abstract

Declaration

I certify that this assignment/report is my own work, based on my personal study and/or research and that I have acknowledged all material and sources used in its preparation, whether they be books, articles, reports, lecture notes, and any other kind of document, electronic or personal communication. I also certify that this assignment/report has not previously been submitted for assessment in any other unit, except where specific permission has been granted from all unit coordinators involved, or at any other time in this unit, and that I have not copied in part or whole or otherwise plagiarised the work of other students and/or persons.

Acknowledgements

Contents

1	Introduction	7
2	Theory	8
2.1	Standard Model of Particle Physics	8
2.1.1	Electroweak Theory	8
2.1.2	Top Quark	8
2.2	tWZ	8
2.2.1	Tetra-lepton Channel	8
2.2.2	Comparison to Tri-lepton Channel	9
2.3	Effective Field Theory (EFT)	10
2.4	Machine Learning in the Context of Particle Physics Analyses	10
2.5	Statistical Techniques	10
2.5.1	Maximum Likelihood Fitting	10
2.5.2	p-value and χ^2	10
2.5.3	Significance	10
2.5.4	Limit Setting	10
3	The ATLAS Experiment and Detector	11
3.1	The ATLAS Experiment	11
3.1.1	Large Hadron Collider (LHC)	11
3.2	The ATLAS Detector	11
3.2.1	Coordinate System and Kinematics	11
3.2.2	Tracking Detectors	12
3.2.3	Calorimeter System	12
3.2.4	Muon Spectrometer	12
3.2.5	Trigger and Data Acquisition System	12
3.2.6	Particle Identification	12
4	Analysis Setup and Strategy	13
4.1	Data and Monte Carlo Simulation	13
4.1.1	Data Samples	13
4.1.2	Monte Carlo Samples	13
4.2	Objects	14
4.2.1	Leptons	15
4.2.2	Jets	16
4.2.3	b -tagging	16
4.3	Kinematic cuts	17
4.4	Regions and Event Selection	17
4.4.1	Optimization studies for event selection	18
4.5	Signal and Control Regions	20
4.5.1	tWZ OF SR	21
4.5.2	tWZ SF SR	22
4.5.3	$t\bar{t}Z$ CR	22
4.5.4	ZZb CR	28
4.5.5	$(tWZ)_{\text{fake}}$ CR	28

4.5.6	Fit Variables	29
4.6	Fake Lepton Estimation	29
4.7	Machine Learning Techniques	39
4.7.1	Object-level BDT	39
4.7.2	Event-level BDT	42
4.8	Two Neutrino Scanning Method (2ν SM) Algorithm	45
4.8.1	The algorithm	46
4.8.2	Calculating $w_{2\nu SM}$	46
4.8.3	Kinematic Veto	47
4.9	Systematics	50
4.9.1	Experimental uncertainties	50
4.9.2	Theoretical uncertainties	52
4.9.3	Generic shape systematics	53
4.10	Analysis Pipeline and TRexFitter	53
4.10.1	Fitting Procedure	54
4.11	Results	55
4.11.1	Tetralepton Channel	55
4.11.2	Trilepton and Tetralepton Channels	57
5	Conclusion and Outlook	62
A	Appendix	63
A.1	Pre-Fit Plots	63
A.1.1	tWZ OF SR	63
A.1.2	tWZ SF SR	70
A.1.3	$t\bar{t}Z$ CR	77
A.1.4	ZZb CR	84
A.1.5	$(tWZ)_{\text{fake}}$ CR	92

Chapter 1

Introduction

Write similar to what is in nrf application.

Talk about previous paper's (tWZ 3-lep) findings - <http://cds.cern.ch/record/2625170>

Explain that SM aims to describe fundamental physics, but fails in certain cases (DM, gravity etc.)

Possibly talk about EFT? Finding tWZ cross section - ζ , global fit. FOR REFERENCE:

The production of a single top quark in association with a W^\pm and Z boson ($tW^\pm Z$) is sensitive to both the neutral and charged electroweak couplings of the top quark as the process involves the simultaneous production of a W boson and a Z boson in association with the top quark. Due to the very large coupling of the top quark to the Higgs boson, the electroweak couplings of the top quark are a theoretically well-motivated area to expect the first signs of new physics. The recent lack of signs of new physics from LHC data tells us that new physics is either very heavy, or is very weakly coupled to Standard Model particles, therefore we might only observe signs of new physics in anomalous rates of well-chosen processes. A prime example of such a process is tWZ . This has an extremely low production cross section (0.7 fb), meaning that it is an extremely rare process to observe and subsequently, it has never been observed by any particle physics experiment. However, the latest datasets recorded by ATLAS are sufficiently large to allow a potential observation of this rare, novel process.

We aim to use the Full Run 2 dataset recorded by the ATLAS experiment at CERN to search for the production of a top quark together with a W^\pm and Z boson for the channel with four leptons (two originating from the decay of the Z boson, one from the associated W boson and one from the W boson which decays from the top quark (together with a b quark)). The Standard Model of particle physics has been confirmed to an extraordinary degree of precision, however we know there are stark deficiencies therein. These include its incompatibility with the theory of gravity and an explanation of the matter-antimatter asymmetry in the universe. Especially relevant is the Standard Model's lack of an explanation for the vast differences in the strengths of the fundamental forces (The Hierarchy Problem), constraining the electroweak couplings of the top quark squarely addresses this fundamental scientific question.

Chapter 2

Theory

2.1 Standard Model of Particle Physics

What is SM (renormalisable qft), come from symmetry, brief description of group structure? Explain structure/properties (fermions, bosons, etc.), coupling constants. 'Particles carry colour/electric charge, some particles can interact with others/themselves, some can't' Where does it how? How well does it work? Where doesn't it work?

2.1.1 Electroweak Theory

Properties of W and Z. Decay channels. Z as the standard candle (distinct OSSF lepton signal).

2.1.2 Top Quark

Properties. History (when/how was it discovered/theorised). Why interesting (large mass). Hierarchy problem. Decay channels. Extremely short lifetime (makes b's so important for top ID).

2.2 tWZ

2.2.1 Tetra-lepton Channel

The leading order Feynman diagram for tWZ in the tetra-lepton channel is shown below.

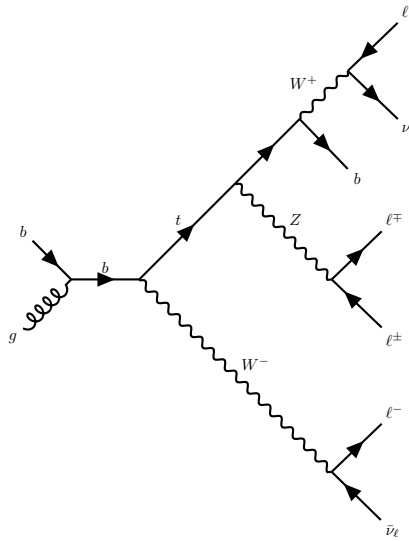


Figure 2.1: Example Feynman diagram of tWZ production in the tetra-lepton channel.

2.2.1.1 Backgrounds

The main backgrounds for tWZ (tetra-lepton channel) are the production of a two tops, both in the $\ell\nu b$ final state channel, together with a Z boson ($t\bar{t}Z$) and diboson production with fully leptonic final states (ZZ).

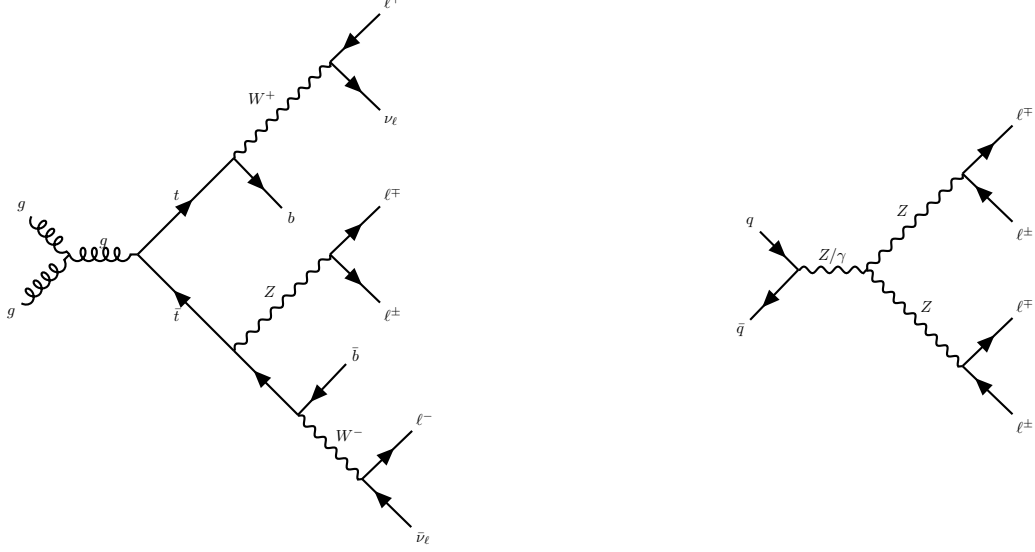


Figure 2.2: Example Feynman diagrams for $t\bar{t}Z$ (left) and ZZ (right) in the tetra-lepton channel.

$t\bar{t}Z$ contains four leptons and two b -quarks in its final state (inclusive $\sigma(t\bar{t}Z) = 0.95 \pm 0.08_{\text{stat}} \pm 0.10_{\text{syst}} \text{pb}$ at $\sqrt{s} = 13 \text{TeV}$ [2]) and can easily mimic the tWZ signal process, for instance, by one of its b -jets getting missed during detection. ZZ contains four leptons and zero b -quarks in its final state (inclusive $\sigma(ZZ) = 14.6^{+1.9}_{-1.8}(\text{stat})^{+0.5}_{-0.3}(\text{syst}) \pm 0.2(\text{theo}) \pm 0.4(\text{lumi}) \text{pb}$ at $\sqrt{s} = 13 \text{TeV}$ [29]). One way in which ZZ can mimic the tWZ signal process is by reconstruction of a non-prompt b -jet.

2.2.2 Comparison to Tri-lepton Channel

Less backgrounds to deal with (in tetralepton). However lower stats (in tetra). Give cross sections (and feynman diagram). Maybe talk a bit about analysis related challenges (trilepton has a hadronically decaying W , does this make the analysis easier or more difficult?).

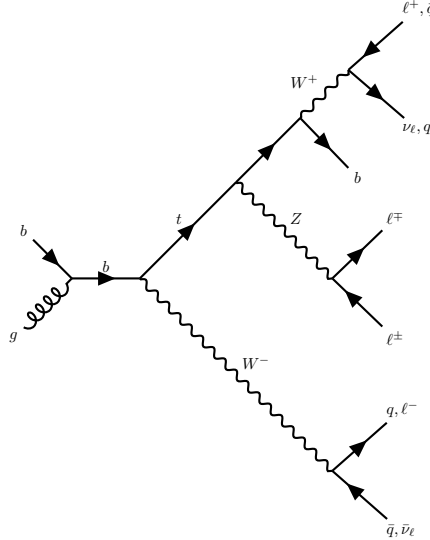


Figure 2.3: Example Feynman diagram of tWZ production in the tri-lepton channel.

The most apparent difference between the tri and tetra-lepton channels is the amount of statistics present, with the tetra-lepton channel having far less events in its phase space than that of the tri-lepton channel. The lack of statis-

tics in the tetra-lepton channel can be attributed to its low production cross section, $\sigma_{(tW^\pm Z).Br(4\ell)}^{\text{NLO}} = 0.7 \text{ fb}$ [34]. The tri-lepton channel has a production cross section ($\sigma_{(tW^\pm Z).Br(3\ell)}^{\text{NLO}} = 3.9 \text{ fb}$ [34]) around a factor of 4 larger than that of the tetra-lepton channel. This difference between the production cross section of the two decay channels can be largely attributed to the difference in branching ratios ($\frac{\Gamma_i}{\Gamma}$) between a hadronically decaying W boson, $\frac{\Gamma_{W \rightarrow \text{had}}}{\Gamma_W} = (67.41 \pm 0.27)\%$ [26], present in the tri-lepton channel and a leptonically decaying W boson, $\frac{\Gamma_{W \rightarrow \ell\nu}}{\Gamma_W} = (10.86 \pm 0.09)\%$ [26], present in the tetra-lepton channel.

Despite the tetralepton channel's low statistics, it is not subject to the large WZ background present in the trilepton channel. The tetralepton channel has a relatively large ZZ background (not present in the trilepton channel), fortunately this can be easily suppressed due to the full reconstructability of the two leptonically decaying Z -bosons.

2.3 Effective Field Theory (EFT)

Brief overview of EFT. What is EFT? Why important to pp as a whole? Why important in twz (high sensitivity to wilson coefficients, expected to have a large impact on global fit)? Similar to what james says in INT note.

2.4 Machine Learning in the Context of Particle Physics Analyses

Brief overview of ML as a whole; History; increase in popularity in recent years (why increased in popularity → novel techniques developed, increase in computing power for your buck). Where does it fit into pp (event selection, object reconstruction and ID (jet reco, b-tagging)). Explain concepts (vocabulary), overtraining, training, testing, classifier, classification. Why use x train/test ratio in pp (use some for analysis/use some for training)? Popular tools which are used today (scikit learn, TMVA, xgboost what is theano, what is keras).

Maybe a subsection on bdt (if end up using it) on the specific algorithm, and minimizing cost function (general). Explanation on ROC curve and why we can use it as a proxy to determine how well our bdt/nn is doing (and where it fails/can fail → things to be aware of cautious of when straight up using ROC integral (e.g. overtraining)).

2.5 Statistical Techniques

Brief overview: frequentist and bayes approach in general in pp, why we use frequentist in this analysis

2.5.1 Maximum Likelihood Fitting

Go through theory.

2.5.2 p-value and χ^2

Go through theory. Go through story of getting p-value, what it means, getting chi-squared, what it means, where the chi squared distribution comes in, degrees of freedom, what is a 'good' chi squared value and what is 'bad' and what do different values mean/infer/suggest.

2.5.3 Significance

Go through theory. What is means/interpreted as. 3 sigma evidence, 5 sigma discovery.

2.5.4 Limit Setting

Go through theory.

Chapter 3

The ATLAS Experiment and Detector

3.1 The ATLAS Experiment

ATLAS (A Toroidal LHC ApparatuS) is one of two general purpose detectors at CERN (the European Organization for Nuclear Research) near Geneva in Switzerland. These detectors collect data from the collisions provided by the worlds highest energy particle accelerator [[lhc-design-report](#)], the Large Hadron Collider (LHC) situated at CERN.

In this section, information about the LHC and the ATLAS detector are given. This includes technical aspects of the ATLAS detector and the processing of data into meaningful physics objects to be used in analyses.

3.1.1 Large Hadron Collider (LHC)

The LHC is a circular 27km particle accelerator located in an underground tunnel on the border between France and Switzerland. The accelerator consists of supercooled, superconducting magnets which accelerate and collide beams of protons at centre-of-mass energies up to $\sqrt{s} = 13\text{TeV}$ at instantaneous luminosities of $\mathcal{L} \sim 10^{34}\text{cm}^{-2}\text{s}^{-1}$. The LHC mainly produces these proton-proton collisions, however heavy-ion collisions can be produced (typically lasting a month, annually) which reach centre-of-mass energies of $\sqrt{s} = 5.02\text{TeV}/\text{nucleon}$ at instantaneous luminosities of $\mathcal{L} \sim 10^{27}\text{cm}^{-2}\text{s}^{-1}$. Proton-proton beams consist of bunches of protons which collide every 25ns, corresponding to a frequency of 40MHz.

Several accelerator systems are used to accelerate protons and heavy ions to such high energies. Protons are extracted from a tank of ionised hydrogen gas and are injected into the Linear Accelerator 2 (LINAC), where they are linearly accelerated to momenta of 50MeV. The proton bunches are then sequentially accelerated by a chain of circular accelerators. The chain starts with the Booster which accelerates the protons to momenta of up to 1.4GeV. The proton bunches are then fed through to the Proton Synchrotron (PS) and the Super Proton Synchrotron (SPS) which accelerate the protons to momenta of up to 25GeV and 450GeV respectively. The protons are then transferred to two beam pipes of the LHC where they travel in opposite directions. Both proton beams are accelerated to their final momenta of 6.5TeV, resulting in a centre-of-mass energy of 13TeV. These proton beams then collide at one of the four main interaction points situated along the LHC.

The four main experiments located at the interaction points are ATLAS, the Compact Muon Solenoid (CMS), Large Hadron Collider Beauty (LHCb) Experiment and A Large Ion Collider Experiment (ALICE). ATLAS and CMS are general-purpose detectors which investigate a wide range of physics processes. Since both ATLAS and CMS can measure the same processes, they are able to cross-check and validate measurements taken by one another. LHCb is specifically designed to study decays of particles containing b -quarks. ALICE is designed to study the strongly interacting quark-gluon plasma which is formed at extremely high energy densities.

At the interaction points, the two proton beams which consist of protons in closely packed bunches, travel in opposite directions to one another and collide. We are only able to study one $p - p$ collision (event) at a time, however many hard $p - p$ collisions can occur per bunch crossing. These additional collisions are referred to as

pile-up. Why pileup bad??? (hard to reconstruct.. etc..)

3.2 The ATLAS Detector

3.2.1 Coordinate System and Kinematics

Physical dimensions, properties (mass). Coordinate system. Definition of ΔR , η .

In the next subsections:

Where are different particles detected? How are they detected at each part of the detector? How well do the different parts detect the different particles and how do they take advantage of different particle properties each part wishes to detect in an engineering/physics perspective (e.g. why we WANT some particles to get detected at some parts of the detector and how we do this (by use of correct materials which interact specifically with those particles which we wish to measure and NOT with other particles))

3.2.2 Tracking Detectors

3.2.3 Calorimeter System

3.2.3.1 Electromagnetic Calorimeter

3.2.3.2 Hadronic Calorimeter

3.2.4 Muon Spectrometer

3.2.5 Trigger and Data Acquisition System

3.2.6 Particle Identification

Chapter 4

Analysis Setup and Strategy

4.1 Data and Monte Carlo Simulation

4.1.1 Data Samples

The pp collision data used in this analysis was collected with the ATLAS detector at the LHC from 2015 to 2018. This data period of data taking is referred to as Run 2. During this period, pp collisions at $\sqrt{s} = 13$ TeV, corresponding to an integrated luminosity (\mathcal{L}) of 156 fb^{-1} , were delivered by the LHC. The ATLAS detector managed to record 147 fb^{-1} of this total delivered data. 139 fb^{-1} of the data recorded by ATLAS is considered to be good enough for physics analyses (the data passes certain quality control criteria) and placed into the *Good Runs List* [25]. We use the Run 2 datasets from the Good Runs List, called `mc16a`, `mc16d` and `mc16e` with integrated luminosity's of 36.2 fb^{-1} , 44.3 fb^{-1} and 58.5 fb^{-1} respectively.

4.1.2 Monte Carlo Samples

Simulated Monte Carlo (MC) samples were generated and used to model the SM tWZ signal and its backgrounds.

The following background processes are considered:

- **$t\bar{t}Z$:** $t\bar{t}$ with an associated Z -boson, in the tetralepton final state. Therefore, both top-quarks decay leptonically (e.g. $t \rightarrow W^+ b \rightarrow \ell^+ \nu b$) and of these top-quarks emits a Z -boson which decays leptonically ($Z \rightarrow \ell^\pm \ell^\mp$ (OSSF lepton pair)). This results in a final state with 4 leptons and 2 b-quarks.
- **ZZ :** Diboson production with a tetralepton final state, therefore both Z -bosons decay leptonically ($Z \rightarrow \ell^\pm \ell^\mp$ (OSSF lepton pair)).
- **other:** Processes with a relatively minimal, but non-negligible background contribution
 - $VVV (V = W/Z)$
 - $t\bar{t}$
 - $t\bar{t}W$
 - $t\bar{t}WW$
 - $t\bar{t}H$
 - WZ
 - $t\bar{t}t$
 - $t\bar{t}t\bar{t}$
 - tZq

The MC simulations are achieved via the use of event generators and parton shower generators. Event generators simulate the pp collisions (hard events) by sampling the proton's Parton Distribution Functions (PDFs) at the desired energy scale. The parton shower generators simulate any incoming or outgoing particles from the hard

process, which carry QCD color charge and can therefore lead to parton showers.

The production of tWZ events is simulated with the **MADGRAPH5_AMC@NLO 2.3.3** generator providing matrix element (ME) calculations at NLO. The events are interfaced with **PYTHIA 8.235** for the parton shower.

The production of $t\bar{t}Z$ and $t\bar{t}W$ events are simulated with the **MADGRAPH5_AMC@NLO 2.3.3** generator providing ME calculations at NLO. The events are interfaced with **PYTHIA 8.210** for the parton shower.

Event generation of tWZ and $t\bar{t}Z$ results in diagrams which overlap with one another, that is, these diagrams contain the same initial and final state particles. Several methods exist in order to separate between the two processes, by removing the overlap, therefore avoiding double counting. There are two different diagram removal procedures, diagram removal procedure 1 (DR1) [22] and diagram removal procedure 2. We use the DR1 scheme to remove the overlap (interference) between tWZ and $t\bar{t}Z$.

Diboson processes which feature the three charged leptons and one neutrino or four charged lepton in their final states, such as WZ and ZZ , are simulated using **SHERPA 2.2.2** at NLO precision. The events are interfaced with **SHERPA** for the parton shower.

Fully leptonic triboson processes such as WWW , WWZ , WZZ , and ZZZ containing up to six leptons in their final states are simulated using **SHERPA 2.2.2** at NLO precision. The events are interfaced with **SHERPA** for the parton shower.

The production of $t\bar{t}$ events are simulated with the **POWHEG** generator providing ME calculations at NLO. The events are interfaced with **PYTHIA 8.210** for the parton shower.

The production of $t\bar{t}t$, $t\bar{t}t\bar{t}$ and $t\bar{t}WW$ are simulated using the **MADGRAPH5_AMC@NLO 2.2.2** generator at LO precision. The events are interfaced with **PYTHIA 8.186** for the parton shower.

The production of $t\bar{t}$ with an associated Higgs boson, $t\bar{t}H$, are generated using the **MADGRAPH5_AMC@NLO 2.6.0** generator at NLO precision. The events are showered using **PYTHIA 8.230**.

The production of $t\bar{t}$ events is simulated with the **POWHEG** generator providing ME calcualtions at NLO. The events are showered using **PYTHIA 8.230**.

The production of a single top quark in association with a Z -boson and an extra parton, tZq , is simulated using **MADGRAPH5_AMC@NLO 2.3.3** at NLO prescision. The events are interfaced with **PYTHIA 8.230** for the parton shower.

In Table 4.1, the event generator and parton shower used for each process's sample are shown.

4.2 Objects

In this section the physics objects (leptons, jets and b -tagged jets) used in this analysis are outlined.

Process	Event Generator	Cross section calculation	Parton Shower
tWZ	MADGRAPH5_AMC@NLO 2.3.3	NLO	PYTHIA 8.235
$t\bar{t}Z$	MADGRAPH5_AMC@NLO 2.3.3	NLO	PYTHIA 8.210
ZZ, WZ	SHERPA 2.2.2	NLO	SHERPA
$VVV (V = W/Z)$	SHERPA 2.2.2	NLO	SHERPA
$t\bar{t}$	POWHEG	NLO	PYTHIA 8.230
$t\bar{t}W$	MADGRAPH5_AMC@NLO 2.3.3	NLO	PYTHIA 8.210
$t\bar{t}WW$	MADGRAPH5_AMC@NLO 2.2.2	LO	PYTHIA 8.186
$t\bar{t}H$	MADGRAPH5_AMC@NLO 2.6.0	NLO	PYTHIA 8.230
$t\bar{t}t, t\bar{t}t\bar{t}$	MADGRAPH5_AMC@NLO 2.2.2	LO	PYTHIA 8.186
tZq	MADGRAPH5_AMC@NLO 2.3.3	NLO	PYTHIA 8.230

Table 4.1: The event generator and parton shower used for the signal and background process's MC samples is shown.

4.2.1 Leptons

In this analysis we only consider e and μ leptons, since τ leptons are difficult to detect in the ATLAS detector. τ leptons are challenging to detect since they have an extremely short lifetime (290.3 ± 0.5 fs [26]) which causes them to decay before reaching any detector components and therefore can only be reconstructed via their decay products.

In addition to our selection criteria of exactly four leptons, we require that the Leading (L), Next-to-Leading (NL), Next-to-Next-to-Leading (NNL) and Next-to-Next-to-Next-to-Leading (NNNL) leptons have p_T greater than 28, 10, 10 and 10 GeV respectively. Here we have chosen to apply relatively loose object-level cuts in an attempt to maximize our signal statistics, since the analysis is heavily statistically limited.

Reconstructed electrons are required to be within $|\eta| < 2.47$ and excluding the transition region between the barrel and end-cap calorimeters at $1.37 < |\eta| < 1.52$. Reconstructed muons are required to be within $|\eta| < 2.5$.

The transverse impact parameter, d_0 , is defined as the minimal spacial distance between the object's (here we are referring to leptons) trajectory and the primary vertex (the vertex associated with the p - p hard scatter). The longitudinal impact parameter, z_0 , is defined as the value of z of the point on the object's trajectory which determines d_0 . To ensure consistency between the lepton and the primary vertex, we require that $|\frac{d_0}{\sigma(d_0)}| < 5$, $|z_0 \sin \theta| < 0.5$ mm for electrons and $|\frac{d_0}{\sigma(d_0)}| < 3$, $|z_0 \sin \theta| < 0.5$ mm for muons, following the current recommendations [39].

To avoid instances where one detector signal can result in multiple different reconstructed objects, an overlap removal is applied which ignores all but one of these objects. We use the current recommended configuration [24].

Electrons are selected using a likelihood based discriminant [1] which takes measurements from the tracking system, calorimeter system and quantities derived from both the tracking and calorimeter system as input. Muons are selected using AnalysisBase's Muon Selection Tool [33].

Loose electrons are defined with the criteria above, using the `LooseAndBLayerLH` ($\sim 91\%$ selection efficiency for electrons with $E_T > 30$ GeV [23]) identification working point. Similarly, tight electrons are defined with the criteria above, using the `TightLH` ($\sim 80\%$ selection efficiency for electrons with $E_T > 30$ GeV [23]) identification working point. Both loose and tight muons use the `Medium` ($\sim 95\%$ selection efficiency [4]) identification working point.

Tight leptons additionally require that they are sufficiently isolated from other particles produced in the collision. This is done by defining a cone of radius $\Delta R = \sqrt{\Delta\eta^2 + \Delta\phi^2}$ around the particle of interest and summing the p_T of all the reconstructed particles surrounding the particle of interest, situated within the cone. A quantity, I_{rel} , is then defined as $I_{rel} = \frac{\sum p_T(\text{surrounding candidate})}{p_T(\text{candidate})}$, the ratio of this sum to the p_T of the lepton candidate. If this value is large, it is likely that the particle of interest originated from a jet (together with many other particles), whereas a prompt decay product resulting from the hard scatter will have little to no energy surrounding it ($I_{rel} \ll 1$). We use Analysis Base's `IsolationSelectionTool` with the `PLVTight` ($\sim 70\%$ efficiency [5]) and `PLVTight` ($\sim 70\%$ efficiency at $p_T = 30\text{ GeV}$ [20]) working points for tight electrons and tight muons respectively (following the current recommendations [37]).

In Table 4.2, a summary of the selection criteria for leptons is shown.

	Electrons		Muons	
	Tight	Loose	Tight	Loose
p_T cuts	$p_T(\ell_1, \ell_2, \ell_3, \ell_4) > (28, 18, 10, 10) \text{ GeV}$			
Overlap Removal	"recommended"			
η cuts	$ \eta(\ell_e) < 2.47$ excluding $1.37 < \eta(\ell_e) < 1.52$		$ \eta(\ell_\mu) < 2.5$	
Impact Parameters	$ \frac{d_0}{\sigma(d_0)} < 5$, $ z_0 \sin \theta < 0.5 \text{ mm}$		$ \frac{d_0}{\sigma(d_0)} < 3$, $ z_0 \sin \theta < 0.5 \text{ mm}$	
Identification WP	TightLH	LooseAndBLayerLH	Medium	Medium
Isolation WP	PLVTight	Not Used	PLVTight	Not Used

Table 4.2: A summary of the requirements applied for selecting tight and loose leptons (e, μ) is shown.

4.2.2 Jets

Jets are reconstructed from topological clusters using the anti- k_t algorithm. Topological clusters are groups of adjacent calorimeter cells which originate from *seed* cells. Seed cells are defined to contain at least 4 times the average amount of noise expected in the cell¹. All cells adjacent to the seed cell are grouped together given that the energy deposited within the cell is at least 2σ . This process is repeated until there are no adjacent cells which meet the above criteria. All adjacent cells to the cluster are then added, with no requirement on the energy deposited within these cells. We use the `AntiKt4EMFlowjets` ($\sim 97\%$ average efficiency with JVT (outlined in the subsequent paragraph) > 0.2 [39]) working point (following the current recommendations [39]).

The jet-vertex-tagger (JVT) and the forward jet-vertex-tagger (fJVT) are likelihood discriminant which aim to suppress pile-up jets. We use the `Medium` working point for the JVT and the fJVT (following the current recommendations [36]). We additionally require that jets have a JVT value greater than 0.5.

Jets are required to be within $p_T(\text{jet}) > 20\text{ GeV}$. We apply these looser p_T cuts in an attempt to increase our limited signal statistics. A forward jet is a signature of single top production, we therefore require jets to have $|\eta| < 4.5$ in order to include these forward jets.

4.2.3 b -tagging

The DL1r b -tagger [32] was used to identify jets as b -jets. The DL1r algorithm combines outputs from several low-level tagging algorithms using a Deep Neural Network and outputs the probability that a given input jet is identified as a b , c or light flavoured jet. We use different DL1r working points to identify b -jets in our event selection (See Section 4.4). The working points are defined based off a cut on the DL1r score corresponding to a b -jet tagging efficiency of 60%, 70%, 77% and 85%.

¹ σ : average noise in a given cell

Since we are heavily statistically limited, we aim to increase the amount of statistics in our regions. In an attempt to achieve this goal in the $t\bar{t}Z$ CR, b -tagged jets were placed under *tight* and *loose* definitions. A tight b -tagged jet is defined as a jet which passes the 77%, 70%, 65% or 60% DL1r b -tagger working point. A loose b -tagged jet is defined as a jet which passes 85% DL1r b -tagger working point, but not the 77%, 70%, 65% or 60% DL1r b -tagger working points. Different numbers (and definitions) of tight and loose b -tagged jets were tried in each region, with the final selection criteria being chosen which maximised the expected significance of $\sigma(tWZ)$ (See Section ??).

4.3 Kinematic cuts

The invariant mass of the OSSF lepton pair coming from the Z boson must equal the invariant mass of the Z boson, and noting that e,μ reconstruction and identification in the ATLAS detector has a high efficiency [Marchese:2688452], we can use these OSSF leptons to reconstruct Z bosons with relatively high confidence. We therefore define a Z candidate as an OSSF lepton pair with an invariant mass, m_{OSSF} , satisfying the condition, $|m_{\text{OSSF}} - m_Z| < 30 \text{ GeV}$, where $m(Z)$ is the nominal Z boson mass (91.1876 GeV [26]). We use this wider mass window to cover the full range of the $m(Z)$ distribution, in an attempt to increase the number of events which pass our baseline selections. Multiple Z candidates can be present in certain decay channels (e.g. $eeee$, $\mu\mu ee$, $\mu\mu\mu\mu$). In these cases, the Z candidate which has an invariant mass closest to the nominal Z boson mass is chosen.

In order to suppress potential fakes and quarkonia (low mass resonances such as J/ψ and upsilon) we require that all OSSF lepton pairs have an invariant mass, m_{OSSF} , greater than 10 GeV .

The final state lepton charges must sum to zero. We therefore require, $\sum_{i=1}^4 \text{charge}(\ell_i) = 0$.

4.4 Regions and Event Selection

We define two tWZ SRs, as opposed to one tWZ SR, in an attempt to suppress and constrain the ZZ background. We require that both tWZ SRs have exactly four tight leptons, exactly one Z -boson candidate, exactly one tight b -tagged jet (from the decay of the top quark) and greater than or equal to one jet. The two tWZ SR's differ by the flavours of their leptons which don't originate from the decay of a Z -boson (Non- Z leptons). The ZZ background has two Z -bosons which decay into a pair of OSSF lepton pairs, in order to mimic the tWZ signal. We take advantage of this to define a tWZ region rich in ZZ background and one with a minimal ZZ background component. This is done by requiring that one of the tWZ SRs has its two non- Z leptons to have opposite flavour and the other tWZ SR is required to have its non- Z leptons to have the same flavour. These two disjoint tWZ SRs are named tWZ OF SR and tWZ SF SR respectively. We therefore expect that the tWZ SF SR contains the majority of tWZ 's ZZ background events.

In order to check the modelling of the most dominant background components in our signal region, we have modified our selection criteria to define $t\bar{t}Z$ and ZZb control regions. The $t\bar{t}Z$ control region has the same requirement on the number of reconstructed Z boson candidates in the signal region (due to a commonality on the number of Z bosons present in both processes), however we require at least two jets and that exactly two of these jets are b -tagged (corresponding to the b -quark jets originating from the two top-quark decays). We choose to define a ZZb region, as opposed to a ZZ region, since the ZZ background present in the tWZ signal region contains exactly one b -tagged jet. Therefore defining a region with ZZ plus exactly one b -jet more closely resembles the ZZ background present in the signal region. In addition to this, mis-modelling of ZZ has been seen in other analyses [3, 21], further motivating the use of a ZZb control region over a ZZ CR. The ZZb CR requires exactly two Z boson candidates and exactly one b -tagged jet, resulting in an implicit requirement on the number of jets ($N_{\text{jet}} \geq 1$).

In order to constrain the fake lepton component contained within the $t\bar{t}Z$ sample, we define a $(tWZ)_{\text{fake}}$ CR which is as similar as possible to the tWZ CR but is enhanced in fakes. This is achieved by defining the $(tWZ)_{\text{fake}}$ CR

Baseline selections				
$N_\ell = 4$ $p_T(\ell_1, \ell_2, \ell_3, \ell_4) > (28, 10, 10, 10)$ GeV $p_T(\text{jet}) > 20$ GeV, $ \eta(\text{jet}) < 4.5$, $\text{jvt} > 0.5$ $ \eta(\ell_e) < 2.47$ excluding $1.37 < \eta(\ell_e) < 1.52$ $ \eta(\ell_\mu) < 2.5$ $\sum_{i=1}^4 \text{charge}(\ell_i) = 0$ All OSSF lepton pairs require $m_{\text{OSSF}} > 10$ GeV				
Regions				
tWZ OF SR	tWZ SF SR	$t\bar{t}Z$ CR	ZZb CR	$(tWZ)_{\text{fake}}$ CR
$N_\ell(\text{tight}) = 4$	$N_\ell(\text{tight}) = 4$	$N_\ell(\text{tight}) = 4$	$N_\ell(\text{tight}) = 4$	$N_\ell(\text{tight}) = 3$ $N_\ell(\text{loose and NOT tight}) = 1$
N_Z candidate = 1	N_Z candidate = 1	N_Z candidate = 1	N_Z candidate = 2	N_Z candidate = 1
$N_{\text{jet}} \geq 1$	$N_{\text{jet}} \geq 1$	$N_{\text{jet}} \geq 2$	$N_{\text{jet}} \geq 1$	$N_{\text{jet}} \geq 1$
$N_{\text{b-jet}}(\text{tight}) = 1$	$N_{\text{b-jet}}(\text{tight}) = 1$	$N_{\text{b-jet}}(\text{tight}) \geq 1$ $N_{\text{b-jet}}(\text{loose}) \geq 0$ $N_{\text{b-jet}}(\text{tight}) + N_{\text{b-jet}}(\text{loose}) = 2$	$N_{\text{b-jet}}(\text{tight}) = 1$	$N_{\text{b-jet}}(\text{tight}) = 1$
Opp. Flavour Non-Z leptons	Same Flavour Non-Z leptons	-	-	-

Table 4.3: A summary of the requirements applied for selecting events in the signal and control regions is shown.

to inherit the same selection criteria as the tWZ SRs however, in this case, we require exactly 3 tight leptons and exactly 1 loose (and NOT tight) lepton (since looser leptons are more likely to be fakes, compared to tighter leptons). A $(t\bar{t}Z)_{\text{fake}}$ CR (requiring exactly 3 tight leptons and exactly 1 loose (and NOT tight) lepton) was tried as an alternative to the $(tWZ)_{\text{fake}}$ CR, however a much larger suppression of fakes were observed in this region (compared to the $(tWZ)_{\text{fake}}$ CR). This suppression of fakes can be explained by the extra b -tagged jet requirement (exactly two b -tagged jets are required in the $t\bar{t}Z$ region, compared to exactly one in the tWZ SRs (See Table 4.3)) which causes suppression of fakes via the overlap removal procedure [24].

In Table 4.3, a summary of the final selection criteria and region definitions is shown.

4.4.1 Optimization studies for event selection

In order to find the selection criteria for jets and leptons which maximized sensitivity to the tWZ signal, studies were performed by plotting the expected significance (Z_μ^{exp}) and expected upper limit ($\mu_{\text{up}}^{\text{exp}}$) for different selection criteria. The fitting procedure as described in Section ?? was used to calculate the expected upper limits and expected significances in this study. The same selection criteria and regions defined in Table 4.3 was used (unless otherwise specified), except for the selection(s) which were being optimised in each case.

In Figure 4.1 the expected significance (Z_μ^{exp}) and expected upper limits ($\mu_{\text{up}}^{\text{exp}}$) for different $\eta(\text{jet})$ cuts are shown.

From Figure 4.1, we can see that the $\eta(\text{jet})$ cut which maximises the sensitivity of tWZ in the tetralepton channel is requiring that $\eta(\text{jet}) < 4.5$. This selection criteria was set for the $\eta(\text{jet})$ across all regions.

In Figure 4.2 the expected significance (Z_μ^{exp}) and expected upper limits ($\mu_{\text{up}}^{\text{exp}}$) for different $p_T(\text{jet})$ cuts are shown.

From Figure 4.2, we can see that the $p_T(\text{jet})$ cut which maximises the sensitivity of tWZ is requiring that $p_T(\text{jet}) > 20$ GeV. This selection criteria was set for the $p_T(\text{jet})$ across all regions.

In Figure 4.3 the expected significance (Z_μ^{exp}) and expected upper limits ($\mu_{\text{up}}^{\text{exp}}$) for a range of different configurations

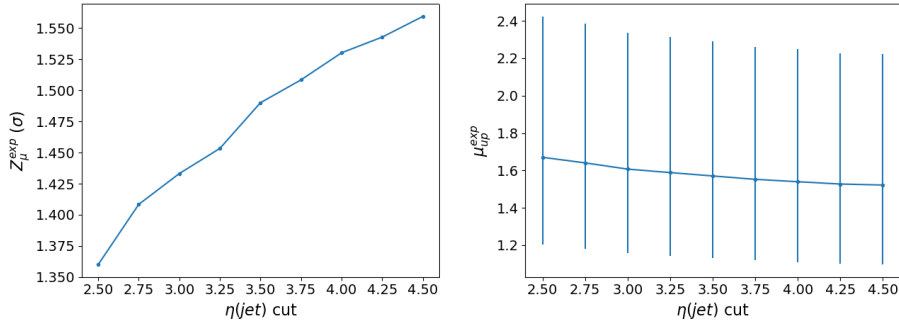


Figure 4.1: **Left:** Expected significance (Z_μ^{exp}) for different $\eta(jet)$ cuts is shown. The cuts applied on the $\eta(jet)$ are shown on the x-axis and corresponding expected significance from the likelihood fit is shown on the y-axis. **Right:** Expected upper limit (μ_{up}^{exp}) for different $\eta(jet)$ cuts is shown. The cuts applied on the $\eta(jet)$ are shown on the x-axis and corresponding expected upper limits are shown on the y-axis. Error bars representing the total uncertainty on the expected upper limits are shown as vertical lines.

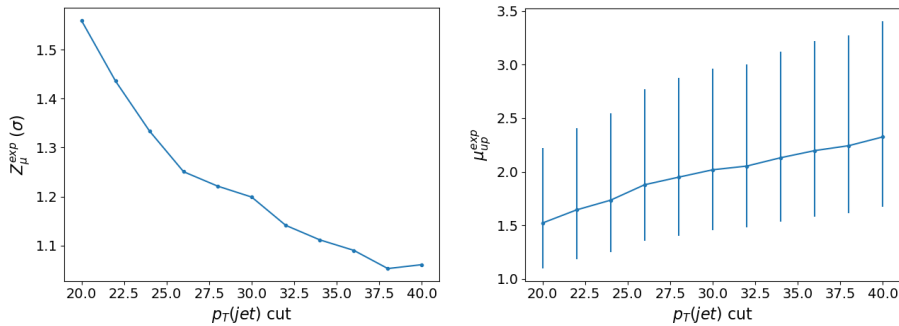


Figure 4.2: **Left:** Expected significance (Z_μ^{exp}) for different $p_T(jet)$ cuts is shown. The cuts applied on the $p_T(jet)$ are shown on the x-axis and corresponding expected significance from the likelihood fit is shown on the y-axis. **Right:** Expected upper limit (μ_{up}^{exp}) for different $p_T(jet)$ cuts is shown. The cuts applied on the $p_T(jet)$ are shown on the x-axis and corresponding expected upper limits are shown on the y-axis. Error bars representing the total uncertainty on the expected upper limits are shown as vertical lines.

of DL1r b -tagged jet working points across different regions.

From Figure 4.3, we can see that requiring that b -tagged jets pass the 77% DL1r WP in the tWZ SR, $(tWZ)_{fake}$ CR and the ZZb CR and that at least one b -tagged jet in the $t\bar{t}Z$ SR passes the 77% DL1r WP (the other jet is just required to pass the 85% DL1r WP) maximises the sensitivity overall (compared to the other investigated configurations). This configuration was chosen b -tagged jets.

The p_T (L Lepton) is constrained by the single lepton triggers (Table ??). We choose to apply a cut on the p_T (NL Lepton) slightly tighter than the tightest single lepton p_T cut in the trigger. We can however, try optimising the p_T (NL Lepton) cut by comparing the expected significance and limit for a range of p_T (NL Lepton) cuts to determine the cut which maximizes sensitivity.

In Figure 4.4 the expected significance (Z_μ^{exp}) and expected upper limits (μ_{up}^{exp}) for different p_T (NL Lepton) cuts is shown.

Since there is a very small change between the different p_T (NL Lepton) cuts on the sensitivity of tWZ , we choose to apply a p_T (NL Lepton) cut at 18 GeV, therefore applying a cut above the trigger p_T cut to suppress any systematic from the modelling of the trigger efficiency.

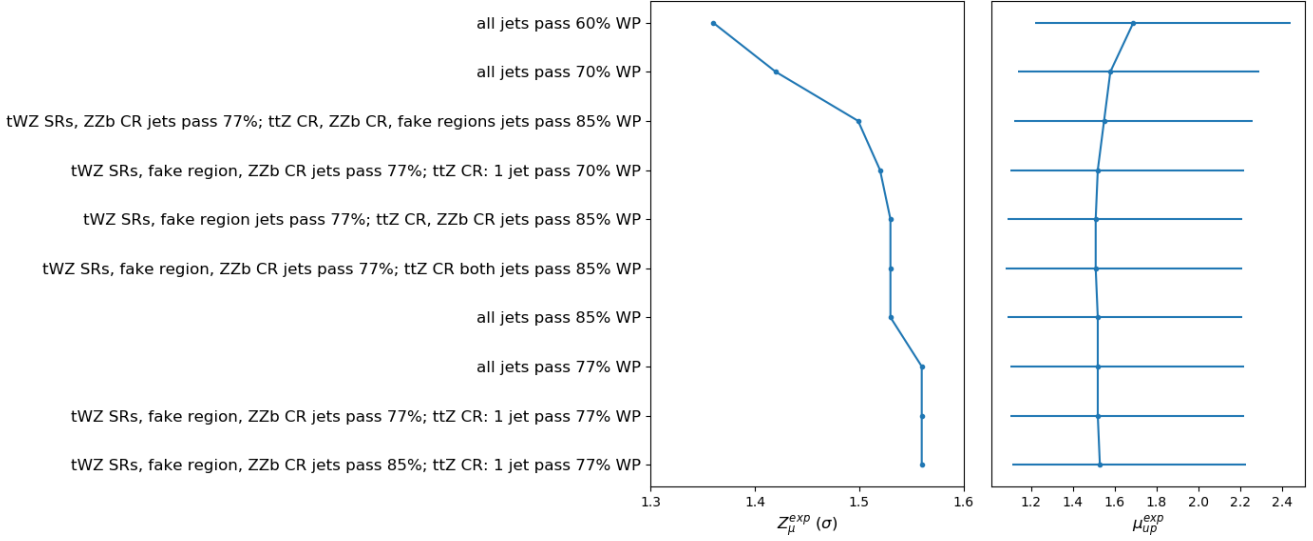


Figure 4.3: Expected significance (Z_μ^{exp}) and expected upper limit ($\mu_{\text{up}}^{\text{exp}}$) for different configurations of DL1r b -tagged jet working points is shown. The common y-axis shows the different configurations of DL1r b -tagged jet working points. On the left panel, the expected significance from the likelihood fit is shown on the x-axis. On the right panel, the expected upper limit from the likelihood fit is shown on the x-axis (with the corresponding total uncertainty represented by horizontal lines).

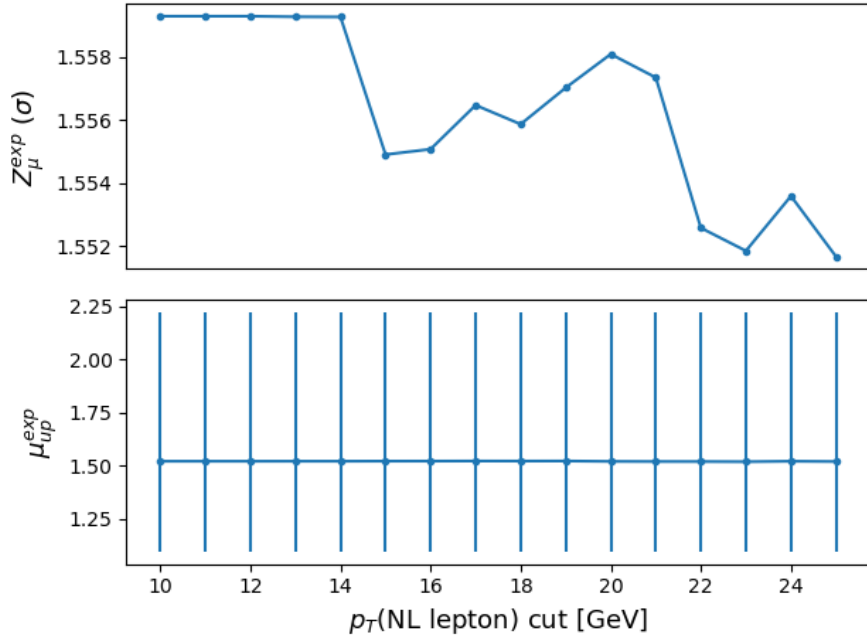


Figure 4.4: Expected significance (Z_μ^{exp}) and expected upper limit ($\mu_{\text{up}}^{\text{exp}}$) for different p_T (NL Lepton) cuts is shown. The common x-axis shows cut applied to the p_T of the next-to-leading lepton. On the top panel, the expected significance from the likelihood fit is shown on the y-axis. On the bottom panel, the expected upper limit from the likelihood fit is shown on the y-axis (with the corresponding total uncertainty represented by vertical lines).

4.5 Signal and Control Regions

In this section, pre-fit distributions of variables in each region are shown. More pre-fit distributions for each region are shown in the appendix (Section A.1). For each figure in this section, the data is given by the black points and

the MC predictions for each process are given by the histograms. The vertical lines on the data points represent the total uncertainty in the data and the diagonal lined bands represent the total MC uncertainty. The lower panel in each plot shows the ratios of the data to the theoretical predictions. The plots in the tWZ OF SR and tWZ SF SR are kept blinded by omitting the data points.

In Table 4.4, the pre-fit yields for each sample in each region is shown.

	tWZ OF SR	tWZ SF SR	tZ CR	ZZb CR	(tWZ) fake CR
$t\bar{t}Z$	13.9325 ± 1.84643	10.1343 ± 1.36039	31.7149 ± 4.46776	5.26303 ± 0.696828	19.1224 ± 2.50011
$t\bar{t}Z$ fakes	0.0687541 ± 0.0482172	0.032827 ± 0.026286	0.0709734 ± 0.043509	0.0474576 ± 0.0301512	4.94775 ± 2.48939
tWZ	3.81359 ± 0.392241	2.57584 ± 0.326401	2.61991 ± 0.861557	1.4023 ± 0.156686	4.93485 ± 0.692143
ZZ	0.546045 ± 0.18975	8.76232 ± 2.66871	1.22357 ± 0.376889	46.0616 ± 13.9203	7.76724 ± 2.36894
other	$t\bar{t}$	$6e-06 \pm 3.04506e-06$	0.250783 ± 0.44226	0.269883 ± 0.223373	$6e-06 \pm 3.04506e-06$
	tZq	0.0827265 ± 0.0399222	0.0757694 ± 0.0355101	0.0637132 ± 0.0293762	0.0590199 ± 0.0244576
	$t\bar{t}W$	$0.00674747 \pm 0.00793546$	$0.00279491 \pm 0.00287747$	$6e-06 \pm 3.04506e-06$	$0.00221727 \pm 0.00562041$
	WZ	0.0439316 ± 0.0241635	0.0397876 ± 0.0154764	0.0134837 ± 0.0128327	0.0474188 ± 0.0330635
	$t\bar{t}t$	$0.000987429 \pm 0.000768187$	$0.00249801 \pm 0.00138007$	0.0141085 ± 0.00486102	$6e-06 \pm 3.04506e-06$
	$t\bar{t}t\bar{t}$	0.00934516 ± 0.0080725	0.0107503 ± 0.00852049	0.0570846 ± 0.0206271	$6e-06 \pm 3.04506e-06$
	$t\bar{t}WW$	0.0293456 ± 0.0263573	0.0296011 ± 0.0196075	0.26412 ± 0.0936908	0.013096 ± 0.0323943
	$VVV(V = W/Z)$	0.280384 ± 0.0866421	0.191257 ± 0.0595588	0.0696624 ± 0.0228108	0.171171 ± 0.0526519
	$t\bar{t}H$	0.854064 ± 0.177974	0.674566 ± 0.141771	1.98187 ± 0.406211	0.151447 ± 0.0357703
Total		19.6684 ± 1.95158	22.7832 ± 3.10338	38.3633 ± 4.6342	53.2187 ± 13.9618
data	-	-	36	49	57

Table 4.4: The pre-fit yields for each sample in each region is shown.

4.5.1 tWZ OF SR

In this section, pre-fit distributions of variables in the tWZ OF SR are shown. More pre-fit distributions for the tWZ OF SR are shown in the appendix (Section A.1.1).

In Figure A.1 MC predictions for p_T , η and ϕ for leading (L) leptons and next-to-leading (NL) leptons in the tWZ OF SR region is shown.

In Figure 4.6 MC predictions for p_T , η and ϕ for leading (L) jets and next-to-leading (NL) jets in the tWZ OF SR region is shown.

In Figure 4.7 MC predictions for p_T , η and ϕ of the next-to-next-to-leading (NNL) jets, H_T (scalar sum of Jet p_T) and the Number of jets in the tWZ OF SR region is shown.

In Figure 4.8 MC predictions for p_T , η and ϕ of the leading b-tagged jets, the scalar sum of b-tagged jet p_T and the Number of b-tagged jets in the tWZ OF SR region is shown.

4.5.2 tWZ SF SR

In this section, pre-fit distributions of variables in the tWZ SF SR are shown. More pre-fit distributions for the tWZ SF SR are shown in the appendix (Section A.1.2).

In Figure A.14 MC predictions for p_T , η and ϕ for leading (L) leptons and next-to-leading (NL) leptons in the tWZ SF SR region is shown.

In Figure 4.10 MC predictions for p_T , η and ϕ for leading (L) jets and next-to-leading (NL) jets in the tWZ SF SR region is shown.

In Figure 4.11 MC predictions for p_T , η and ϕ of the next-to-next-to-leading (NNL) jets, H_T (scalar sum of Jet p_T) and the Number of jets in the tWZ SF SR region is shown.

In Figure 4.12 MC predictions for p_T , η and ϕ of the leading b-tagged jets, the scalar sum of b-tagged jet p_T and the Number of b-tagged jets in the tWZ SF SR region is shown.

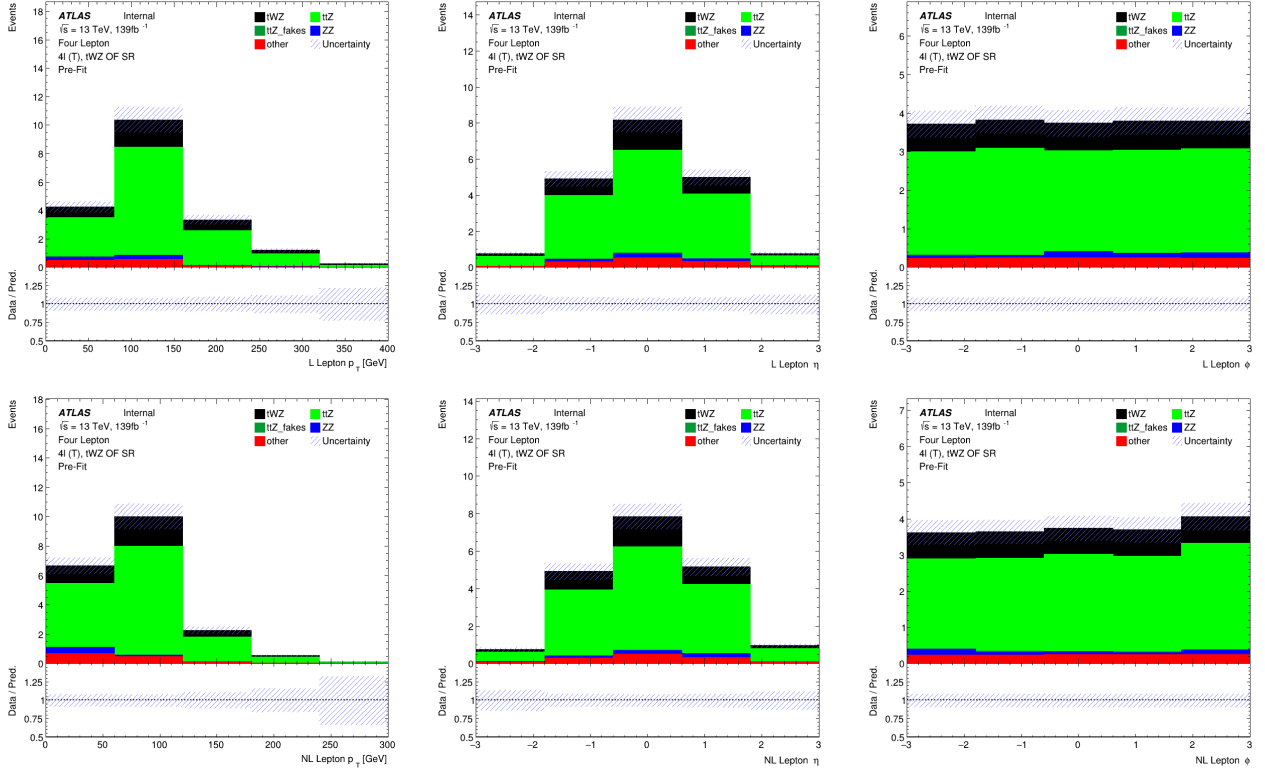


Figure 4.5: MC predictions for p_T , η and ϕ for leading (L) leptons (top row) and next-to-leading (NL) leptons (bottom row) in the tWZ OF SR region (*blinded*) is shown.

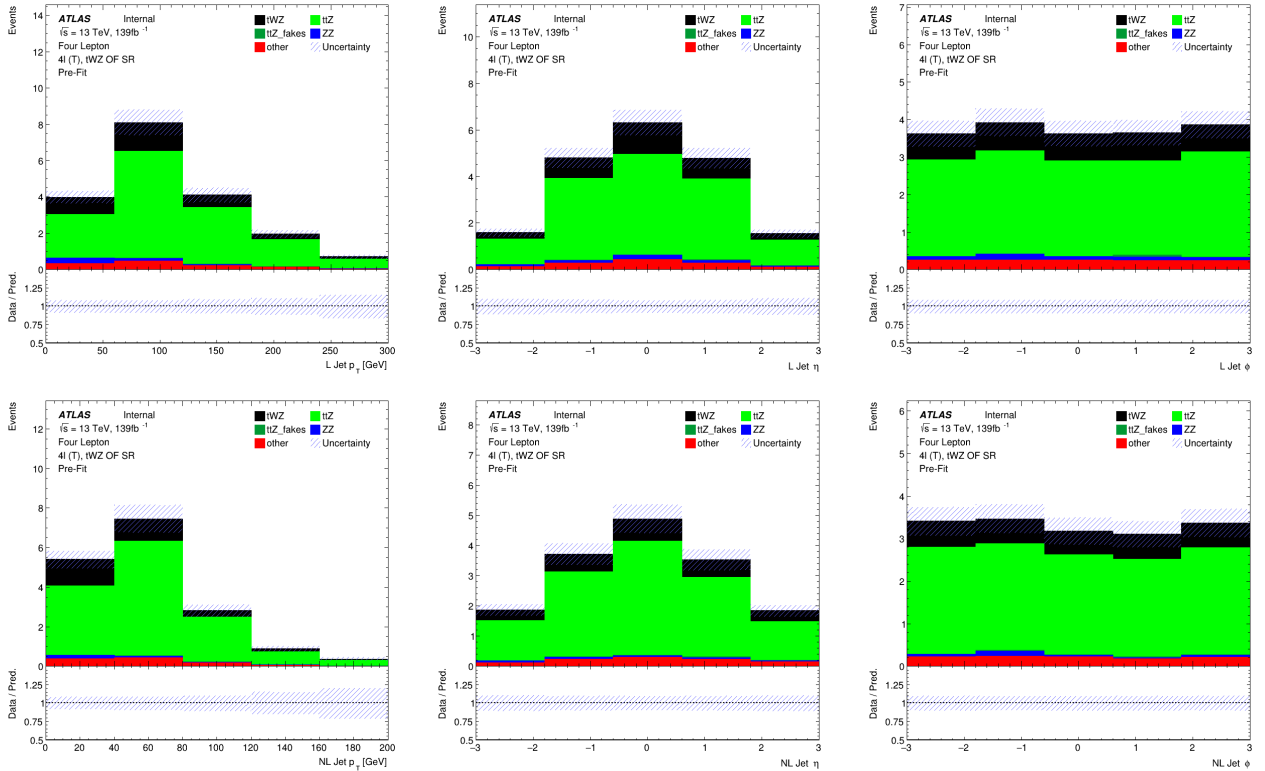


Figure 4.6: MC predictions for p_T , η and ϕ for leading (L) jets (top row) and next-to-leading (NL) jets (bottom row) in the tWZ OF SR region (*blinded*) is shown.

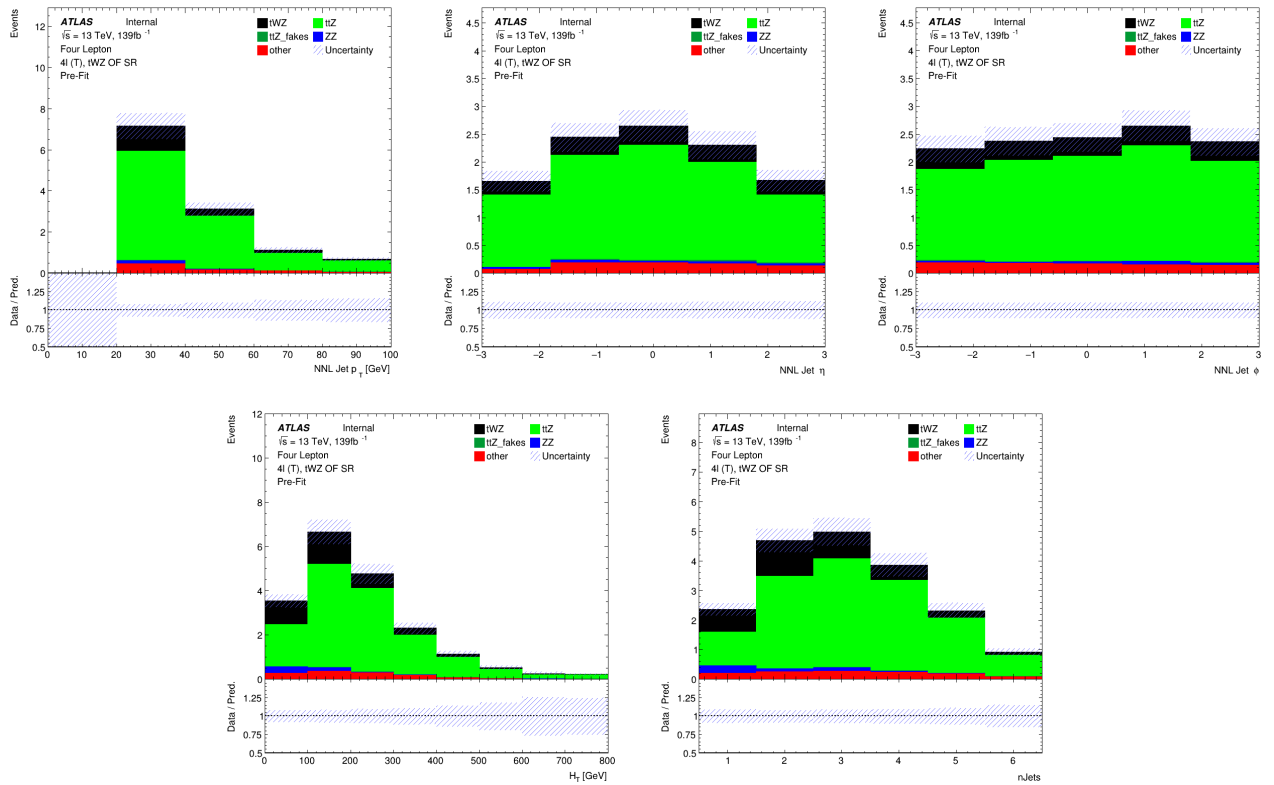


Figure 4.7: **Top row:** MC predictions for p_T , η and ϕ for next-to-next-to-leading (NNL) jets in the tWZ OF SR region (*blinded*) is shown. **Bottom row:** MC predictions for H_T (scalar sum of Jet p_T) (left) and the Number of jets (right) in the tWZ OF SR region (*blinded*) is shown.

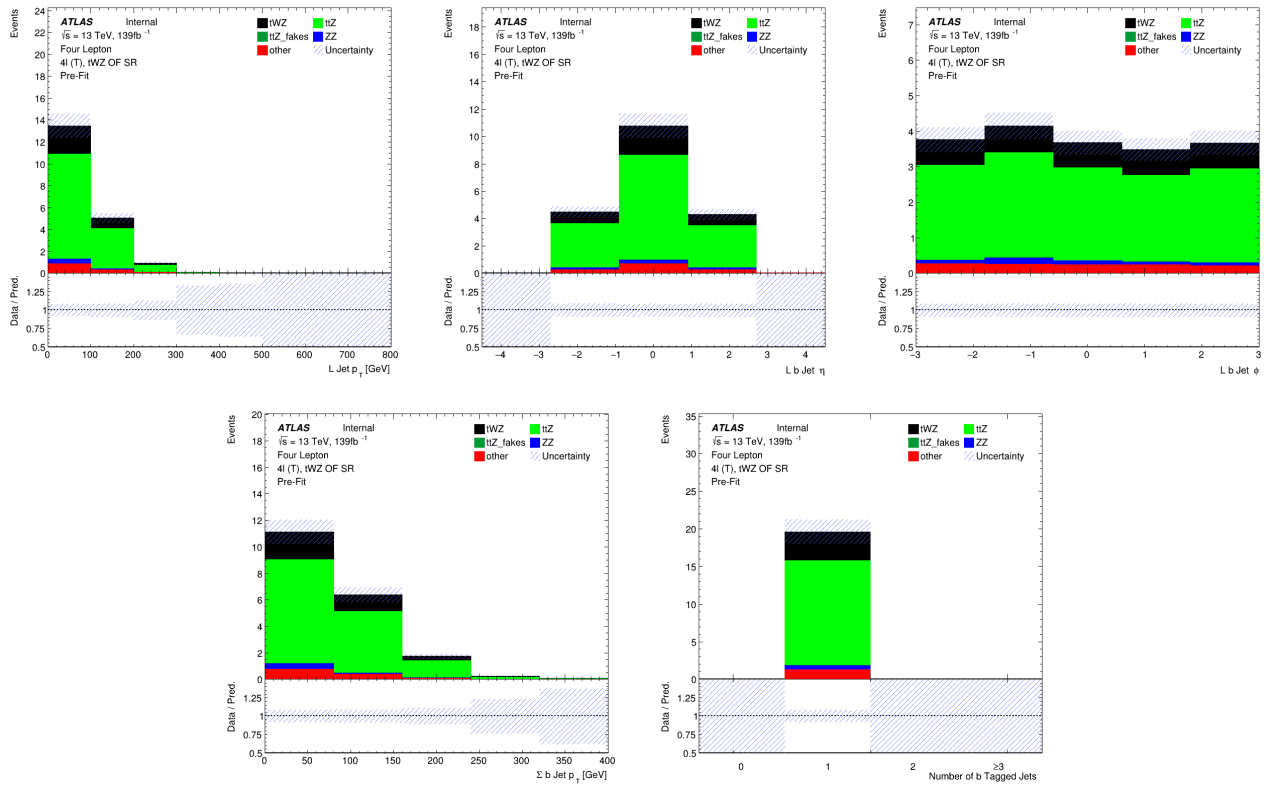


Figure 4.8: **Top row:** MC predictions for p_T , η and ϕ for leading b-tagged jets in the tWZ OF SR region (*blinded*) is shown. **Bottom row:** MC predictions for the scalar sum of b-tagged jet p_T (left) and the Number of b-tagged jets (right) in the tWZ OF SR region (*blinded*) is shown.

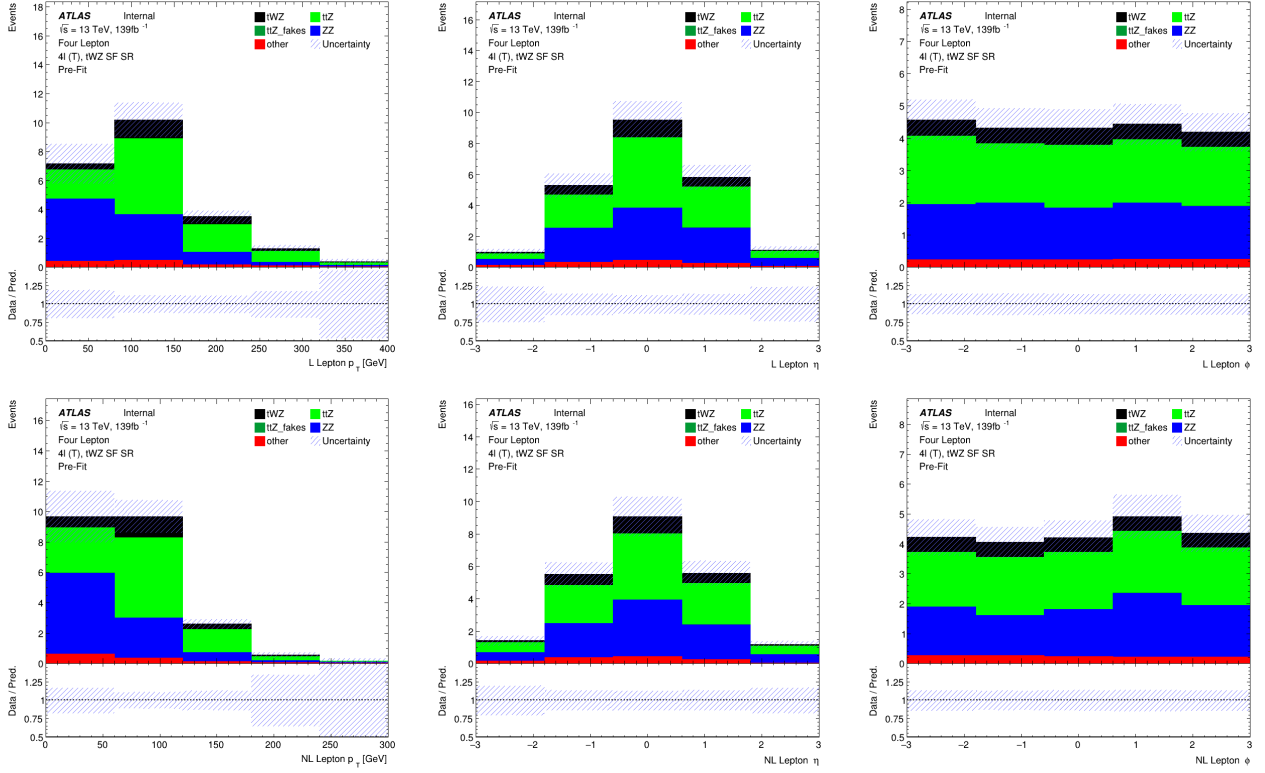


Figure 4.9: MC predictions for p_T , η and ϕ for leading (L) leptons (top row) and next-to-leading (NL) leptons (bottom row) in the tWZ SF SR region (*blinded*) is shown.

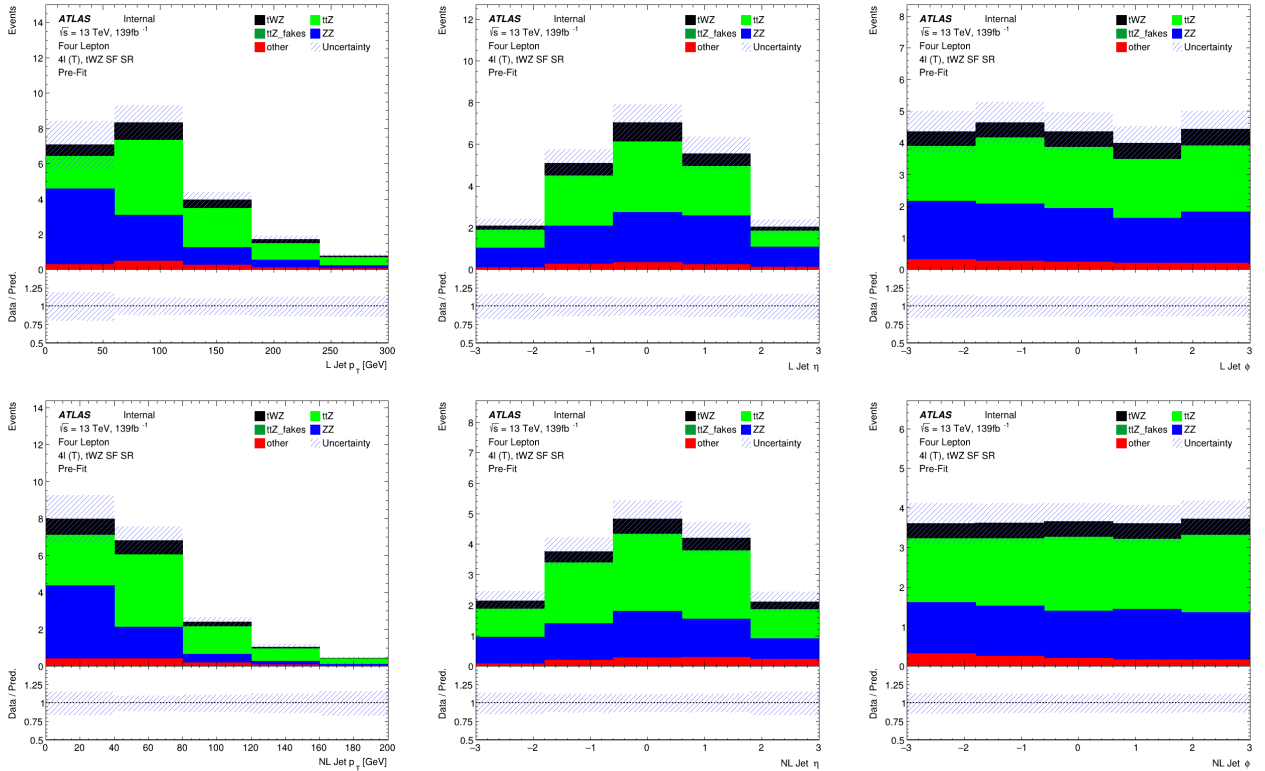


Figure 4.10: MC predictions for p_T , η and ϕ for leading (L) jets (top row) and next-to-leading (NL) jets (bottom row) in the tWZ SF SR region (*blinded*) is shown.

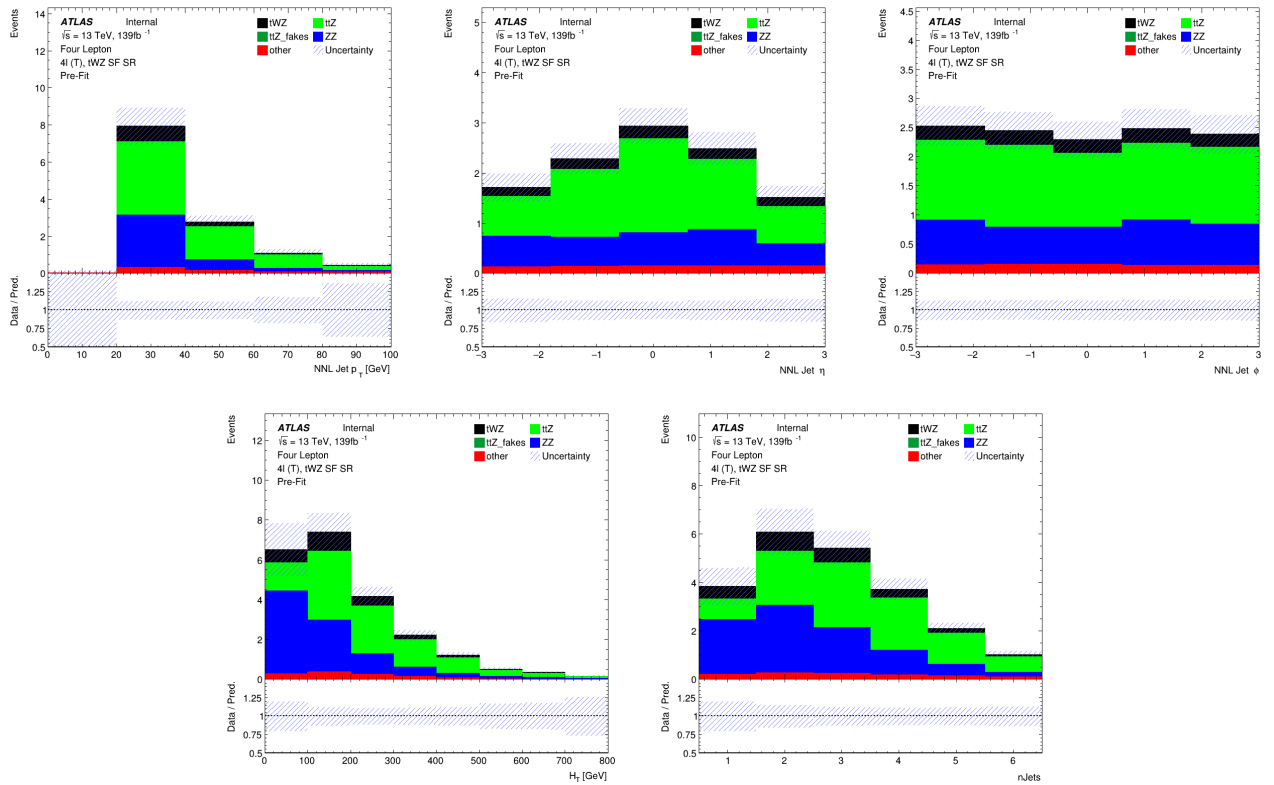


Figure 4.11: **Top row:** MC predictions for p_T , η and ϕ for next-to-next-to-leading (NNL) jets in the tWZ SF SR region (*blinded*) is shown. **Bottom row:** MC predictions for H_T (scalar sum of Jet p_T) (left) and the Number of jets (right) in the tWZ SF SR region (*blinded*) is shown.

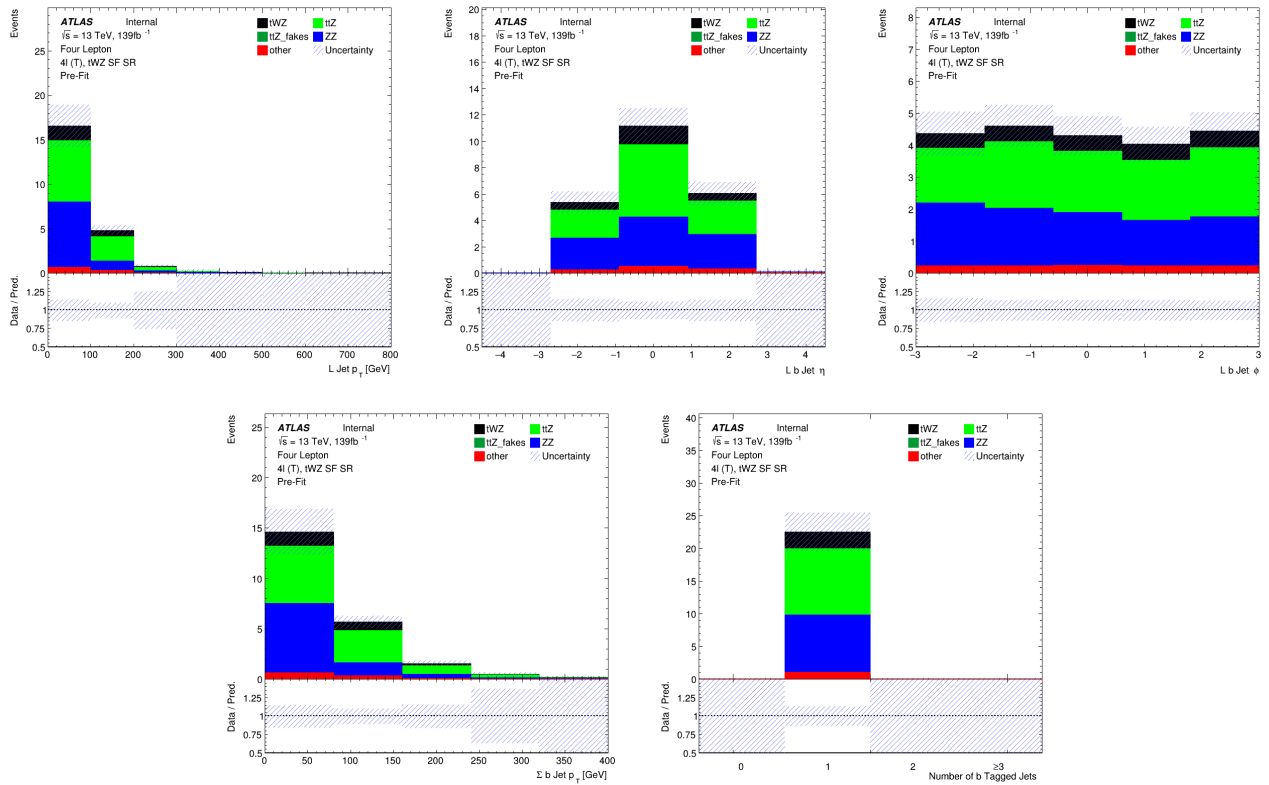


Figure 4.12: **Top row:** MC predictions for p_T , η and ϕ for leading b-tagged jets in the tWZ SF SR region (*blinded*) is shown. **Bottom row:** MC predictions for the scalar sum of b-tagged jet p_T (left) and the Number of b-tagged jets (right) in the tWZ SF SR region (*blinded*) is shown.

4.5.3 $t\bar{t}Z$ CR

In this section, pre-fit distributions of variables in the $t\bar{t}Z$ CR are shown. More pre-fit distributions for the $t\bar{t}Z$ CR are shown in the appendix (Section A.1.3).

In Figure A.27 MC predictions for p_T , η and ϕ for leading (L) leptons and next-to-leading (NL) leptons in the $t\bar{t}Z$ CR region is shown.

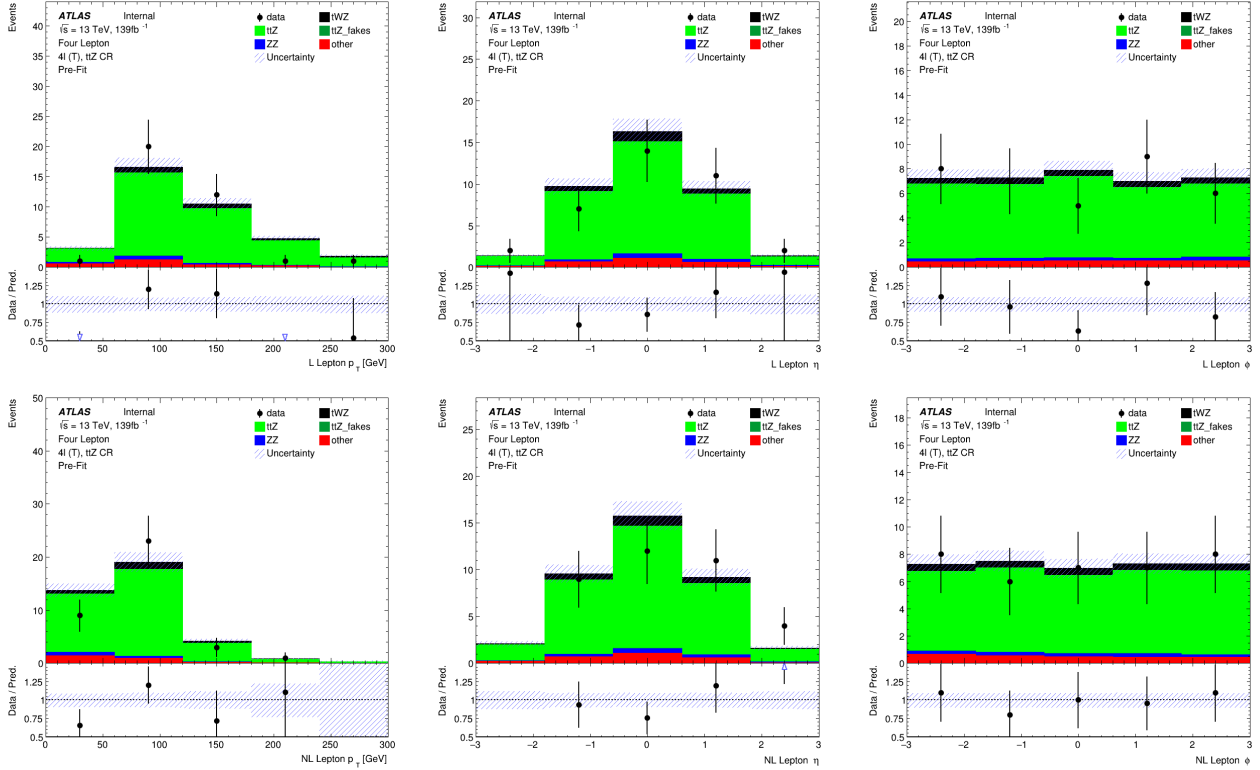


Figure 4.13: MC predictions for p_T , η and ϕ for leading (L) leptons (top row) and next-to-leading (NL) leptons (bottom row) in the $t\bar{t}Z$ CR region (*blinded*) is shown.

In Figure 4.14 MC predictions for p_T , η and ϕ for leading (L) jets and next-to-leading (NL) jets in the $t\bar{t}Z$ CR region is shown.

In Figure 4.15 MC predictions for p_T , η and ϕ of the next-to-next-to-leading (NNL) jets, H_T (scalar sum of Jet p_T) and the Number of jets in the $t\bar{t}Z$ CR region is shown.

In Figure 4.16 MC predictions for p_T , η and ϕ of the leading b-tagged jets, the scalar sum of b-tagged jet p_T and the Number of b-tagged jets in the $t\bar{t}Z$ CR region is shown.

4.5.4 ZZb CR

In this section, pre-fit distributions of variables in the ZZb CR are shown. More pre-fit distributions for the ZZb CR are shown in the appendix (Section A.1.4).

In Figure A.41 MC predictions for p_T , η and ϕ for leading (L) leptons and next-to-leading (NL) leptons in the ZZb CR region is shown.

In Figure 4.18 MC predictions for p_T , η and ϕ for leading (L) jets and next-to-leading (NL) jets in the ZZb CR region is shown.

In Figure 4.19 MC predictions for p_T , η and ϕ of the next-to-next-to-leading (NNL) jets, H_T (scalar sum of Jet p_T) and the Number of jets in the ZZb CR region is shown.

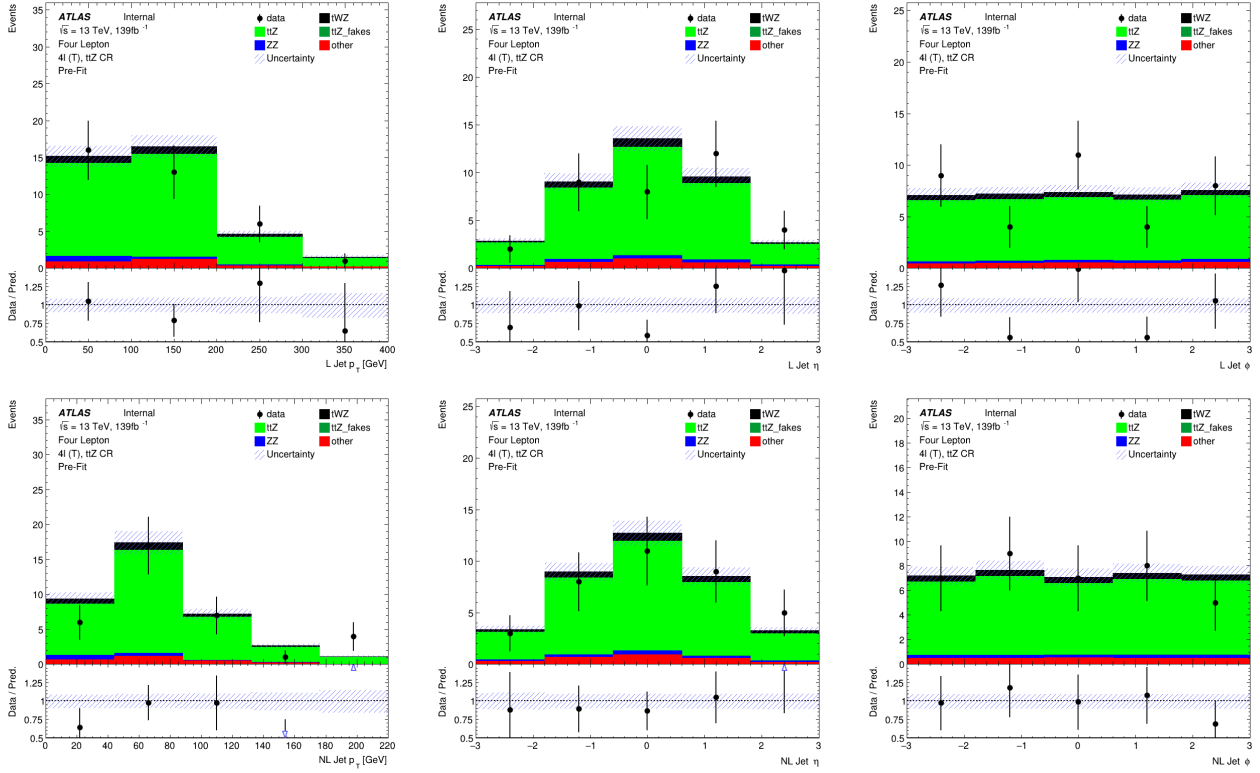


Figure 4.14: MC predictions for p_T , η and ϕ for leading (L) jets (top row) and next-to-leading (NL) jets (bottom row) in the $t\bar{t}Z$ CR region (*blinded*) is shown.

In Figure 4.20 MC predictions for p_T , η and ϕ of the leading b-tagged jets, the scalar sum of b-tagged jet p_T and the Number of b-tagged jets in the ZZb CR region is shown.

4.5.5 $(tWZ)_{\text{fake}}$ CR

In this section, pre-fit distributions of variables in the $(tWZ)_{\text{fake}}$ CR are shown. More pre-fit distributions for the $(tWZ)_{\text{fake}}$ CR are shown in the appendix (Section ??).

In Figure 4.21 MC predictions for p_T , η and ϕ for leading (L) leptons and next-to-leading (NL) leptons in the $(tWZ)_{\text{fake}}$ CR region is shown.

In Figure 4.22 MC predictions for p_T , η and ϕ for leading (L) jets and next-to-leading (NL) jets in the $(tWZ)_{\text{fake}}$ CR region is shown.

In Figure 4.23 MC predictions for p_T , η and ϕ of the next-to-next-to-leading (NNL) jets, H_T (scalar sum of Jet p_T) and the Number of jets in the $(tWZ)_{\text{fake}}$ CR region is shown.

In Figure 4.24 MC predictions for p_T , η and ϕ of the leading b-tagged jets, the scalar sum of b-tagged jet p_T and the Number of b-tagged jets in the $(tWZ)_{\text{fake}}$ CR region is shown.

Given the limited statistics which we are presented with in the tetralepton channel, we nevertheless observe relatively good agreement overall between data and MC.

4.6 Fake Lepton Estimation

Fake leptons are objects reconstructed as leptons, but do not correspond to the leptons which we are interested in our analysis. Fake leptons can be split up into two main categories, irreducible (prompt) fakes and reducible (non-prompt) fakes. Irreducible fakes are true leptons which do not come from the process of interest. Reducible fakes are objects which are mis-identified or incorrectly reconstructed as leptons. In the ATLAS detector, the probability for a fake to occur is very low.

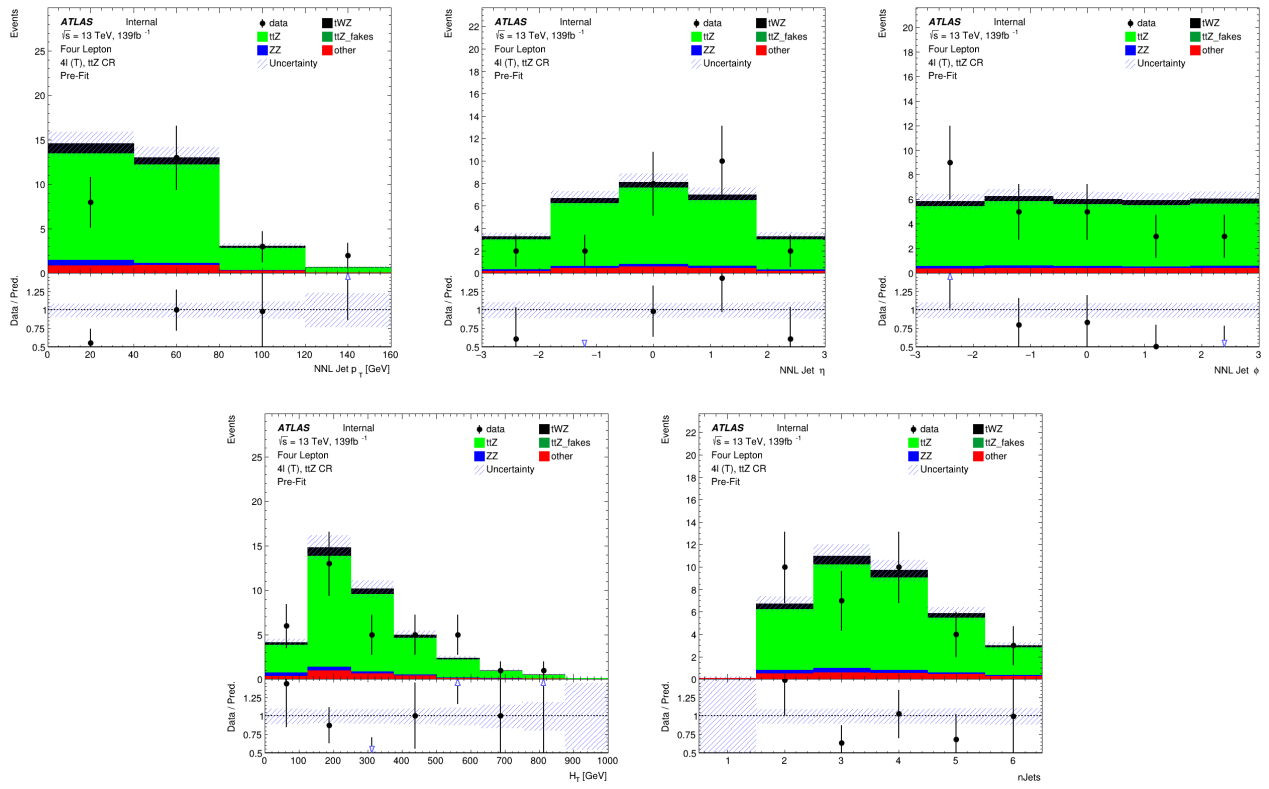


Figure 4.15: **Top row:** MC predictions for p_T , η and ϕ for next-to-next-to-leading (NNL) jets in the $t\bar{t}Z$ CR region (*blinded*) is shown. **Bottom row:** MC predictions for H_T (scalar sum of Jet p_T) (left) and the Number of jets (right) in the $t\bar{t}Z$ CR region (*blinded*) is shown.

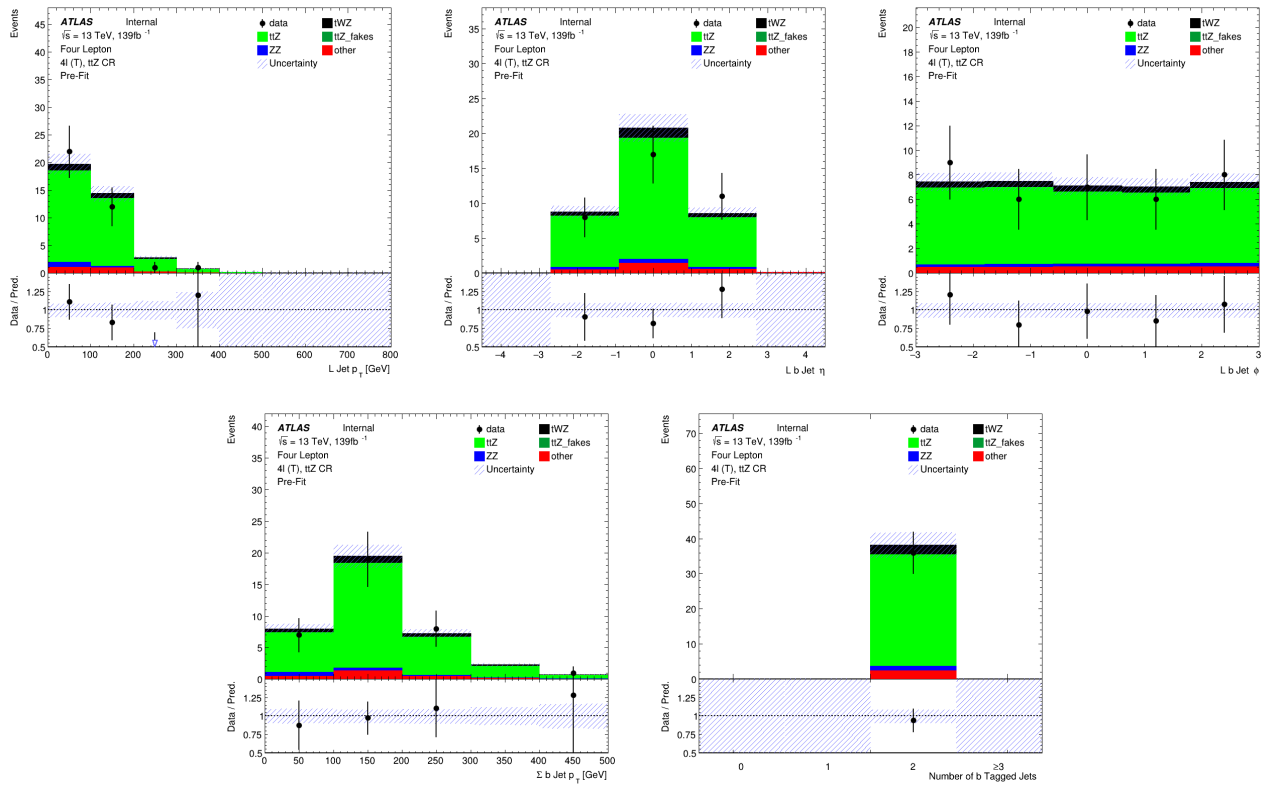


Figure 4.16: **Top row:** MC predictions for p_T , η and ϕ for leading b-tagged jets in the $t\bar{t}Z$ CR region (*blinded*) is shown. **Bottom row:** MC predictions for the scalar sum of b-tagged jet p_T (left) and the Number of b-tagged jets (right) in the $t\bar{t}Z$ CR region (*blinded*) is shown.

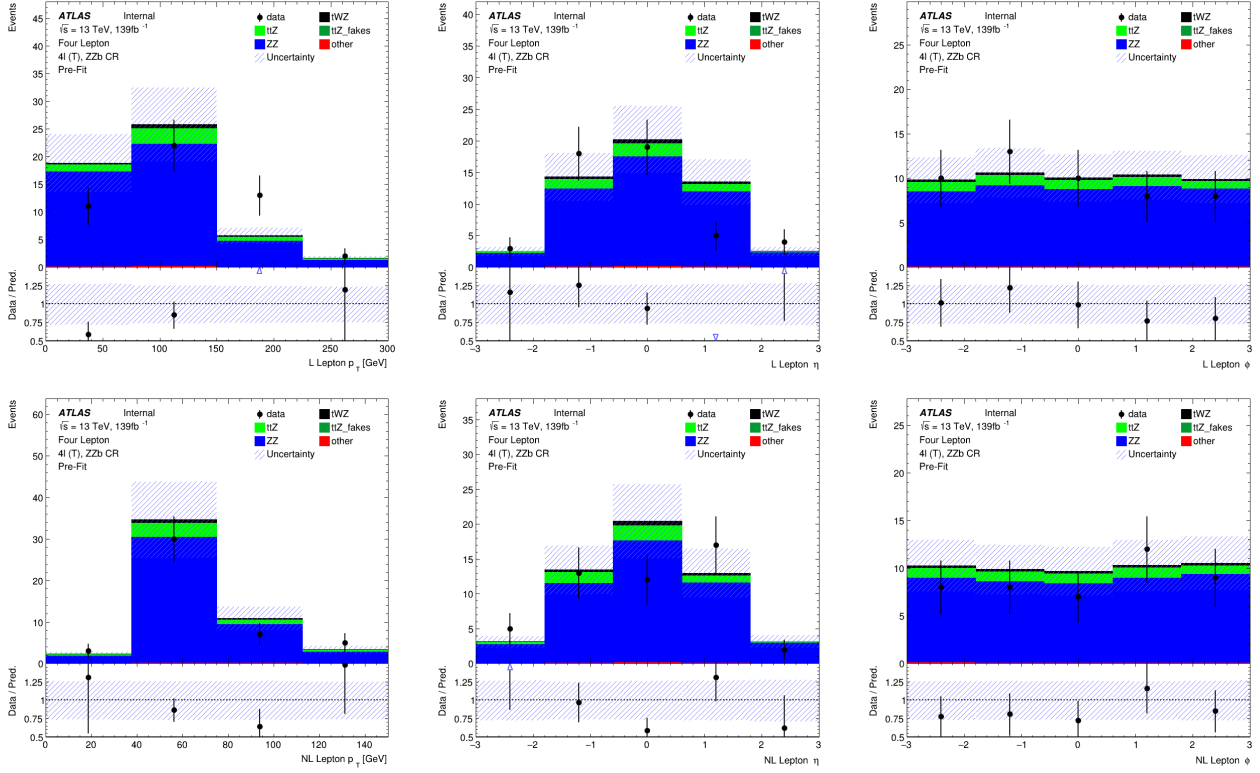


Figure 4.17: MC predictions for p_T , η and ϕ for leading (L) leptons (top row) and next-to-leading (NL) leptons (bottom row) in the ZZb CR region (*blinded*) is shown.

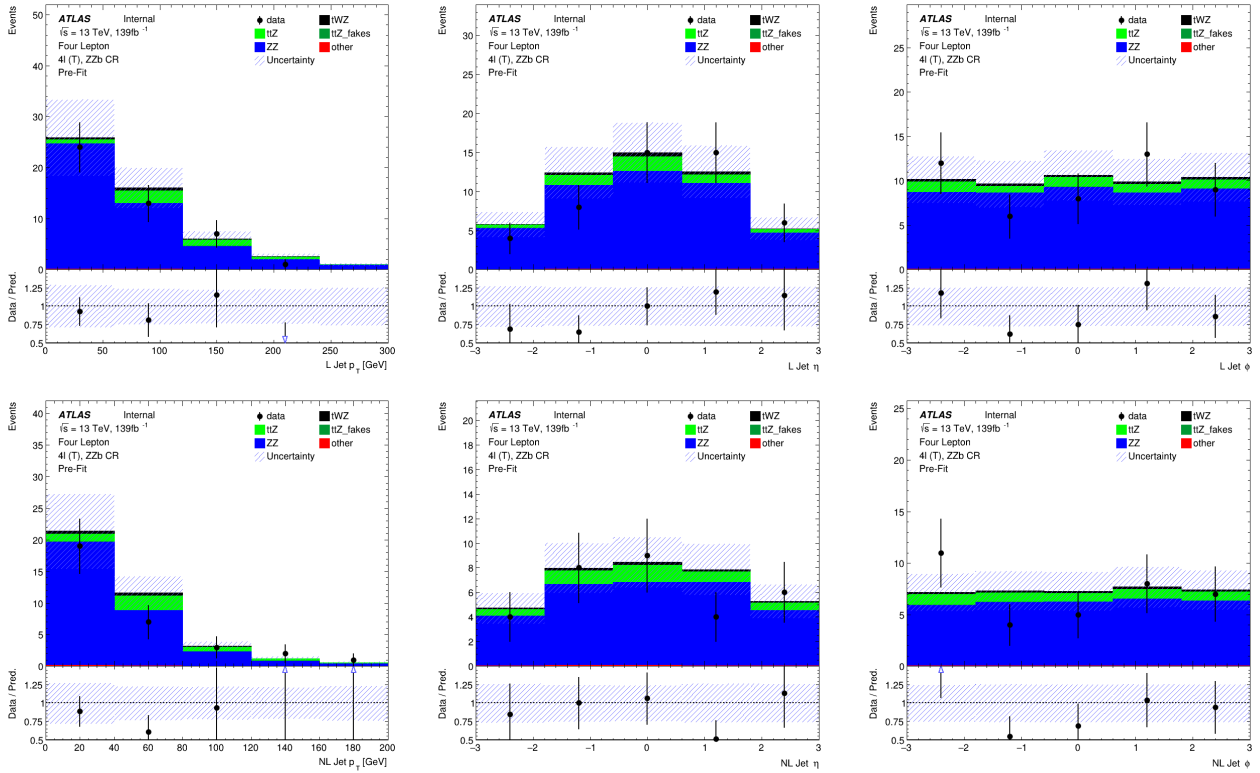


Figure 4.18: MC predictions for p_T , η and ϕ for leading (L) jets (top row) and next-to-leading (NL) jets (bottom row) in the ZZb CR region (*blinded*) is shown.

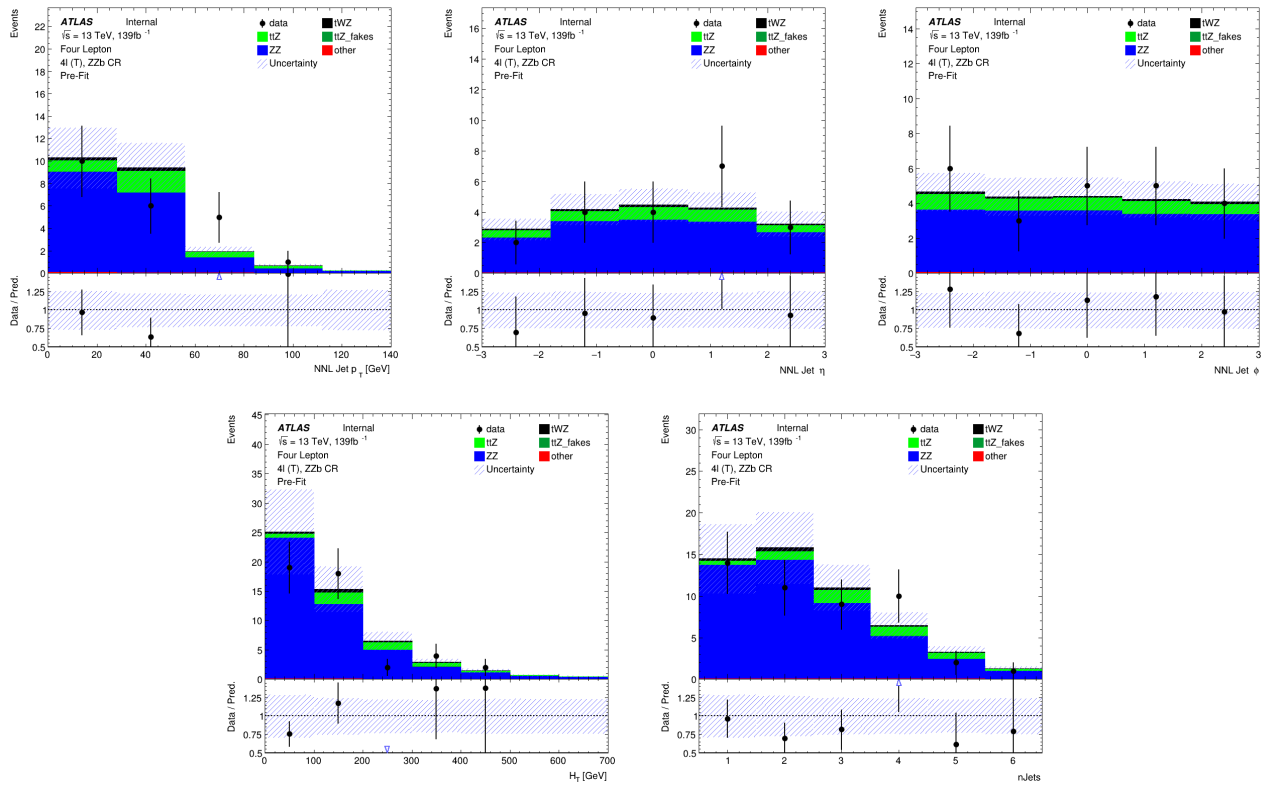


Figure 4.19: **Top row:** MC predictions for p_T , η and ϕ for next-to-next-to-leading (NNL) jets in the ZZb CR region (*blinded*) is shown. **Bottom row:** MC predictions for H_T (scalar sum of Jet p_T) (left) and the Number of jets (right) in the ZZb CR region (*blinded*) is shown.

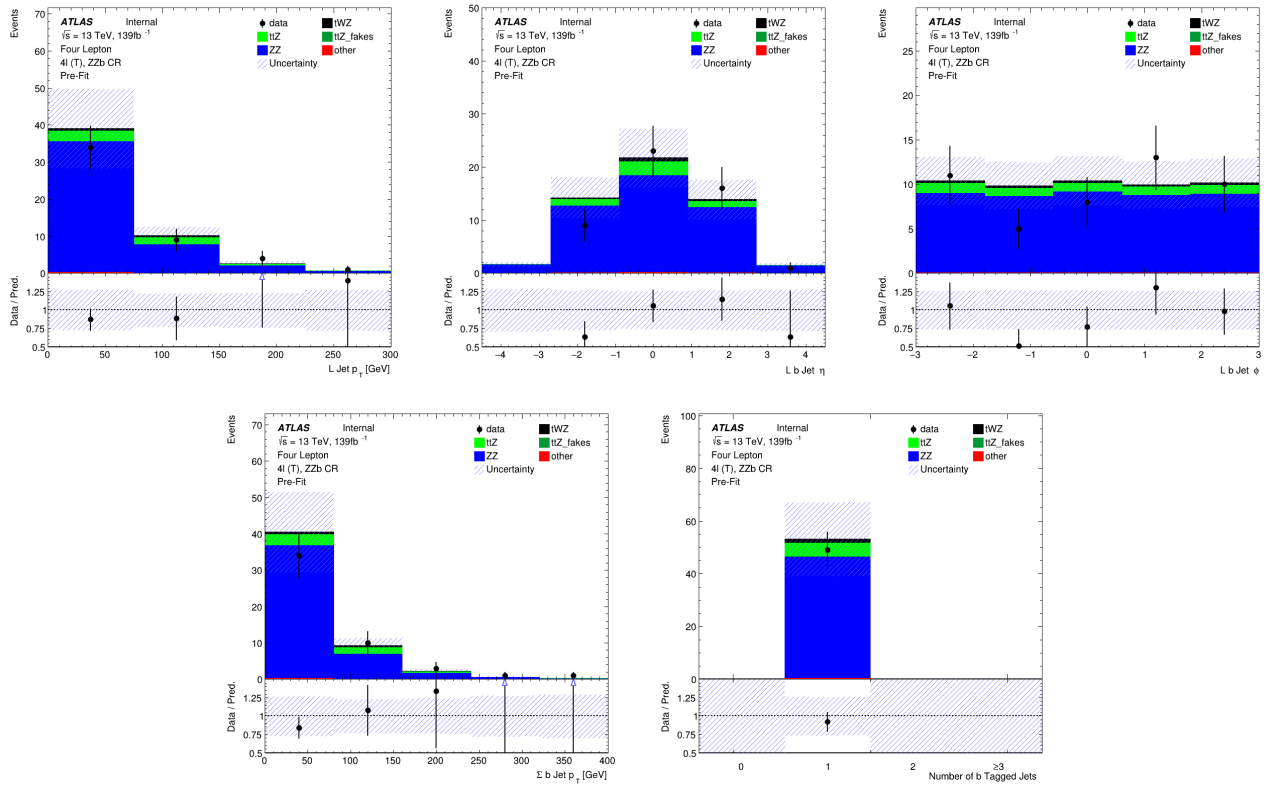


Figure 4.20: **Top row:** MC predictions for p_T , η and ϕ for leading b-tagged jets in the ZZb CR region (*blinded*) is shown. **Bottom row:** MC predictions for the scalar sum of b-tagged jet p_T (left) and the Number of b-tagged jets (right) in the ZZb CR region (*blinded*) is shown.

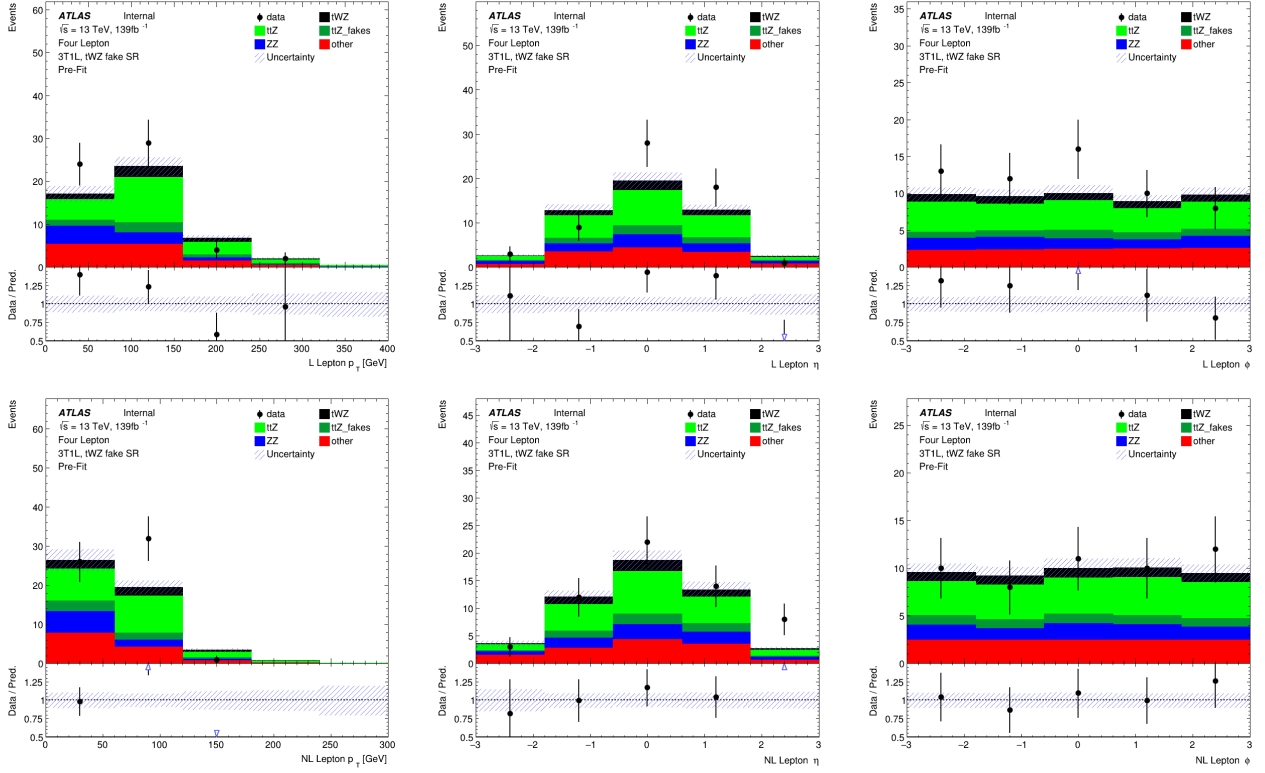


Figure 4.21: MC predictions for p_T , η and ϕ for leading (L) leptons (top row) and next-to-leading (NL) leptons (bottom row) in the (tWZ) fake CR region (*blinded*) is shown.

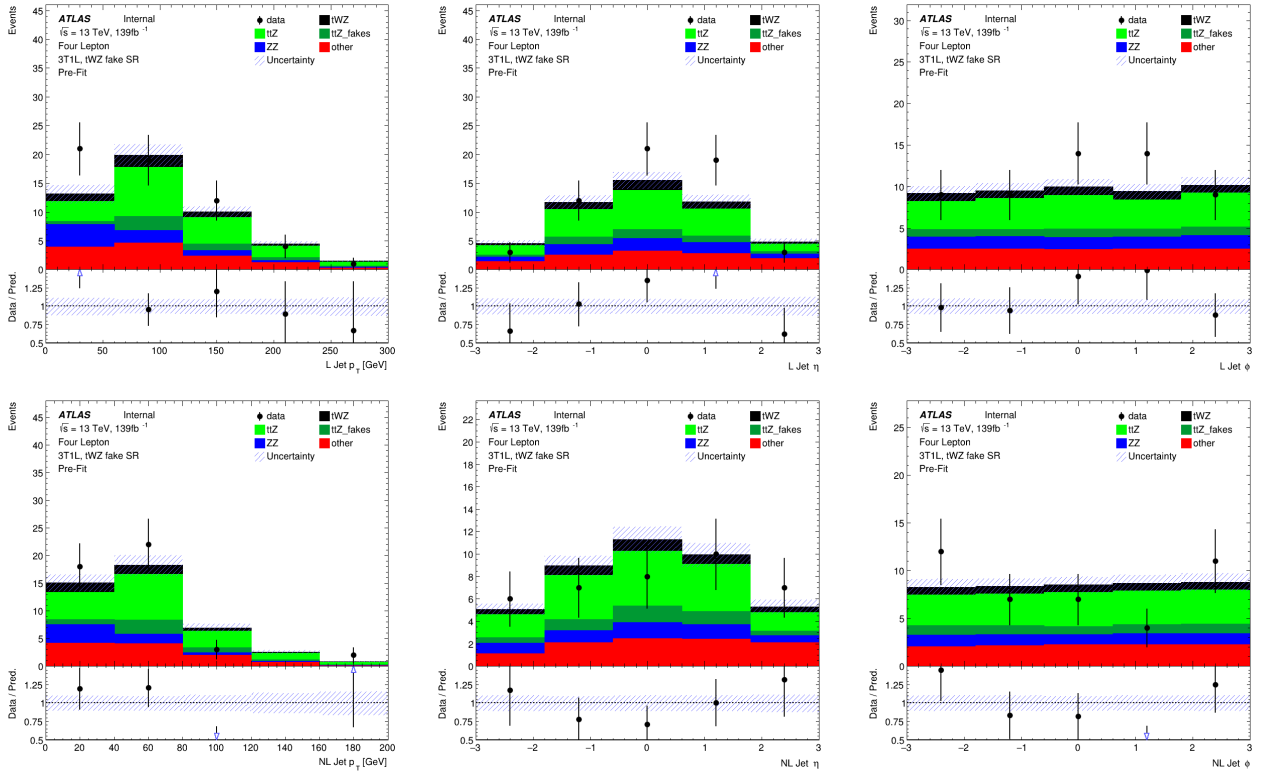


Figure 4.22: MC predictions for p_T , η and ϕ for leading (L) jets (top row) and next-to-leading (NL) jets (bottom row) in the (tWZ) fake CR region (*blinded*) is shown.

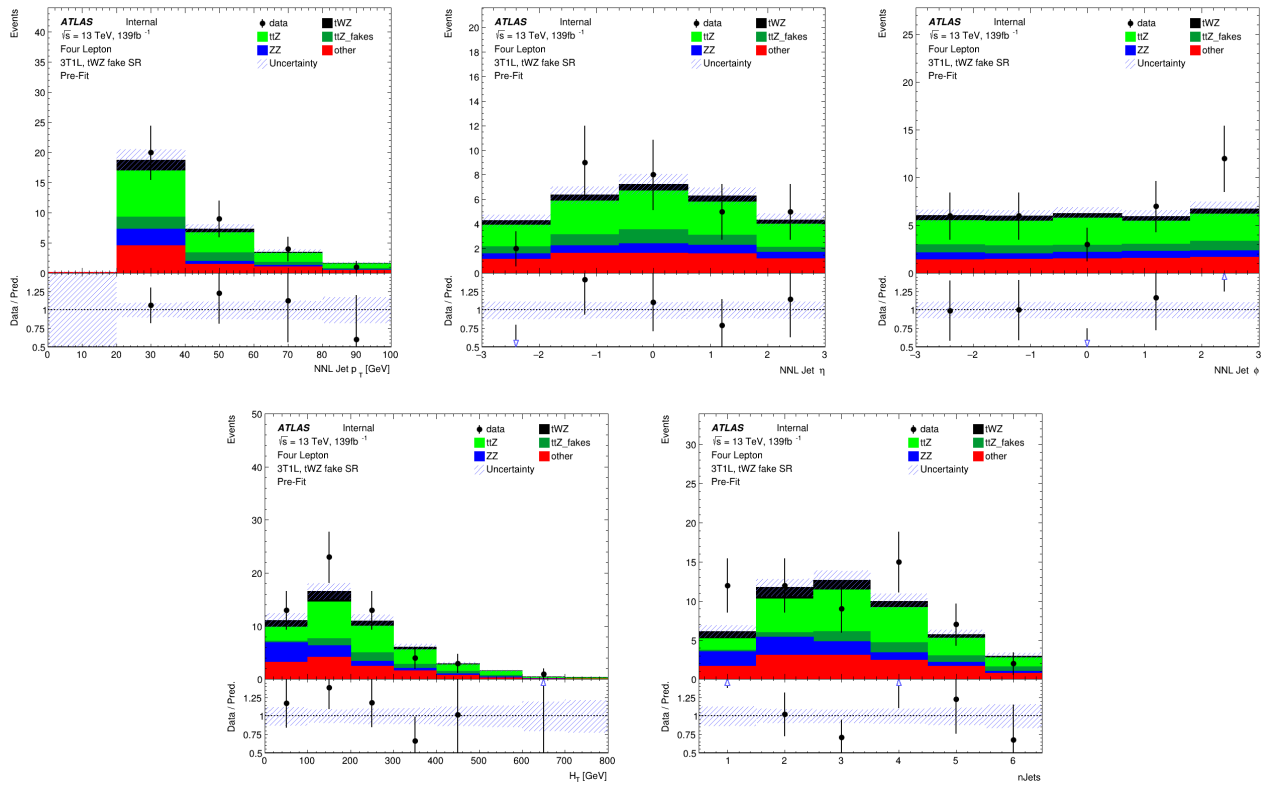


Figure 4.23: **Top row:** MC predictions for p_T , η and ϕ for next-to-next-to-leading (NNL) jets in the $(tWZ)_{\text{fake}}$ CR region (*blinded*) is shown. **Bottom row:** MC predictions for H_T (scalar sum of Jet p_T) (left) and the Number of jets (right) in the $(tWZ)_{\text{fake}}$ CR region (*blinded*) is shown.

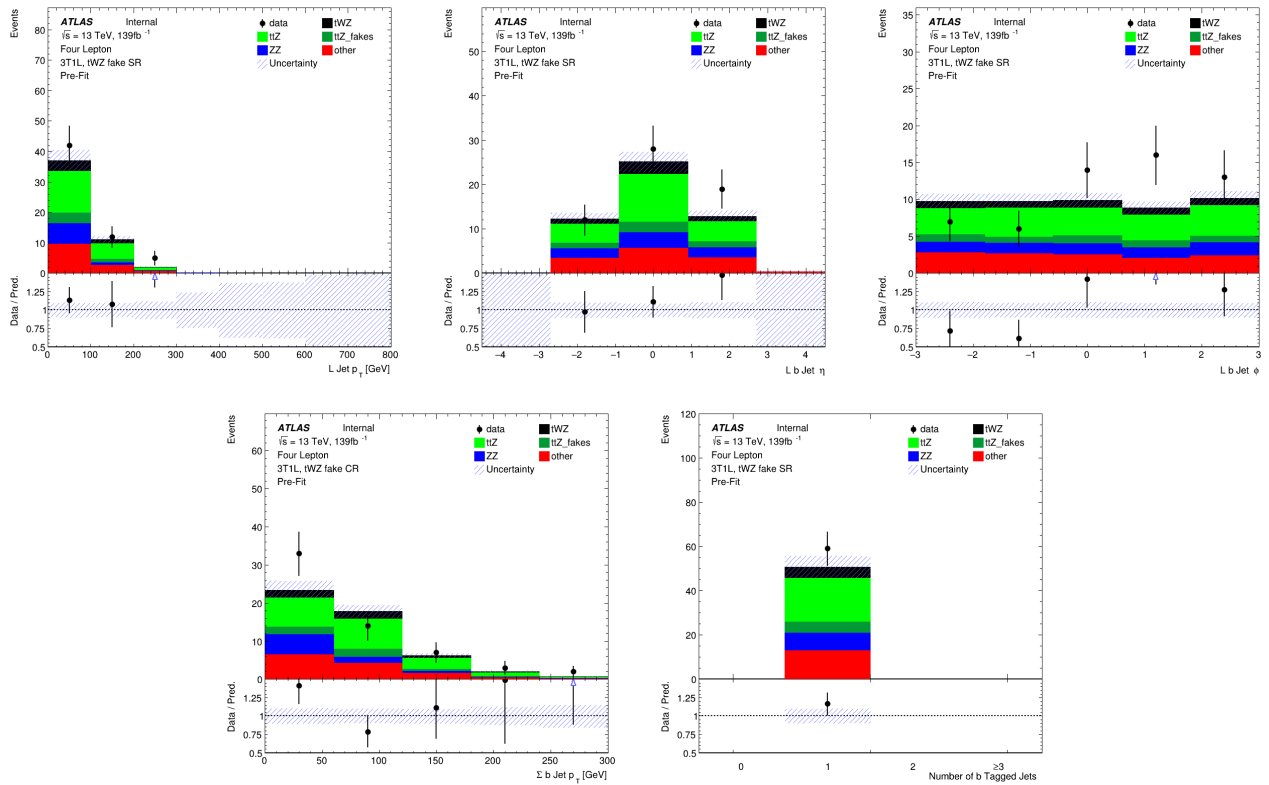


Figure 4.24: **Top row:** MC predictions for p_T , η and ϕ for leading b-tagged jets in the $(tWZ)_{\text{fake}}$ CR region (*blinded*) is shown. **Bottom row:** MC predictions for the scalar sum of b-tagged jet p_T (left) and the Number of b-tagged jets (right) in the $(tWZ)_{\text{fake}}$ CR region (*blinded*) is shown.

We aim to estimate the fake lepton contribution in this analysis. We start off by noticing that $t\bar{t}Z$ is our most dominant background ($\sim 75\%$ of the total background contribution) and will therefore have the largest fake component compared to all other samples considered in the analysis. The fake lepton efficiency, ϵ , can be written as $\epsilon = \frac{N_{\text{fake}}^{\text{tight}}}{N_{\text{fake}}^{\text{loose}}}$, where $N_{\text{fake}}^{\text{tight}}$ is the number of fake leptons which pass the tight lepton selection (See Section 4.2.1) and $N_{\text{fake}}^{\text{loose}}$ is the number of fake leptons which pass the loose lepton selection (See Section 4.2.1). The probability of one fake lepton to occur, $P(\text{one fake } \ell)$, is proportional to ϵ and the probability for two fakes to occur is simply, $P(\text{two fake } \ell) = (P(\text{one fake } \ell))^2 \propto \epsilon^2$. Since $\epsilon < 1$, we have $P(\text{one fake } \ell) \ll P(\text{two fake } \ell)$. For the purposes of this analysis we shall investigate the fake lepton component to first order and therefore will only consider the case where one fake lepton occurs in a $t\bar{t}Z$ event.

Firstly, we split up the dominant $t\bar{t}Z$ background into $t\bar{t}Z$ and $(t\bar{t}Z)_{\text{fake}}$ components. Secondly, we define a $(tWZ)_{\text{fake}}$ CR (See Section 4.4) which is enhanced in fakes and aims to constrain the $(t\bar{t}Z)_{\text{fake}}$ background in the SR.

All events which contribute to the $(t\bar{t}Z)_{\text{fake}}$ background are determined by the IFF Truth Classifier [27]. The IFF Truth Classifier is a tool which aims to classify leptons based off their truth information. It uses the more general MCTruthClassifier [MCTruthClassifier] tool's output as input and returns one of the following lepton categories: Unknown, KnownUnknown (leptons which can (in principle) be classified, but the MCTruthClassifier fails to classify the lepton's truth type or origin), IsoElectron, ChargeFlipIsoElectron, PromptMuon, PromptPhotonConversion, ElectronFromMuon, TauDecay, BHadronDecay, CHadronDecay or LightFlavorDecay (More details [28]). Given these categories, we consider leptons classified as BHadronDecay, CHadronDecay or LightFlavorDecay (i.e. a lepton originating from the decay of a b -Hadron, c -Hadron or light-flavour jet) to be fakes. Since we only consider events with one fake lepton to contribute to our $(t\bar{t}Z)_{\text{fake}}$ background, we require that events which contribute to this background are those where exactly one lepton from the $t\bar{t}Z$ sample are classified by the IFF Truth Classifier with one of the three aforementioned categories.

The $(tWZ)_{\text{fake}}$ CR aims to be as similar as possible to the tWZ SRs, but enhanced in fakes. This CR can then be used to constrain the normalisation of the $(t\bar{t}Z)_{\text{fake}}$ template from data, since we use the *mixed data and MC fit* (See Section 4.10) which uses the data in the CRs to construct a modified ASIMOV dataset from the fitted nuisance parameters from a background only fit to the CRs. To ensure that this region is enhanced in fakes, we require that it contains 3 tight leptons and 1 loose lepton, since loose leptons are more likely to be fakes. By using the p_T of the loose lepton ($p_T(\text{Loose Lepton})$) in this region as the variable used in the fit, the shape (and normalisation) of the $(t\bar{t}Z)_{\text{fake}}$ template can be constrained.

The proportion of fake events in a region can be calculated by taking the ratio of the $(t\bar{t}Z)_{\text{fake}}$ MC yield in the region and the total MC yield in the region. These are 0.0035 ± 0.0025 , 0.0014 ± 0.0012 and 0.10 ± 0.051 for the tWZ OF SR, tWZ SF SR and $(tWZ)_{\text{fake}}$ CR respectively. This shows that there is significantly more $(t\bar{t}Z)_{\text{fake}}$ events in the $(tWZ)_{\text{fake}}$ CR compared to the tWZ SRs, therefore justifying our inclusion of the $(tWZ)_{\text{fake}}$ CR in the fit (to constrain the $(t\bar{t}Z)_{\text{fake}}$ background).

4.7 Machine Learning Techniques

Now that we have our baseline selections applied and our regions defined, we implement two Boosted Decision Trees (BDT) in order to discriminate between tWZ and our most prominent background process, $t\bar{t}Z$ and ZZ . We chose to use a BDT, as opposed to another ML algorithm, since they are very stable and perform well with minimal/no optimisation or tweaking of the hyper parameters. A multi-layered sequential neural network was tried, however, it was out-performed by a BDT. More specifically, Scikit-Learn's GradientBoostingClassifier was used.

Two different BDTs were used, the first aims to discriminate between tWZ events and its major backgrounds, $t\bar{t}Z$ and ZZ . The second aims to discriminate between ℓb systems which originate from the decay of a top quark ($t \rightarrow W(\rightarrow \ell\nu)b$) and those which do not. We refer to these two BDTs as an **event-level** and an **object-level** classifier respectively. The discriminator output from the object-level BDT can be converted to a variable which can then be used as input to the event-level BDT.

4.7.1 Object-level BDT

The object-level BDT was trained on a $t\bar{t}$ sample, using the same jet and lepton baseline selections as outlined in Table 4.3. Minor differences occur between this $t\bar{t}$ sample and the MC samples used for the rest of the analysis, such as the use of the older MV2c10 b -tagger. This is such since the $t\bar{t}$ sample was used in a separate analysis and was re-purposed for this analysis. Despite these differences, the trained object-level BDT is sufficient in this case, since we expect that ℓb systems present in the $t\bar{t}$ sample are similar enough to those present in the MC samples used in the rest of the analysis. Additionally, we opted to use this disjoint $t\bar{t}$ sample as to avoid resorting to use our MC samples used in the rest of the analysis which is heavily limited on statistics, therefore maximizing the amount of MC statistics used in the fitting procedure and the training of the event-level BDT.

The signal class is defined to consist of reconstructed ℓb systems (defined as the sum of the 4-vectors of the lepton and b -jet) coming from top quarks which are well matched to their truth counterparts. In particular, we require that ΔR between the reconstructed and truth ℓb system is less than 0.05. We additionally require that the reconstructed lepton and the truth top have charges with the same sign (since $t \rightarrow b\ell^+\bar{\nu}_\ell$ and $\bar{t} \rightarrow \bar{b}\ell^-\nu_\ell$). Conversely, the background class is defined to consist of reconstructed ℓb systems which are not well matched to their truth counterparts. In particular, we require that ΔR between the reconstructed and truth ℓb system is greater than 0.05. We additionally require that the reconstructed lepton and the truth top have charges with opposite sign. These definitions for the signal and background classes ensure that the signal class consists of mostly ℓb systems originating from tops and the background class consists of mostly ℓb systems which do not originate from a top decay.

Different observables corresponding to an ℓb system were used as input to training. The optimum values for the hyper-parameters used were determined by training the BDT with a range of different values for the hyper-parameters and choosing the set of values which maximized the mean accuracy (based off 5 fold kfold cross-validation). This method is more commonly referred to as hyper-parameter optimisation or tuning. After hyper-parameter optimisation, the mean accuracy of each fold increased from 0.76 to 0.77 ($\sim 1\%$ increase).

In Table 4.5, the variables used in training the object-level BDT are shown.

Observable	Description
$m(\ell b)$	Invariant mass of the ℓb system
$p_T(\ell b)$	p_T of the ℓb system
$\Delta\eta(\ell, b)$	$\Delta\eta$ between the ℓ and b -tagged jet
$\Delta\phi(\ell, b)$	$\Delta\phi$ between the ℓ and b -tagged jet
$\Delta R(\ell, b)$	ΔR between the ℓ and b -tagged jet

Table 4.5: A list of the observables used in the object-level BDT, ordered by importance (descending, top to bottom) is shown.

In Figure 4.26, normalised distributions of the signal and background classes for the training set of all variables used in the object-level BDT are show.

Overall the BDT input variables show a large amount of discrimination.

In Table 4.6, the hyper-parameters used in the object-level BDT is shown.

The number of events used in training for the signal and background classes were 347952 and 266636 respectively. Imbalanced datasets can cause ML classifiers to ignore small classes while concentrating on classifying large classes more accurately, which may result in the trained classifier performing sub-optimally. In order to correct this dataset imbalance, we ensure that the relative weighting of each event is such that the sum of the signal weights is equal to the sum of the background weights. In Figure 4.27 the normalised histograms of the training and test sets (extracted from fold 5 from a 5 fold kfold cross validation) for signal and background is shown.

We can see that the shapes of the training and test sets for both signal and background are very similar. This is a good indicator that no over-training occurred. Another over-training check is performed using 5 fold kfold cross validation. We ensure that the variance of the mean accuracy of each folds' test set in cross validation is substantially small. This indicates that fluctuations in features from different training sets are not learnt by the

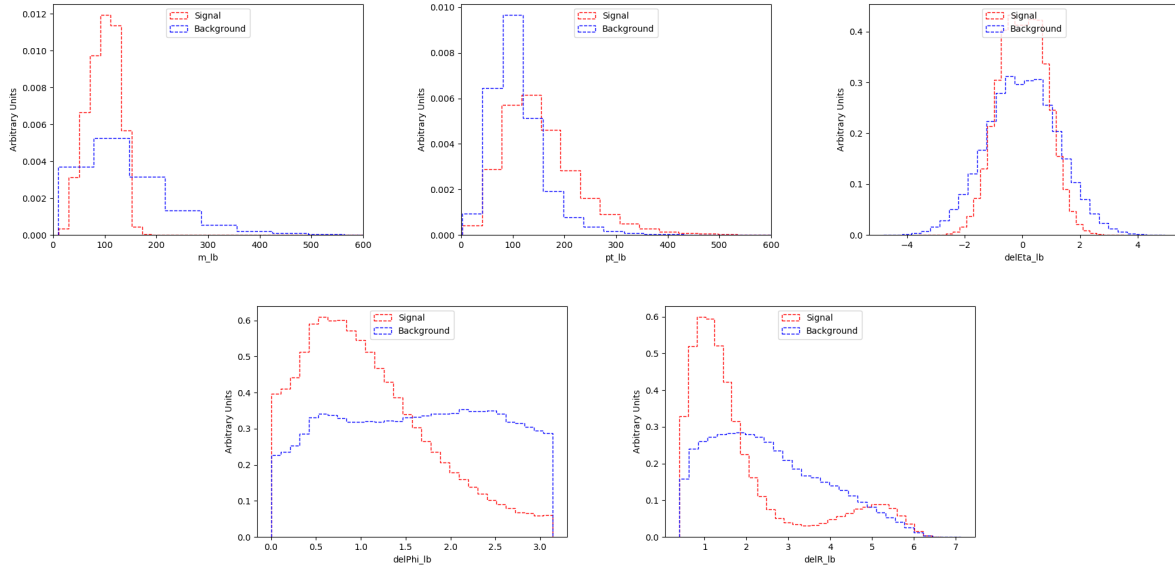


Figure 4.25: Normalised distributions of the signal and background classes for the training set of all variables used in the object-level BDT (ordered from top left to bottom right via decreasing importance) are shown. The red and blue dotted lined histograms represent the signal and background classes events (normalised to an area of 1), respectively. The variable used in training is shown on the x-axis. The y-axis shows the relative number of events for the signal and background classes (in arbitrary units). **From top left to bottom right:** Invariant mass of the llb system. The p_T of the llb system. $\Delta\eta$ between the ℓ and b -tagged jet. $\Delta\phi$ between the ℓ and b -tagged jet. ΔR between the ℓ and b -tagged jet.

Hyper-parameter	Value	Description
loss	deviance	The loss function to be optimised
criterion	friedman_mse	The function used to measure the quality of a split
n_estimators	200	The number of boosting stages to perform
learning_rate	0.1	The step size at each iteration during optimisation
max_depth	6	The maximum depth of the individual regression estimators
min_samples_split	2	The minimum number of samples (events) required to split an internal node
min_samples_leaf	1	The minimum number of samples (events) required to be at a leaf node
validation_fraction	0.1	The proportion of training data to set aside as validation set for early stopping
n_iter_no_change	20	Training terminates when the validation score (determined by the validation set) does not improve in all of the previous

Table 4.6: A list of the hyper-parameters used in the object-level BDT is shown. Hyperparameters not listed in this table use the default values as stated in the Scikit-learn Documentation[38].

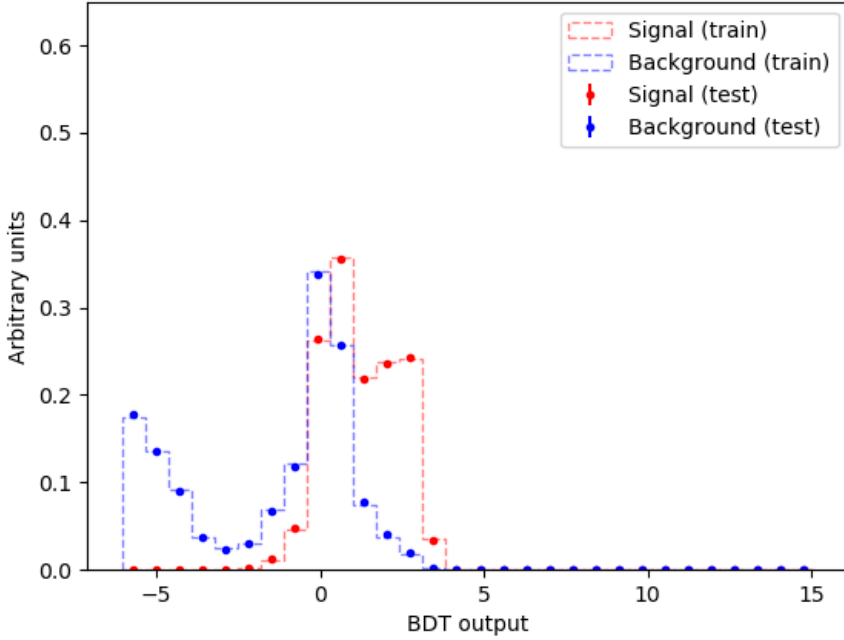


Figure 4.26: Normalised histograms of the object-level BDT discriminator output from the signal and background classes for the training and test sets from the 5th fold in a 5 fold kfold cross validation is shown. The output of the object-level BDT is shown on the x-axis and the relative number of events (in arbitrary units) is shown on the y-axis. The training set for the signal class is shown by the red dotted histogram. The test set for the signal class is shown by the red points, with the total uncertainty represented by the vertical error bars. The training set for the background class is shown by the blue dotted histogram. The test set for the background class is shown by the blue points, with the total uncertainty represented by the vertical error bars.

classifier. For the object-level classifier, a variance of 3.24×10^{-7} was calculated for the mean accuracies of each folds' test set in cross validation, providing further evidence that no over-training occurred.

The output from the object-level BDT was used to construct a variable to be used as input to the event-level BDT. The event-level BDT aims to discriminate between tWZ and our most prominent background, $t\bar{t}Z$. We therefore aim to construct a variable from the output of the object-level BDT which discriminates well between tWZ and $t\bar{t}Z$. Since tWZ events contain one top quark and $t\bar{t}Z$ events contain two top quarks, we expect that tWZ events have one ℓb combination which scores well and we expect that $t\bar{t}Z$ events have two ℓb combinations which score well. We construct a variable, $\text{BDTScore}(\frac{\text{Best}}{\text{2nd Best}})$, which takes the ratio of the scores of the top scoring ℓb system to the 2nd best scoring ℓb system. We expect this variable to be large for tWZ events and closer to one for $t\bar{t}Z$ events, therefore providing discrimination between tWZ and $t\bar{t}Z$.

In Figure 4.28, normalised distributions of the signal and total background of the $\text{BDTScore}(\frac{\text{Best}}{\text{2nd Best}})$ variable in the tWZ OF SR, tWZ SF SR and $t\bar{t}Z$ CR are shown.

There doesn't seem to be a large amount of discrimination between signal and background for $\text{BDTScore}(\frac{\text{Best}}{\text{2nd Best}})$ in either of the above regions. We do however see some discrimination in bins near a value of 1, where the number of background events exceed the number of signal events, which is what we expect. This effect is slightly more exaggerated in the $t\bar{t}Z$ CR than the tWZ SRs. This can be explained since we expect to have a larger proportion of $t\bar{t}Z$ events (events with two ℓb systems) in the $t\bar{t}Z$ CR. Despite the apparent lack of discrimination between signal and background events from this variable, when used as input to training in the event-level BDT (see Section 4.7.2), it ranks relatively high on variable importance (see Table 4.7) and thus improves the mean accuracy of the classifier. The tells us that the event-level BDT is taking advantage of the discrimination between signal and background

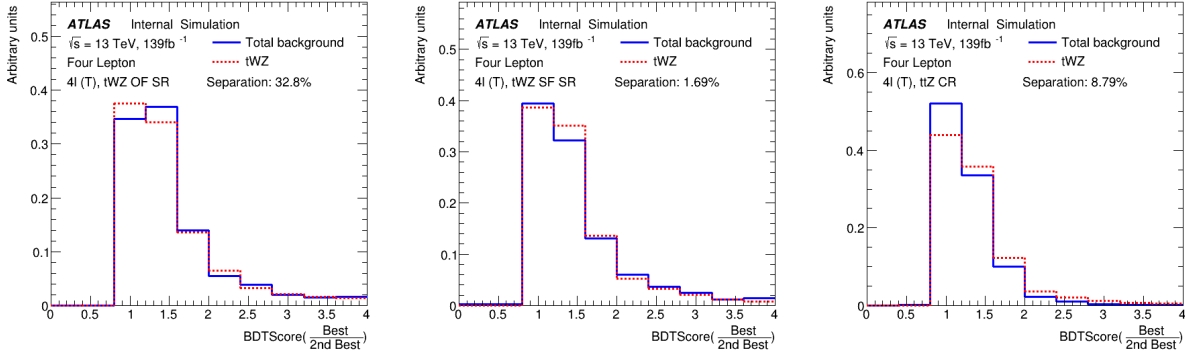


Figure 4.27: Normalised distributions of the signal and total background of the $\text{BDTScore}(\frac{\text{Best}}{\text{2nd Best}})$ variable in the tWZ OF SR, tWZ SF SR and $t\bar{t}Z$ CR are shown (left to right). The dotted red and solid blue lines represent the distributions (normalised to an area of 1) of the signal and total background events respectively. The x-axis shows the $\text{BDTScore}(\frac{\text{Best}}{\text{2nd Best}})$ and the y-axis show the relative number of events (in arbitrary units).

present in the $\text{BDTScore}(\frac{\text{Best}}{\text{2nd Best}})$ variable.

4.7.2 Event-level BDT

The event-level BDT was trained on 50% of the tWZ MC sample’s events for the signal class and similarly, 50% of the $t\bar{t}Z$ and ZZ MC sample’s events were used for the background class. The samples we train on are individual events, with the features being carefully chosen observables. These observables are chosen on the basis that they are somewhat uncorrelated from one another and show a relatively large amount of separation power between tWZ and $t\bar{t}Z$. Similarly to the object-level BDT, the optimum values for the hyper-parameters used were determined via hyper-parameter optimisation. After hyperparameter optimisation, the mean accuracy of each fold (determined from 5 fold kfold cross validation) increased from 0.72 to 0.74 ($\sim 3\%$ increase).

In Table 4.7, the variables used in training the event-level BDT are shown.

Observable	Description
$2\nu\text{SM}$	Maximum weight from the $2\nu\text{SM}$ algorithm
HT	Scalar sum of jet p_T
LT	Scalar sum of lepton p_T
$\sum p_T(b-jet)$	Scalar sum of b -tagged jet p_T
$\text{BDTScore}(\frac{\text{Best}}{\text{2nd Best}})$	Ratio of the top scoring ℓb system to the 2nd best scoring ℓb system from the output of the object-level BDT (ℓb classifier)
$\Delta\eta(\ell_{1,\text{Non}-Z}, \ell_{2,\text{Non}-Z})$	$\Delta\eta$ between the two leptons, not coming from a Z candidate
$\min(m(\ell b))$	Mass of the ℓb system with the smallest mass
$\Delta\phi(\ell_{1,\text{Non}-Z} \ell_{2,\text{Non}-Z}, b_1)$	$\Delta\phi$ between the non- Z lepton system (leptons not originating from a Z -candidate) and the leading b -tagged jet

Table 4.7: A list of the observables used in the event-level BDT, ordered by importance (descending, top to bottom) is shown.

In Figure 4.29, normalised distributions of the signal and background classes for the training set of all variables used in the event-level BDT are shown.

Overall the BDT input variables show a reasonable amount of discrimination. In particular the output weight from the $2\nu\text{SM}$ algorithm shows the most discrimination. When determining which variables to use in training the event-level BDT, the output weight from $2\nu\text{SM}$ was shown to provide the most sizeable boost in performance of the BDT. Surprisingly, the least important variable, $\Delta\phi$ between the non- Z lepton system (leptons not originating from a Z -candidate) and the leading b -tagged jet, seem to discriminate well between signal and background. A possible explanation for its low ranking importance is due to it being relatively highly correlated with many of the other input variables.

In Table 4.8, the hyper-parameters used in the event-level BDT are shown.

Since we are training on $t\bar{t}Z$ and ZZ events for the background class, we ensure that the relative weighting of these events are such that they mimic the amount of $t\bar{t}Z$ and ZZ expected to be present in the regions where we aim to use the BDT discriminator (tWZ SRs and $t\bar{t}Z$ CR). This is done by applying normalization weights to each event,

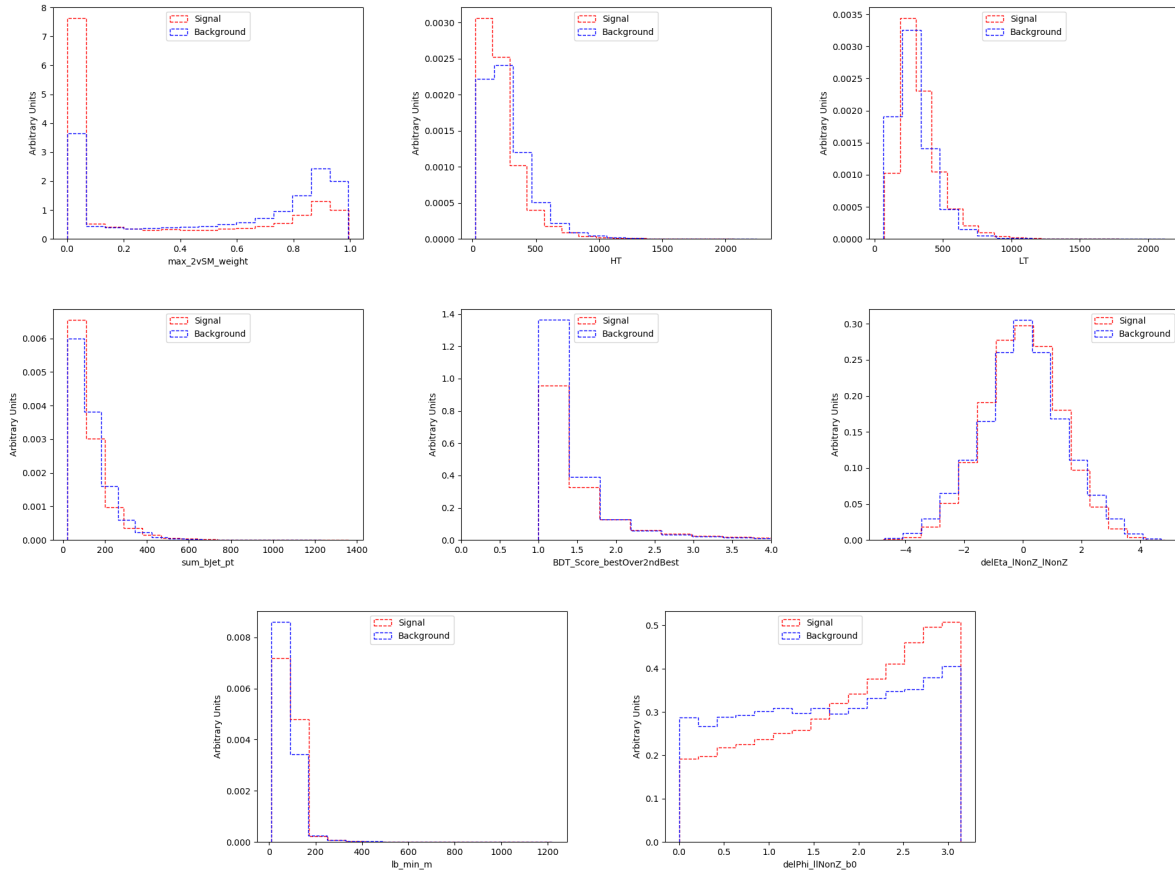


Figure 4.28: Normalised distributions of the signal and background classes for the training set of all variables used in the event-level BDT (ordered from top left to bottom right via decreasing importance) are shown. The red and blue dotted lined histograms represent the signal and background classes events (normalised to an area of 1), respectively. The variable used in training is shown on the x-axis. The y-axis shows the relative number of events for the signal and background classes (in arbitrary units). **From top left to bottom right:** Output weight from the 2ν SM algorithm (See Section 4.8). Scalar sum of jet p_T . Scalar sum of lepton p_T . Sum of b -tagged jet p_T . Output from the object-level BDT (See Section 4.7.1). $\Delta\eta$ between the two leptons, not coming from a Z candidate. Mass of the ℓb system with the smallest mass. $\Delta\phi$ between the non- Z lepton system (leptons not originating from a Z -candidate) and the leading b -tagged jet.

Hyper-parameter	Value	Description
loss	deviance	The loss function to be optimised
criterion	friedman_mse	The function used to measure the quality of a split
n_estimators	200	The number of boosting stages to perform
learning_rate	0.1	The step size at each iteration during optimisation
max_depth	6	The maximum depth of the individual regression estimators
min_samples_split	2	The minimum number of samples (events) required to split an internal node
min_samples_leaf	1	The minimum number of samples (events) required to be at a leaf node
validation_fraction	0.1	The proportion of training data to set aside as validation set for early stopping
n_iter_no_change	20	Training terminates when the validation score (determined by the validation set) does not improve in all of the previous

Table 4.8: A list of the hyper-parameters used in the event-level BDT is shown. Hyperparameters not listed in this table use the default values as stated in the Scikit-learn Documentation[38].

defined as,

$$W = \frac{\sigma \mathcal{L} \text{weight(MC)}}{\text{totalWeight(MC)}} \quad (4.1)$$

where σ is the cross section of the process, \mathcal{L} is the integrated luminosity, weight(MC) is the weight assigned to the event by the MC generator and totalWeight(MC) is the sum of those weights for all the generated events.

The number of events used in training for the signal and background classes were 41157 and 22701 respectively. Similarly to the object-level BDT, there is a dataset imbalance. We correct this imbalance (in the same way as before with the object-level BDT) by ensuring that the relative weighting of each event is such that the sum of the signal weights is equal to the sum of the background weights.

In Figure 4.30 the normalised histograms of the training and test sets (extracted from fold 5 from a 5 fold kfold cross validation) for signal and background is shown.

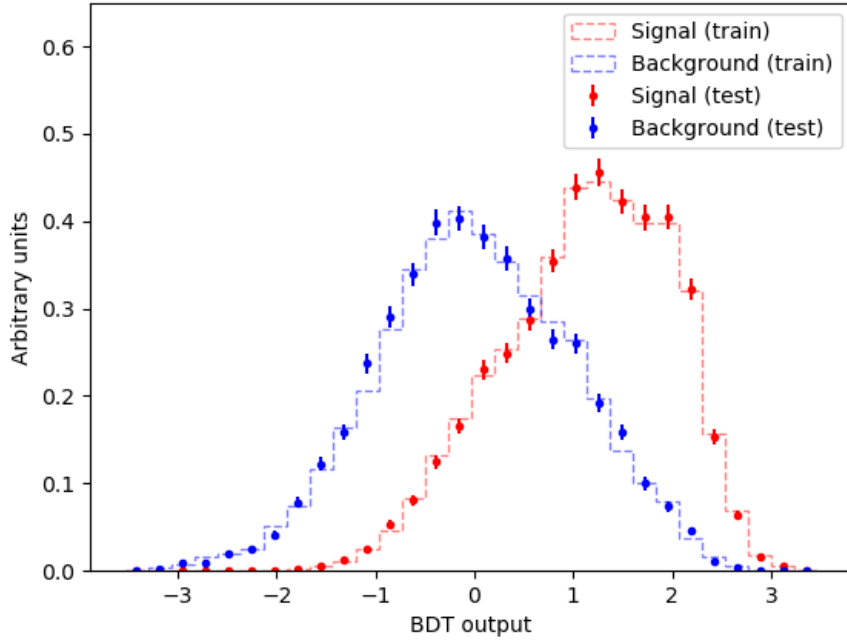


Figure 4.29: Normalised histograms of the event-level BDT discriminator output from the signal and background classes for the training and test sets from the 5th fold in a 5 fold kfold cross validation are shown. The output of the event-level BDT is shown on the x-axis and the relative number of events (normalised to have an area of 1, in arbitrary units) is shown on the y-axis. The training set for the signal class is shown by the red dotted histogram. The test set for the signal class is shown by the red points, with the total uncertainty represented by the vertical error bars. The training set for the background class is shown by the blue dotted histogram. The test set for the background class is shown by the blue points, with the total uncertainty represented by the vertical error bars.

We can see that the shapes of the training and test sets for both signal and background are very similar. This is a good indicator that no over-training occurred. As with the object-level BDT, we perform another over-training check, by ensuring that the variance of the mean accuracy of each folds' test set in a 5 fold kfold cross validation is substantially small. This indicates that fluctuations in features from different training sets are not learnt by the classifier. For the event-level classifier, a variance of 0.00026 was calculated for the mean accuracies of each folds' test set in cross validation, providing further evidence that no over-training occurred.

4.8 Two Neutrino Scanning Method ($2\nu\text{SM}$) Algorithm

The Two Neutrino Scanning Method ($2\nu\text{SM}$) algorithm² [31, 30] aims to reconstruct $t\bar{t}$ systems in the 2ℓ , 3ℓ and 4ℓ final states (e.g. 2ℓ case: $t\bar{t} \rightarrow \ell^+ \nu_\ell b \ell^- \bar{\nu}_\ell \bar{b}$). This was initially designed to suppress the $t\bar{t}$ background in the $t\bar{t}$ analysis. We can re-purpose this algorithm to distinguish between tWZ and $t\bar{t}Z$ by removing the easily-identifiable Z boson.

The $2\nu\text{SM}$ algorithm reconstructs a $t\bar{t}$ system by scanning through the components of two possible neutrino 4-vectors (ν_1 and ν_2). It then aims to determine which ν_1 and ν_2 correspond to the two neutrinos which originate from the decay of a $t\bar{t}$ system the best (quantified by an output weight, $w_{2\nu\text{SM}}$). $w_{2\nu\text{SM}}$ is the likelihood under the $t\bar{t}$ dilipeton final state hypothesis. We are able to use this algorithm in our analysis to discriminate between tWZ and $t\bar{t}Z$ since we can easily reconstruct the OSSF leptons which decay from the Z boson and remove it before inputting the event into the algorithm. We would then expect that the $2\nu\text{SM}$ algorithm returns a higher score from a $t\bar{t}Z$ event (~ 1 , i.e. it looks like a $t\bar{t}$ event after removal of the Z boson) and a lower score from a tWZ event (~ 0 , i.e. it does not look like a $t\bar{t}$ event after removal of the Z boson).

4.8.1 The algorithm

The $2\nu\text{SM}$ algorithm starts off by writing down four equations which correspond to the invariant masses of the top quark ($m(t)$) and W boson ($m(W)$) for the two top decays (i.e. $t \rightarrow W^+ b \rightarrow \ell^+ \nu_\ell$) in a dileptonic $t\bar{t}$ event. These can be written as,

$$(\ell_1 + \nu_1)^2 = m(W)^2 = (80.385 \text{ GeV})^2 \quad (4.2)$$

$$(\ell_1 + \nu_1 + b_{1,2})^2 = m(t)^2 = (172.5 \text{ GeV})^2 \quad (4.3)$$

$$(\ell_2 + \nu_2)^2 = m(W)^2 = (80.385 \text{ GeV})^2 \quad (4.4)$$

$$(\ell_2 + \nu_2 + b_{2,1})^2 = m(t)^2 = (172.5 \text{ GeV})^2 \quad (4.5)$$

where the subscripts indicate that these particles originate from the decay of two different top quarks in a $t\bar{t}$ system. We assume that the mass of the neutrinos (ν_1 and ν_2) are close to zero, which leaves us with 6 unknowns, p_{T,ν_1} , ϕ_{ν_1} , η_{ν_1} , p_{T,ν_2} , ϕ_{ν_2} and η_{ν_2} (components of the two neutrino's 4-vectors).

The $2\nu\text{SM}$ algorithm takes the 4-vectors of the two reconstructed leptons (not from the Z boson) and the two jets with the highest DL1r b -tagger score as input. For each neutrino (ν_1 and ν_2), we scan over a range of possible η and ϕ values. These values were chosen to be $\phi_{\nu_1}, \phi_{\nu_2} \in [-\pi, \pi]$ with a step size of ≈ 0.25 and $\eta_{\nu_1}, \eta_{\nu_2} \in [-5, 5]$ with a step size of ≈ 0.31 . These ranges were chosen to maximize accuracy and minimize computation time. For each of these possible η and ϕ values, we calculate the corresponding p_T for each neutrino. The transverse momentum of a neutrino, $p_{T,\nu}$, can be calculated via (*****referecne somewhere here*****),

$$p_{T,\nu} = \frac{\frac{1}{2}(m(W)^2 - m(\ell)^2)}{E_\ell \cosh \eta_\nu - p_{\ell,z} \sinh \eta_\nu - p_{\ell,x} \cos \phi_\nu - p_{\ell,y} \sin \phi_\nu} \quad (4.6)$$

where E_ℓ is the energy of the lepton and $p_{\ell,z}$, $p_{\ell,x}$, $p_{\ell,y}$ are the z , x and y components of lepton's momentum. At this stage, we have possible 4-vectors for ν_1 and ν_2 . Using these possible neutrino 4-vectors, we reconstruct the two possible $t\bar{t}$ systems,

$$t_1 = \ell_1 + b_1 + \nu_1 \text{ and } t_2 = \ell_2 + b_2 + \nu_2 \quad (4.7)$$

OR

$$t_1 = \ell_1 + b_2 + \nu_1 \text{ and } t_2 = \ell_2 + b_1 + \nu_2 \quad (4.8)$$

These reconstructed $t\bar{t}$ systems are then used to calculate a weight, $w_{2\nu\text{SM}}$. The $w_{2\nu\text{SM}}$ weight (a value ranging from 0 to 1) is defined as a product of four probabilities (described below) and can be written as,

$$w_{2\nu\text{SM}} = P_{m_{t_1}} \times P_{m_{t_2}} \times P_{\Delta E_x} \times P_{\Delta E_y} \quad (4.9)$$

The $w_{2\nu\text{SM}}$ is calculated for each pair of reconstructed neutrinos (or reconstructed $t\bar{t}$ systems), with the maximum value being chosen as the final value for the event.

²software tool and weights provided by Thomas McCarthy ($t\bar{t}Z$ analysis group - Max Planck Institute)

4.8.2 Calculating $w_{2\nu SM}$

We use distributions of well modelled observables ($m_{b\ell\nu}$ and ΔE_x) from simulated $t\bar{t}$ events in order to determine how well our reconstructed neutrinos (and in turn top quarks) resemble neutrinos (and top quarks) present in a $t\bar{t}$ event.

4.8.2.1 $P_{m_{t_1}}$ and $P_{m_{t_2}}$

A normalised distribution of the mass of reconstructed top quarks ($m_{b\ell\nu}$) from a $t\bar{t}$ sample is generated to determine the probabilities $P_{m_{t_1}}$ and $P_{m_{t_2}}$. The distribution is generated from reco-level leptons, generator-level neutrinos and reoc-level jets matched in ΔR to generator-level b -quarks, therefore only filling the distribution with correct detector-level objects. We then use the distribution to interpolate our two reconstructed top quarks, which returns a weight value from 0 to 1, with higher values corresponding to a reconstructed top quark which has a mass close to that of a top quark from a $t\bar{t}$ system. This interpolation is done for both reconstructed tops, t_1 and t_2 , corresponding to probabilities $P_{m_{t_1}}$ and $P_{m_{t_2}}$. The distribution used is shown in Figure 4.31.

In Figure 4.31, the $m_{b\ell\nu}$ distribution (generated from simulated $t\bar{t}$ events), used to calculate $P_{m_{t_1}}$ and $P_{m_{t_2}}$ is shown.

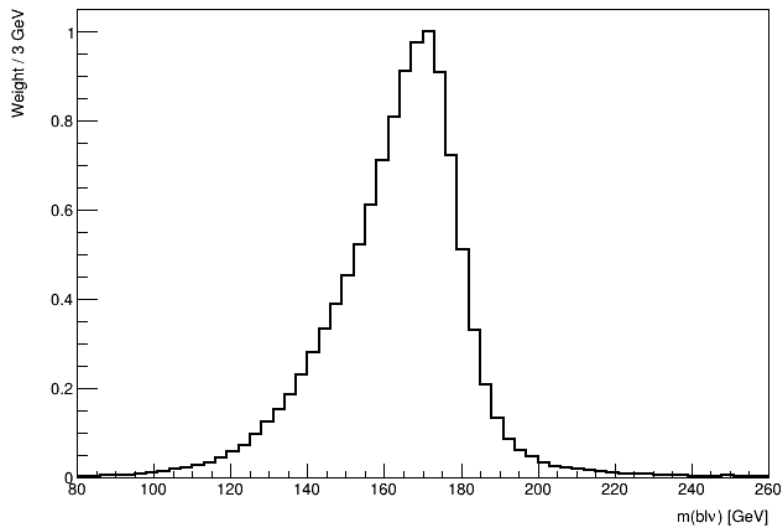


Figure 4.30: $m_{b\ell\nu}$ distribution generated from simulated $t\bar{t}$ events, used to calculate $P_{m_{t_1}}$ and $P_{m_{t_2}}$ is shown. The $m_{b\ell\nu}$ distribution is shown by the black lined histogram. The mass of the $b\ell\nu$ system is shown on the x-axis. The corresponding weight of the $m_{b\ell\nu}$ distribution is shown on the y-axis.

4.8.2.2 $P_{\Delta E_x}$ and $P_{\Delta E_y}$

A similar method is used to determine $P_{\Delta E_x}$ and $P_{\Delta E_y}$. In this case we generate a weight distribution of $\Delta E_x = (p_{T,\nu_1})_x + (p_{T,\nu_2})_x - (E_T^{\text{miss}})_x$ based off simulated $t\bar{t}$ events. In particular, this distribution is generated using reco-level E_T^{miss} and generator-level neutrinos. The use of this distribution lies under the assumption that neutrinos are the dominant source of E_T^{miss} , and therefore, $(E_T^{\text{miss}})_x \approx (p_{T,\nu_1})_x + (p_{T,\nu_2})_x$ and $(E_T^{\text{miss}})_y \approx (p_{T,\nu_1})_y + (p_{T,\nu_2})_y$. We then use the distribution to interpolate the value of ΔE_x and ΔE_y from our reconstructed neutrinos. This returns a weight value from 0 to 1, with higher values corresponding to ΔE_x and ΔE_y (and in turn our reconstructed neutrino's p_T) closer to those observed in a $t\bar{t}$ event. We expect the ΔE_x and ΔE_y distributions to have the same shapes, therefore we only need to generate one (we have chosen ΔE_x). In Figure 4.32, the $m_{b\ell\nu}$ distribution (generated from simulated $t\bar{t}$ events), used to calculate $P_{m_{t_1}}$ and $P_{m_{t_2}}$ is shown.

4.8.3 Kinematic Vetoos

The $2\nu SM$ algorithm is extremely computationally intensive. The computation time depends on the number step size of the ϕ and η ranges which we scan over to reconstruct the neutrinos. For example, consider the step sizes chosen in this analysis, $\Delta\eta \approx 0.31$ and $\Delta\phi \approx 0.25$ which corresponds to 32 values for η and 25 values for ϕ . There

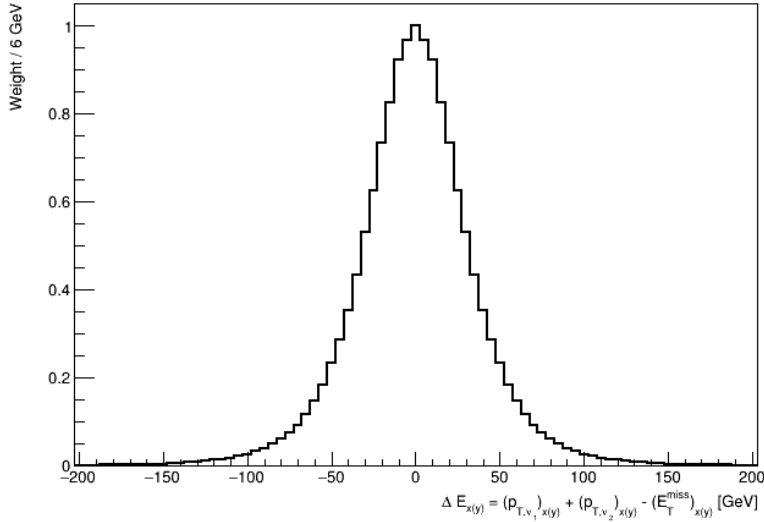


Figure 4.31: ΔE_x distribution generated from simulated $t\bar{t}$ events, used to calculate $P_{\Delta E_x}$ and $P_{\Delta E_y}$ is shown. The ΔE_x distribution is shown by the black lined histogram. ΔE_x is shown on the x-axis. The corresponding weight of ΔE_x distribution is shown on the y-axis.

will be $(32)(32)(25) = 640\,000$ possible pairs of neutrinos (ν_1 and ν_2) to consider **per event**. Since we have to consider two possible $t\bar{t}$ systems (See Equations 4.7 and 4.8), this number effectively increases to $(2)(640000) = 128\,000$ iterations **per event**. In order to reduce the number of $t\bar{t}$ systems we need to consider, therefore decreasing computation time, we look at distributions of well modelled observables from $t\bar{t}$ events and veto (discard) a possible reconstructed $t\bar{t}$ system if the observable in question is improbable or unlikely to be observed in a $t\bar{t}$ event. To achieve this, we define a threshold range for these observables, and if the possible reconstructed $t\bar{t}$ system's corresponding value for this observable lies outside this range, it is vetoed and the algorithm continues with the next iteration.

4.8.3.1 $\Delta\langle m(\ell b) \rangle$

The first observable which we consider is the difference between average mass of the two possible ℓb system combinations, $\Delta\langle m(\ell b) \rangle$. The two possible ℓb system combinations are,

$$(\ell b)_1 = \ell_1 + b_1 \text{ and } (\ell b)_2 = \ell_2 + b_2 \quad (4.10)$$

OR

$$(\ell b)_1 = \ell_1 + b_2 \text{ and } (\ell b)_2 = \ell_2 + b_1 \quad (4.11)$$

$$(4.12)$$

$\Delta\langle m(\ell b) \rangle$ is therefore defined as,

$$\Delta\langle m(\ell b) \rangle = \frac{1}{2} |[(m(\ell_1 b_1) + m(\ell_1 b_1)) - (m(\ell_1 b_2) + m(\ell_2 b_1))| \quad (4.13)$$

The idea here is that, if $\Delta\langle m(\ell b) \rangle$ is large, it's more likely that we can simply select the ℓb combination with the smaller (minimum) average mass. To illustrate this, we look at the distribution (constructed from $t\bar{t}$ events) of $P(\text{Correct combination of } \ell b \text{ systems} | \text{minimum}\langle m(\ell b) \rangle)$ vs $\Delta\langle m(\ell b) \rangle$ for b -tagged jets in the same ($\eta(b_1) \times \eta(b_2) \geq 0$) and opposite hemispheres ($\eta(b_1) \times \eta(b_2) < 0$).

In Figure 4.33 the $P(\text{Correct combination of } \ell b \text{ systems} | \text{minimum}\langle m(\ell b) \rangle)$ vs $\Delta\langle m(\ell b) \rangle$, for b -tagged jets in the same and opposite hemispheres, constructed from $t\bar{t}$ events is shown.

From the Figure above, for both cases where the b -tagged jets are in the same and opposite hemispheres, the probability for a correct ℓb system being chosen given that we are considering the ℓb system with minimum average mass is an increasing function which plateaus to 1 at ~ 90 GeV. We use these two distributions to interpolate the $P(\text{Correct combination of } \ell b \text{ systems} | \text{minimum}\langle m(\ell b) \rangle)$ from $\Delta\langle m(\ell b) \rangle$. We require that $P(\text{Correct combination of } \ell b \text{ systems} | \text{minimum}\langle m(\ell b) \rangle) > 0.8$, before vetoing any ℓb combination, such that we

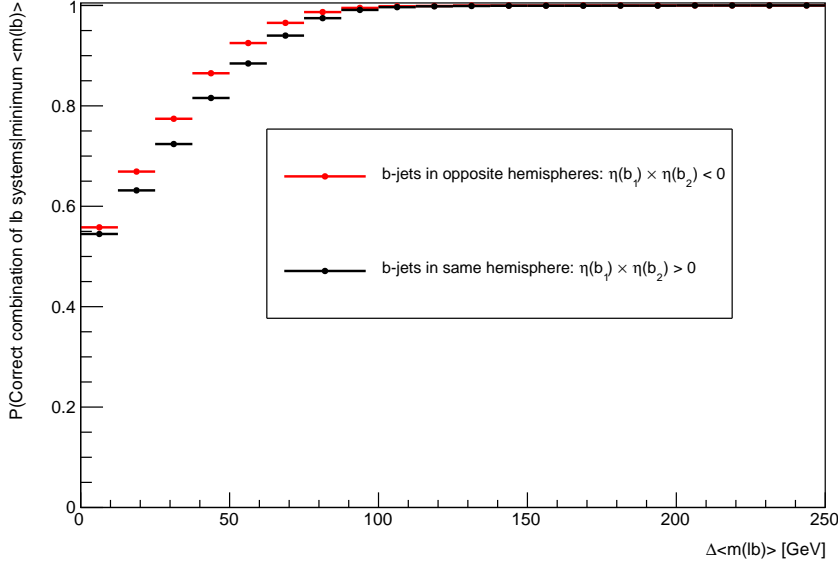


Figure 4.32: $P(\text{Correct combination of } \ell b \text{ systems} | \text{minimum}\langle m(\ell b) \rangle)$ vs $\Delta\langle m(\ell b) \rangle$, for b -tagged jets in the same and opposite hemispheres, constructed from $t\bar{t}$ events is shown. The horizontal red lines represent the distribution in the case when the two b -jets are in opposite hemispheres. The dot in the middle of the line represents the midpoint of the line. The horizontal black lines represent the distribution in the case when the two b -jets are in the same hemispheres. The dot in the middle of the line represents the midpoint of the line. The average $m(\ell b)$ is shown on the x-axis. The $P(\text{Correct combination of } \ell b \text{ systems} | \text{minimum}\langle m(\ell b) \rangle)$ is shown on the y-axis.

have are at least 80% certain that we know the correct ℓb combination. In this case, the ℓb combination with the maximum $\Delta\langle m(\ell b) \rangle$ is vetoed. If $P(\text{Correct combination of } \ell b \text{ systems} | \text{minimum}\langle m(\ell b) \rangle) < 0.8$ we need to consider both possible ℓb system combinations.

4.8.3.2 $\eta(b\bar{b}\ell\ell)$

We consider η of the $b\bar{b}\ell\ell$ system, $\eta(b\bar{b}\ell\ell)$ to veto improbable $\eta(\nu_1)$ and $\eta(\nu_2)$ values.

In the same way as for $\Delta\langle m(\ell b) \rangle$, we generate a distribution to determine values $\eta(\nu)$ which are improbable for a $t\bar{t}$ event. In this case, we generate a 2D histogram from simulated $t\bar{t}$ events (dileptonic final state) at generator-level of $\eta(\nu)$ vs $\eta(b\bar{b}\ell\ell)$.

In Figure 4.34, a heatmap of occupancy for $\eta(\nu)$ vs $\eta(b\bar{b}\ell\ell)$ (produced from simulated $t\bar{t}$ events) is shown. Using the above heatmap, we define a veto region (where a $t\bar{t}$ event is extremely unlikely to occur) based off double-sided 95% limits (**something here on confidence limit??**). We apply a veto if either possible neutrino lies within this region. The veto region is shown in Figure 4.35.

In Figure 4.35, the veto region (extracted from Figure 4.34) for vetoing improbable neutrinos is shown.

4.8.3.3 L_T

The final kinematic constraint which we consider is the scalar sum of lepton p_T , $L_T = p_T(\ell_1) + p_T(\ell_2)$ which we use to veto certain possible neutrinos, ν_1 and ν_2 .

Again, we generate a distribution to determine (and veto) improbable possible neutrinos in simulated $t\bar{t}$ events (dilepton final state).

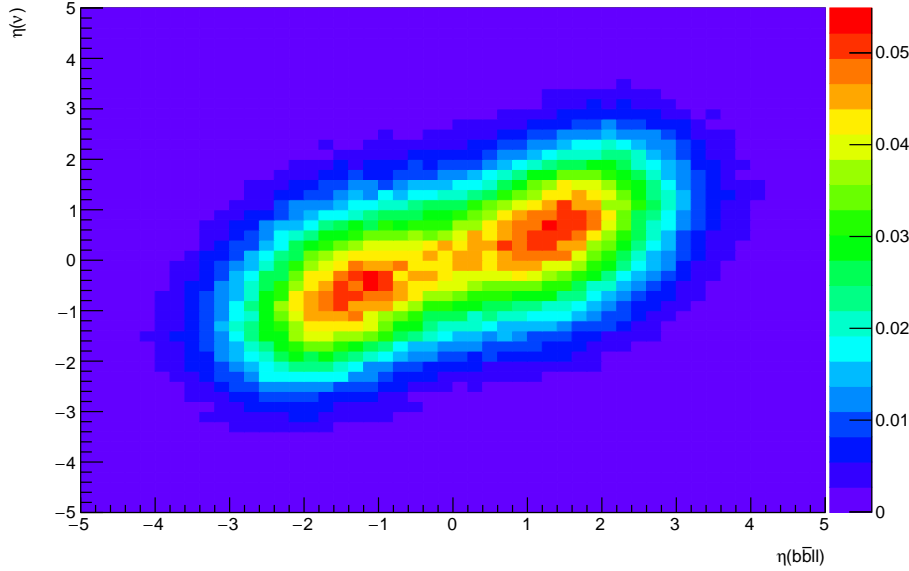


Figure 4.33: Heatmap of occupancy for $\eta(\nu)$ vs $\eta(b\bar{b}\ell\ell)$ produced from simulated $t\bar{t}$ events (dileptonic final state) at generator-level is shown. η of the $b\bar{b}\ell\ell$ system is shown on the x-axis. η of the neutrino is shown on the y-axis. The colorbar on the right represents the occupancy (normalised) in the phase space.

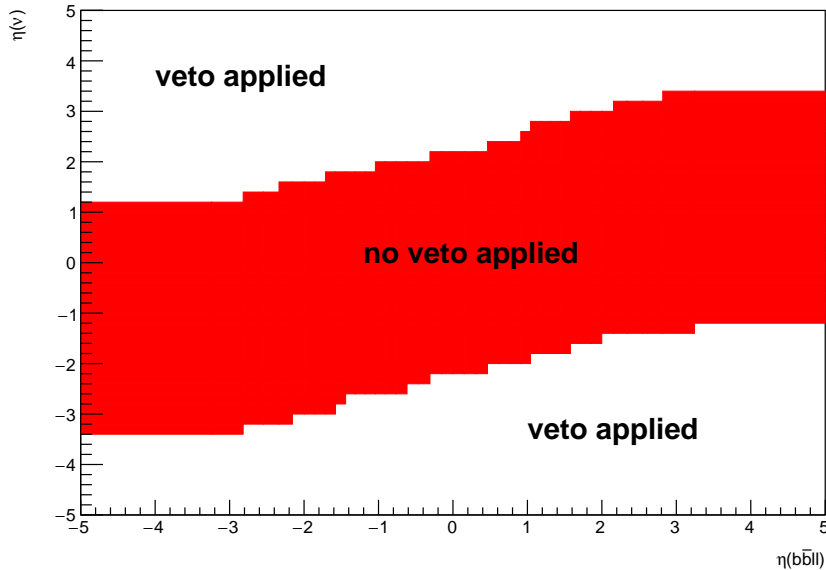


Figure 4.34: The regions where vetoes are applied for the $\eta(b_1 b_2 \ell_1 \ell_2)$ constraint is shown. η of the $b\bar{b}\ell\ell$ system is shown on the x-axis. η of the neutrino is shown on the y-axis. The red band shows the region where the neutrino would not be vetoed. The white areas (above and below the red band) are regions where the neutrino is vetoed.

In Figure 4.36, a heatmap of occupancy for $\Delta R(\ell, \nu)$ vs L_T (produced from simulated $t\bar{t}$ events) is shown. Using the same method as described in Section 4.8.3.2, we define a veto region where a veto is applied if either possible neutrino lies within this region. In Figure 4.35, the veto region (extracted from Figure 4.36) for vetoing improbable neutrinos values is shown.

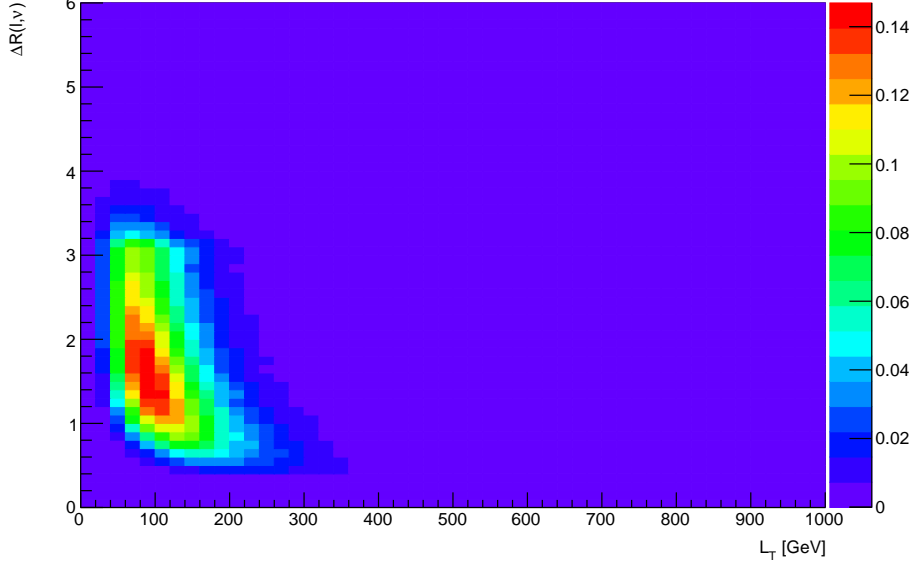


Figure 4.35: A heatmap of occupancy for $\Delta R(\ell, \nu)$ vs L_T produced from simulated $t\bar{t}$ events (dileptonic final state) at generator-level is shown. ΔR between leptons and neutrinos is shown on the x-axis. L_T (scalar sum of lepton p_T) is shown on the y-axis. The colorbar on the right represents the occupancy (normalised) in the phase space.

4.9 Systematics

The systematic uncertainties can be separated into experimental (detector) systematics, which are related to the reconstruction of physics objects in the detector and theoretical uncertainties related to the modelling of the different processes background.

4.9.1 Experimental uncertainties

In this section, the experimental systematics are outlined.

- **Luminosity:**

The 2015–2018 luminosity estimate of 139fb^{-1} has a relative uncertainty of 3%. This uncertainty is obtained using the LUCID-2 detector [17] for the primary luminosity measurements. This systematic uncertainty affects all processes modelled using MC simulations.

- **Pile-up reweighting:**

An uncertainty related to the SFs used for MC to account for differences in pile-up distributions between MC and data is applied. This uncertainty is obtained by re-scaling the $\langle\mu\rangle$ value in data by 1.00 and 1/1.18 corrections are only applied to MC.

- **Jet vertex tagger:**

Uncertainties associated to the JVT are applied via the `JetJvtEfficiency` package [15] which account for the residual contamination from pile-up jets after pile-up suppression and the MC generator choice [9].

- **Heavy- and light-flavor tagging:**

The efficiency of the flavour-tagging algorithm is measured for each jet flavour using control samples in data and in simulation. From these measurements, correction factors are derived to correct the tagging rates in the simulation. In the case of b -tagged jets, the correction factors and their uncertainties are estimated from data using dileptonic $t\bar{t}$ events [11, 6]. In the case of c -jets, they are derived from jets arising from W boson decays in $t\bar{t}$ events [10]. In the case of light-flavour jets, the correction factors are derived using dijet events [7]. Sources of uncertainty affecting the b - and c -tagging efficiencies are evaluated as a function of jet p_T , including bin-to-bin correlations. The uncertainties in the efficiency for tagging light-flavour jets depend on the jet p_T

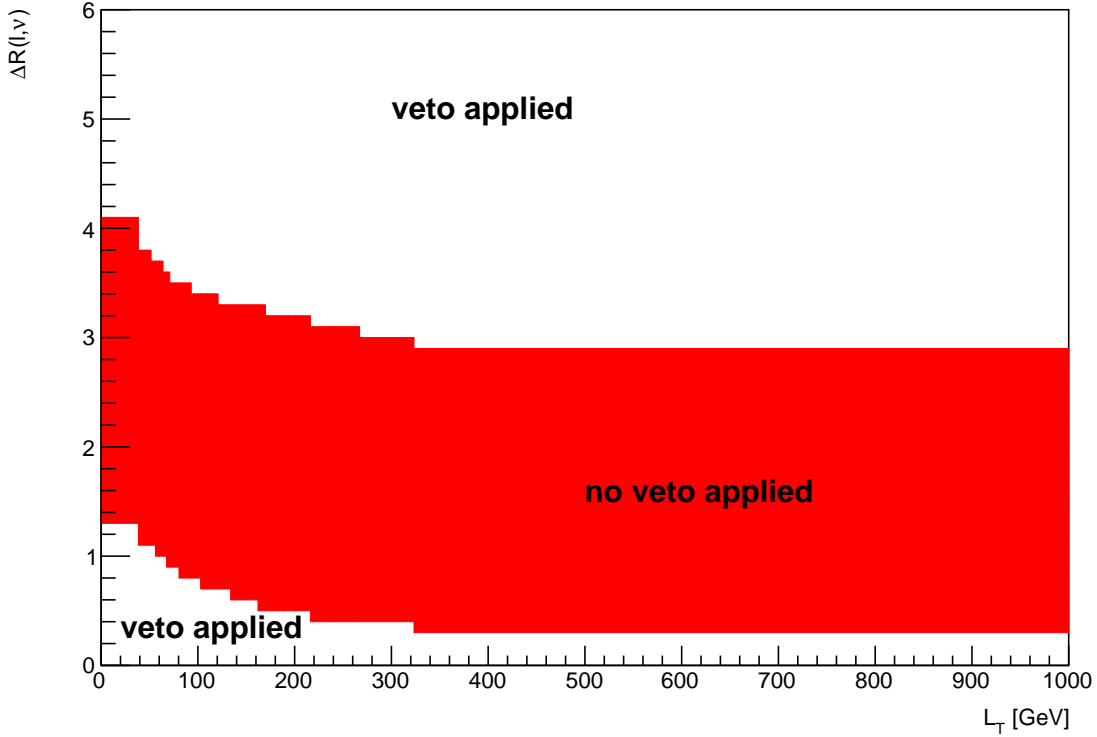


Figure 4.36: The regions where vetoes are applied for the L_T constraint is shown. ΔR between leptons and neutrinos is shown on the x-axis. L_T (scalar sum of lepton p_T) is shown on the y-axis. The red band shows the region where the neutrino would not be vetoed. The white areas (above and below the red band) are regions where the neutrino is vetoed.

and on η . An additional uncertainty is assigned to account for the extrapolation of the b -tagging efficiency measurement from the p_T region used to determine the correction factors to regions with higher p_T .

- **Electron efficiency:**

Uncertainties associated with the electron efficiency SFs are provided by the egamma CP group [13] and arise from the reconstruction, ID, isolation and trigger efficiencies. They correct for the efficiency difference between data and MC [8] and are measured with a “tag-and-probe” method in $Z \rightarrow e^+e^-$ and $J/\psi \rightarrow e^+e^-$ events. The information on the correlation of the different components of the systematic uncertainties are provided for all efficiency measurements. The default correlation model for the uncertainties is used, which provides one up/down variation for each of the SF components separately [13, 14].

- **Muon efficiency:**

As for electrons, SFs obtained from $Z \rightarrow \mu^+\mu^-$ and $J/\psi \rightarrow \mu^+\mu^-$ events are applied to correct for the differences between data and MC in the muon ID, isolation and trigger efficiencies [12]. Uncertainties on these SFs are provided by the muon CP group [16] and applied as up/down variations of the nominal SFs for each component.

4.9.2 Theoretical uncertainties

In this section, the theoretical systematics are outlined.

- **$t\bar{t}Z$ background:**

An overall normalization uncertainty of 10% is considered for the $t\bar{t}Z$ background. Two generic shape systematics are considered for the $t\bar{t}Z$ background. They are constructed (see Section 4.9.3) by either applying

a linear or triangular interpolation to up and down variations which are defined to be $\pm 20\%$ from the nominal $t\bar{t}Z$ background.

- **ZZ background:**

An overall normalization uncertainty of 30% is considered for the ZZ background.

- **$t\bar{H}$ background:**

An overall normalization uncertainty of 20% is considered for the $t\bar{H}$ background.

- **tZq background:**

An overall normalization uncertainty of 14% is considered for the tZq background.

- **$t\bar{t}Z$ fake background:**

An overall normalization uncertainty of 50% is considered for the $t\bar{t}Z$ fake background.

- **other background processes:**

The ‘other’ background consists of many processes which have minimal but non-negligible contribution in the signal regions (See Section 4.1.2). An overall normalization uncertainty of 30% is considered for the ‘other’ background processes.

- **tWZ background:** A modelling uncertainty on tWZ is considered by comparing the nominal sample (using the DR1 scheme) and a minimal DR2 sample.

Two generic shape systematics are considered for the tWZ background. They are constructed (see Section 4.9.3) by either applying a linear or triangular interpolation to up and down variations which are defined to be $\pm 20\%$ from the nominal tWZ background.

4.9.3 Generic shape systematics

It is evident that the tetralepton channel is statistically limited. We therefore expect that the uncertainty on u_{tWZ} is dominated by statistical uncertainty and that the impact of shape systematics will be negligible in comparison.

In order to include shape uncertainties related to the modelling of our samples, we construct generic shape systematics for any given sample process. Given that we choose a sufficiently large set of values for which the systematics can take in the fit, the constructed systematics could represent many shape systematics which we have not yet considered to include in the fitting procedure.

We start by constructing an envelope (error bars) consisting of two MC templates. One with the nominal MC template increased by 20% on its normalisation and the other with the nominal MC template decreased by 20% on its normalisation. The templates are then modified from their original shape either by doing linear interpolation (from the leftmost-up variation to the rightmost-down variation) or triangular interpolation (shape is set to zero at the rightmost and leftmost parts and reaches the envelope in the middle). The linear and triangular interpolation is done using TRF’s `ForceShape` option [35]. This envelope now represents the bounds which the systematic can vary in the fit.

In Figure ?? the envelope before and after the shape change, for both the linear and triangular interpolations, for the $t\bar{t}Z$ background in the $t\bar{t}Z$ CR is shown.

We consider two shape systematics (linear and triangular shapes) for tWZ and the most dominant background processes across both channels. In particular, we consider these shape systematics for $t\bar{t}Z$ for both the tri- and tetralepton channels. Additionally, we consider these shape systematics for the $WZ + b$ and $WZ + c$ backgrounds in the trilepton channel.

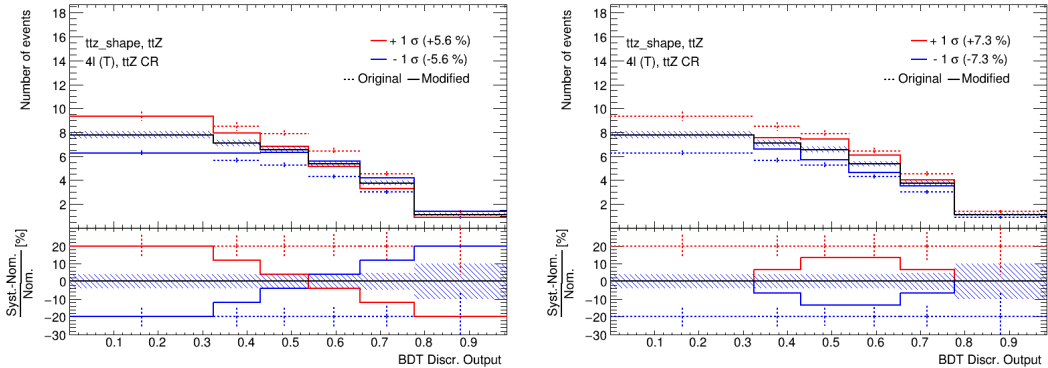


Figure 4.37: $t\bar{t}Z$ generic shape systematic before (original) and after (modified) linear (left) and triangular (right) interpolation in the $t\bar{t}Z$ CR is shown. The output from the event-level BDT shown on the x-axis. In the upper panel, the number of events is shown on the y-axis. In the lower panel, the difference between the systematic variation (the envelope's templates) and the nominal template, divided by the nominal template, is shown on the y-axis. The nominal $t\bar{t}Z$ template is shown by the solid black lined histogram, with the diagonal lined bands representing its total uncertainty. The templates of the upper and lower envelopes (before modification) is given by the dotted red and blue lined histograms respectively. The templates of the upper and lower envelopes (after modification) is given by the solid red and blue lined histograms respectively, with the vertical dotted lines representing its total uncertainty.

4.10 Analysis Pipeline and TRexFitter

We make use of industry standard **ROOT**³ wrappers in this analysis, namely, **PyROOT** and **TRexFitter**.

Python is used extensively in many fields of science (not limited to physics and data science) due to its simplicity and ongoing support by the communities which utilize it. **PyROOT** allows users to access the full **ROOT** functionality within Python. More specifically, **PyROOT** provides Python bindings for **ROOT**.

TRexFitter is a framework for binned template profile likelihood fits[40]. In this analysis, we used **TRexFitter** (tag: **TRexFitter-00-04-13**) to produce all pre-fit and post-fit plots (including fit statistics, e.g. limit, significance, $\mu_{best-fit}$).

The analysis pipeline starts with sample derivations (derived dataset) being submitted to the grid for ntuple production. This applies cuts and selections to the already reduced derivations and produces ntuples with trees containing variables (e.g. scale factors, observables, MC truth flags) that will be used at future stages in the analysis. These ntuples are then read by **PyROOT** where the events are looped over, before being written to **ROOT** files as input to **TRexFitter**. The Python scripts are used to define the different regions and apply the final cuts and selections outlined in Table 4.3. In addition to this purpose, they are used to train the two BDTs and to produce the output from these trained BDTs. As each event is looped over, the cuts and selection criteria are checked for the given event and is either thrown away (if the event does not pass the selection criteria), or gets written to a **ROOT** file (if the event passes the selection criteria) corresponding to the MC sample and Run 2 data-set (mc16a, mc16d, mc16e) which it belongs to. These **ROOT** files contain all observables, weights and scale factors (corresponding to an event) which we wish to use in **TRexFitter**. **TRexFitter** then takes these files as input, runs a maximum likelihood fit and produces relevant plots (e.g. pre-fit, post-fit, pull plots) and statistical parameters (e.g. limit, significance, $\mu_{best-fit}$).

4.10.1 Fitting Procedure

Using the **TRexFitter** framework, binned profile-likelihood fits are performed to determine the signal strength $\mu_{tWZ} = \sigma_{obs}(tWZ)/\sigma_{SM}(tWZ)$ of tWZ production. A fit across all regions in the tetralepton channel is performed to determine the sensitivity tWZ in this channel. In Section 4.11.2, a combined fit is performed across all regions in the trilepton and tetralepton channels to take advantage of the sensitivity of tWZ in both channels in order to

³CERN’s HEP data analysis framework (written in C++)

further boost the sensitivity of tWZ .

In the separate and combined fits, the *mixed data and MC* fit setup [41] is used. This is done to obtain the most accurate prediction of the expected results while keeping the signal regions blinded. For this setup, first a background-only fit to the control regions using real data is done to determine estimates of the nuisance parameters. Then these estimates are used to construct a modified ASIMOV dataset in the signal regions. Finally, the fit is performed using real data in the control regions and the aforementioned modified ASIMOV data-set in the signal regions.

In these fits, the parameter of interest (POI) is μ_{tWZ} . The POI is ultimately the quantity which we wish to measure and is set as a free parameter (unconstrained; can take any value in the fit). The nuisance parameters are assigned to the systematic uncertainties outlined in 4.9. Furthermore, a gamma (γ) nuisance parameter for a bin is added to the likelihood function if the statistical uncertainty in the bin exceeds 0.1% of its nominal value.

Pruning is done per sample and per region on the shape and normalisation uncertainties for samples. A sample's shape and normalisation nuisance parameter is pruned (removed from the limit/fit) if the fraction of signal yield to the total yield (signal + background) is less than 0.01.

An auto-binning algorithm, `TransfoD` [18], was used to define the binning. This aims to maximise $\frac{\text{signal}}{\text{background}}$ in each bin. Furthermore, it aims to avoid defining bins with a low number of events.

4.11 Results

In the section, an expected upper limit and an expected significance are set on the cross section of tWZ . This is performed for the current analysis in the tetralepton channel as well as for a combined analysis across the trilepton and tetralepton channels. The trilepton analysis was performed as an independent study by Benjamin Warren (UCT). Note that throughout this section, all signal regions remain blinded.

4.11.1 Tetralepton Channel

In Figure 4.25 pre-fit distributions for the variables used in the likelihood fit in each region are shown.

In Figure 4.39 post-fit distributions for the variables used in the likelihood fit in each region are shown.

In Table 4.9, the post-fit yields for each sample in each region is shown.

	tWZ OF SR	tWZ SF SR	$t\bar{t}Z$ CR	ZZb CR	$(tWZ)_{\text{fake}}$ CR
$t\bar{t}Z$	13.2379 ± 1.52295	9.62061 ± 1.12291	29.9054 ± 3.60908	5.08899 ± 0.620121	18.5393 ± 2.23036
$t\bar{t}Z$ fakes	0.0702522 ± 0.0468691	0.0334067 ± 0.0256903	0.0723509 ± 0.0418526	0.0485273 ± 0.029133	5.04378 ± 2.34732
tWZ	7.83414 ± 3.31679	5.33547 ± 2.24801	5.69373 ± 2.58041	2.89889 ± 1.23837	10.278 ± 4.3345
ZZ	0.481776 ± 0.119774	7.72372 ± 1.2351	1.07955 ± 0.182461	40.6067 ± 6.26078	6.86097 ± 1.11443
other	tt	$6.00553e-06 \pm 3.02819e-06$	0.252557 ± 0.442116	0.273507 ± 0.223201	$6.00553e-06 \pm 3.02819e-06$
	tZq	0.0827905 ± 0.0398773	0.0756107 ± 0.0354584	0.063585 ± 0.0293325	0.05884 ± 0.0244084
	$tttW$	$0.00668643 \pm 0.00792217$	$0.00279748 \pm 0.00287361$	$6.00553e-06 \pm 3.02819e-06$	0.002306 ± 0.00564349
	WZ	0.0442934 ± 0.024156	0.0396511 ± 0.0154282	0.0133471 ± 0.0128199	0.0472562 ± 0.0330315
	ttt	$0.000987164 \pm 0.000766266$	$0.00247481 \pm 0.00136945$	0.0140869 ± 0.00479496	$6.00553e-06 \pm 3.02819e-06$
	$tttt$	0.00934035 ± 0.0080554	0.0107458 ± 0.00849984	0.0571373 ± 0.0204011	$6.00553e-06 \pm 3.02819e-06$
	$ttWW$	0.0294618 ± 0.0263174	0.029771 ± 0.0195582	0.264364 ± 0.0926252	0.0129431 ± 0.0323803
	$VVV(V = W/Z)$	0.280643 ± 0.0853411	0.191433 ± 0.0586778	0.0697266 ± 0.0225059	0.171142 ± 0.0518102
	ttH	0.846054 ± 0.175495	0.669375 ± 0.140107	1.96662 ± 0.401199	0.150025 ± 0.0353826
Total	22.9243 ± 2.96284	23.9876 ± 2.11249	39.4734 ± 3.44937	49.0856 ± 6.04162	53.4282 ± 4.31683
data	-	-	36	49	57

Table 4.9: The post-fit yields for each sample in each region is shown.

The expected upper limit of tWZ in the tetralepton channel is measured as,

$$\mu_{up}^{exp} = 1.60^{+2.34}_{-1.15} \quad (4.14)$$

The expected significance of tWZ in the tetralepton channel is measured as,

$$Z_\mu^{exp} = 1.43\sigma \quad (4.15)$$

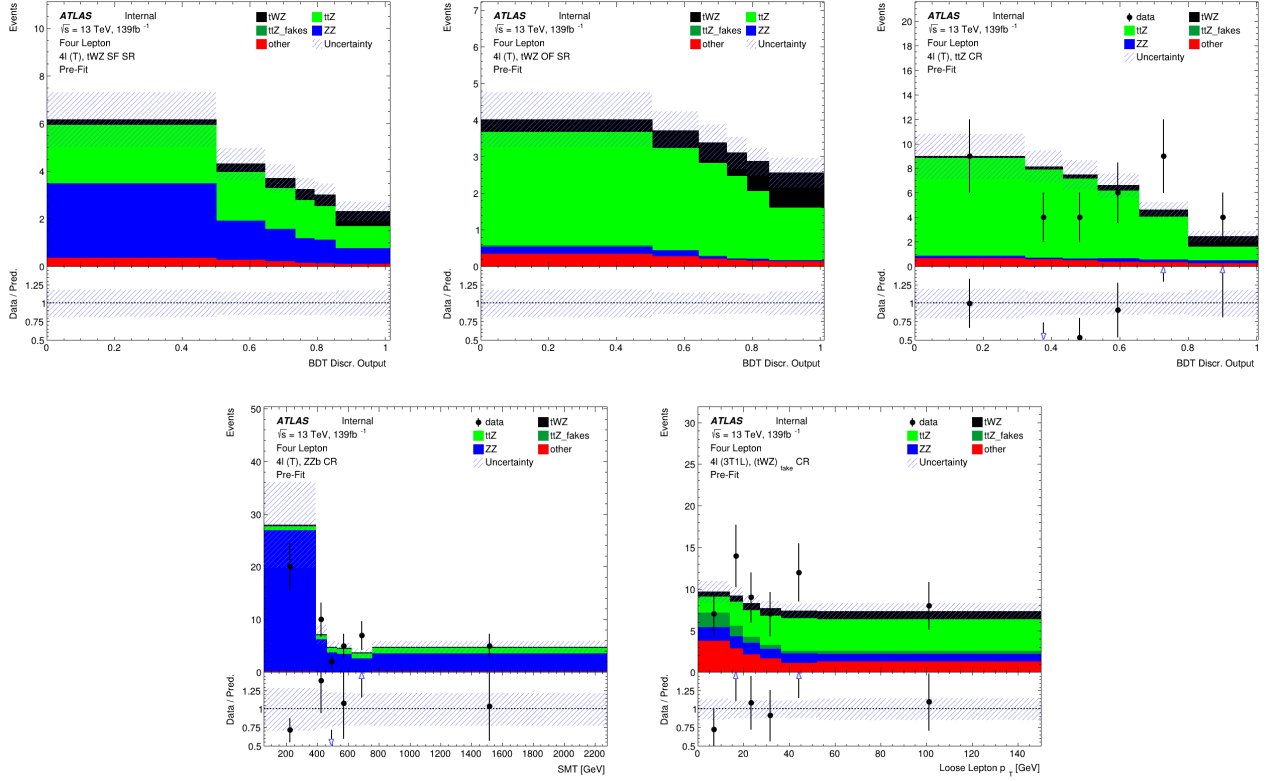


Figure 4.38: Pre-fit distributions (blinded) of variables used in the fit are shown. The data is given by the black points and the MC predictions for each process are given by the histograms. The vertical lines on the data points represent the total uncertainty in the data and the diagonal lined bands represent the total MC uncertainty. The lower panel in each plot shows the ratios of the data to the theoretical predictions. The plots in the tWZ OF SR and tWZ SF SR are kept blinded by omitting the data points. **Top left:** The event-level BDT Disc. Output in the tWZ SF (4T) SR region is shown. **Middle top:** The event-level BDT Disc. Output in the tWZ SF (4T) SR region is shown. **Top right:** The event-level BDT Disc. Output in the $t\bar{t}Z$ CR region is shown. **Bottom left:** $SMT = \sum p_T(\ell) + \sum p_T(\text{jet}) + E_T^{\text{miss}}$ in the ZZb CR is shown. **Bottom right:** p_T (loose lepton) in the $(tWZ)_{\text{fake}}$ (3T1L) CR is shown.

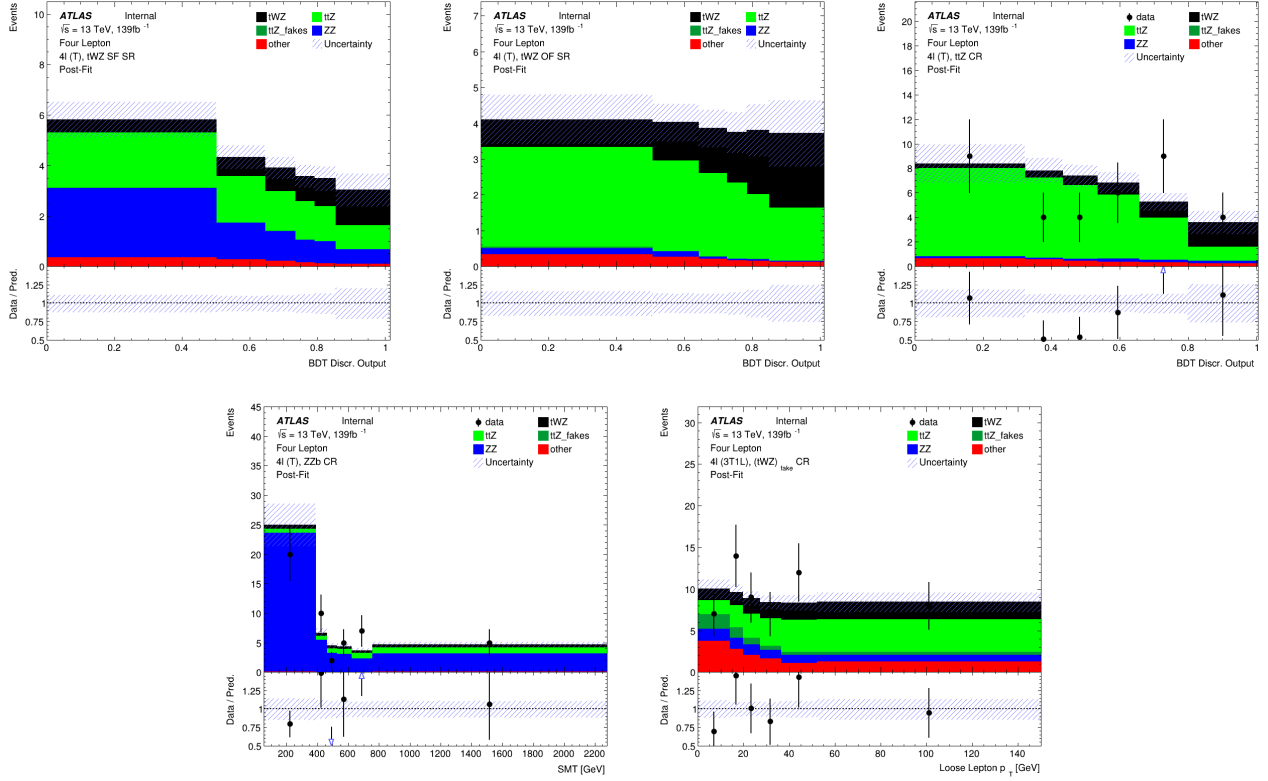


Figure 4.39: Post-fit distributions (blinded) of variables used in the fit are shown. The data is given by the black points and the MC predictions for each process are given by the histograms. The vertical lines on the data points represent the total uncertainty in the data and the diagonal lined bands represent the total MC uncertainty. The lower panel in each plot shows the ratios of the data to the theoretical predictions. The plots in the tWZ OF SR and tWZ SF SR are kept blinded by omitting the data points. **Top left:** The event-level BDT Disc. Output in the tWZ SF (4T) SR region is shown. **Middle Top:** The event-level BDT Disc. Output in the tWZ SF (4T) SR region is shown. **Top right:** The event-level BDT Disc. Output in the $t\bar{t}Z$ CR region is shown. **Bottom left:** $SMT = \sum p_T(\ell) + \sum p_T(jet) + E_T^{\text{miss}}$ in the ZZb CR is shown. **Bottom right:** $p_T(\text{loose lepton})$ in the $(tWZ)_{\text{fake}}$ (3T1L) CR is shown.

The best-fit value of the signal strength, $\mu(tWZ) = \frac{\sigma(tWZ)}{\sigma(tWZ)_{SM}}$, from the likelihood fit is measured as,

$$\mu(tWZ) = 2.18^{+0.99}_{-0.85} \quad (4.16)$$

The expected upper limit is in agreement with the extracted best-fit value on the signal strength, therefore no deviations from the SM cross section of tWZ is observed. Neither the 3σ evidence nor the 5σ discovery standards are reached for the expected significance. This is not surprising, given the low amount of events present in the tetralepton channel.

In Figure 4.40, a ranking plot showing the impact of the systematic uncertainties on the POI, $\mu(tWZ)$ is shown.

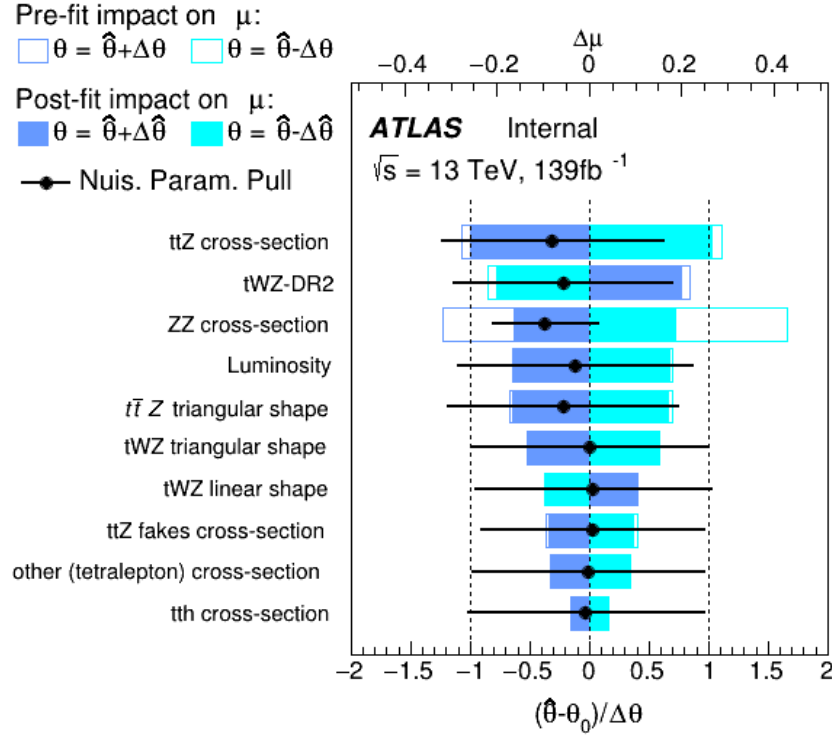


Figure 4.40: A ranking plot showing the impact (ordered from top to bottom via decreasing impact) of the systematic uncertainties (top 10) on the POI, $\mu(tWZ)$, in the tetralepton channel is shown. $\hat{\theta}$ is the best-fit value of the nuisance parameter. $\Delta\hat{\theta}$ and $\Delta\theta$ are the post-fit and pre-fit uncertainties respectively. The post-fit and pre-fit impact of each nuisance parameter on $\mu(tWZ)$ are shown with the solid and lined rectangles respectively. The empty and solid blue rectangles correspond to the pre-fit and post-fit impacts on $\mu(tWZ)$ respectively. These impacts are shown on the upper axis ($\Delta\mu$). On the lower axis, the nuisance parameter pull, $\frac{\hat{\theta}-\theta_0}{\Delta\theta}$, is shown (θ_0 is the nominal pre-fit value of the nuisance parameter). The nuisance parameter pull is indicated by the black points, with their relative post-fit errors ($\frac{\Delta\hat{\theta}}{\Delta\theta}$) shown by the black horizontal error bars.

Some nuisance parameters are pulled down from their nominal pre-fit values, however these are all within 1σ uncertainty and are thus relatively small. It is expected that the modelling uncertainties (shape and normalisations) of the most dominant backgrounds (e.g. $t\bar{t}Z$, ZZ) have relatively large impacts on $\mu(tWZ)$, since the uncertainty of the analysis is dominated by statistical uncertainty.

4.11.2 Trilepton and Tetralepton Channels

In the section, an expected upper limit and an expected significance are set on the cross section of tWZ from the combined fit across all regions of tWZ in the tetralepton and trilepton channels.

The trilepton analysis follows a similar analysis strategy to that of the tetralepton analysis. It includes an event-level BDT which aims to discriminate between the tWZ and all background as well as an object-level

Nuisance Parameter	Channel Affected	
	trilepton	tetralepton
$\sigma(t\bar{t}H)$	✓	✓
$\sigma(t\bar{t}Z)$	✓	✓
$\sigma(WZ)$	✓	✓
$\sigma(tZq)$	✓	✓
$\sigma(ZZ)$	✓	✓
$\sigma(\text{other(trilepton)})$	✓	✗
$\sigma(\text{other(tetralepton)})$	✗	✓
$\sigma(t\bar{t}Z)_{fakes}$	✗	✓
$\sigma(t\bar{t})_{fakes}$	✓	✗
$\sigma(Z + jets)_{fakes}$	✓	✗
Luminosity	✓	✓
jvt	✓	✓
pileup	✓	✓
DL1r SF (b jets)	✓	✓
DL1r SF (light jets)	✓	✓
$\sigma(tWZ - DR2)$	✗	✓
lepton SF	✓	✓
$t\bar{t}Z$ triangular shape	✓	✓
$t\bar{t}Z$ linear shape	✓	✓
$WZ + b$ triangular shape	✓	✗
$WZ + b$ linear shape	✓	✗
$WZ + c$ triangular shape	✓	✗
$WZ + c$ linear shape	✓	✗

Table 4.10: A summary of the nuisance parameters used in the combined fit is shown. The channels which are affected by each nuisance parameter are indicated with a ✓ (is affected) or a ✗ (is not affected).

BDT which aims to identify hadronically decaying W bosons to discriminate between tWZ and the large WZ background. One tWZ SR is defined and five CRs are defined. WZ and $t\bar{t}Z$ CRs are defined to constrain the dominant WZ and $t\bar{t}Z$ backgrounds. Three CRs which require that one of the three selected leptons are loose, are defined for WZ , $t\bar{t}Z$ and tWZ in order to constraint the fake lepton component (using the MC template method - similar to the method used in Section 4.6 to estimate the fake lepton component).

The expected upper limit of tWZ in the trilepton channel is measured as,

$$\mu_{up}^{exp} = 2.53^{+3.55}_{-1.82} \quad (4.17)$$

The expected significance of tWZ in the trilepton channel is measured as,

$$Z_\mu^{exp} = 0.81\sigma \quad (4.18)$$

The best-fit value of the signal strength, $\mu(tWZ) = \frac{\sigma(tWZ)}{\sigma(tWZ)_{SM}}$, from the likelihood fit is measured as,

$$\mu(tWZ) = 1.27^{+1.32}_{-1.24} \quad (4.19)$$

The expected upper limit is in agreement with the extracted best-fit value on the signal strength, therefore no deviations from the SM cross section of tWZ is observed.

In Table 4.10, the nuisance parameters used in the fit, including which channel's regions are affected by each, are shown.

The expected upper limit of tWZ across both channels is measured as,

$$\mu_{up}^{exp} = 1.43^{+2.04}_{-1.03} \quad (4.20)$$

The expected significance of tWZ across both channels is measured as,

$$Z_\mu^{exp} = 1.56\sigma \quad (4.21)$$

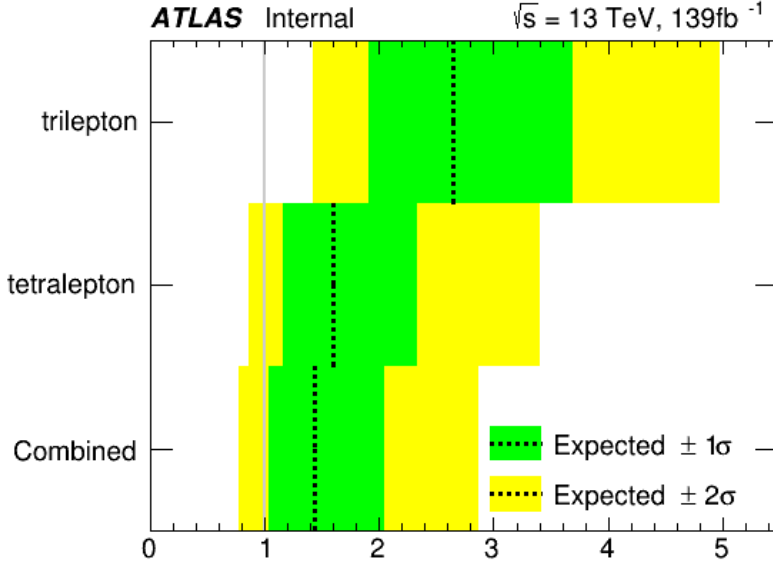


Figure 4.41: The expected upper limits of the trilepton channel, tetralepton channel and both channels combine are shown. The y-axis shows the channels in which the fitting procedure was performed. The expected limits are represented by the vertical dotted line. One- and two- σ uncertainty bands are shown in green and yellow respectively. The vertical grey line indicates when $\mu(tWZ) = 1$.

The best-fit value of the signal strength, $\mu(tWZ) = \frac{\sigma(tWZ)}{\sigma(tWZ)_{SM}}$, from the likelihood fit is measured as,

$$\mu(tWZ) = 2.00^{+0.75}_{-0.70} \quad (4.22)$$

In Figure 4.41, the expected upper limits of the trilepton channel, tetralepton channel and both channels combined are shown.

It can be seen that the sensitivity of tWZ is mostly driven by the tetralepton analysis, with the trilepton analysis attributing a small decrease in the expected upper limit of the combined analysis, and its associated uncertainty.

In Figure 4.42, the best-fit values of $\mu(tWZ)$ from the fit for the trilepton channel, tetralepton channel and both channels combined are shown.

It can be seen from Figures 4.41 and 4.42 that the best fit value for the signal strength on tWZ , $\mu(tWZ)$, and the expected limits for the tri- and tetralepton channels are consistent with one-another (their uncertainties overlap). Therefore it is appropriate to combine these two analyses.

In Figure 4.43, a ranking plot showing the impact of the systematic uncertainties on the POI, $\mu(tWZ)$, in the combined fit across both the tri- and tetralepton channels is shown.

Some nuisance parameters are pulled down from their nominal pre-fit values, however these are all within 1σ uncertainty and are thus relatively small. It is expected that the modelling uncertainties (shape and normalisations) of the most dominant backgrounds (e.g. $t\bar{t}Z$, ZZ , WZ) have relatively large impacts on $\mu(tWZ)$, since the uncertainty of the analysis is dominated by statistical uncertainty.

4.11.2.1 Projection to Higher Luminosity

In this section we apply a fully blinded fit to the ASIMOV dataset for integrated luminosities larger than the 139fb^{-1} currently available from the ATLAS Full Run 2 dataset. This study gives us insight into the sensitivity of tWZ which we could expect if we were to replicate the current analysis, given more data. Given the upgrades planned for the LHC and the ATLAS detector, we will soon expect an large increase in available $p - p$ collision data (reaching $\mathcal{L} = 3000\text{fb}^{-1}$ [19]). This study therefore gives us an idea of the sensitivity of tWZ which we can expect in the future.

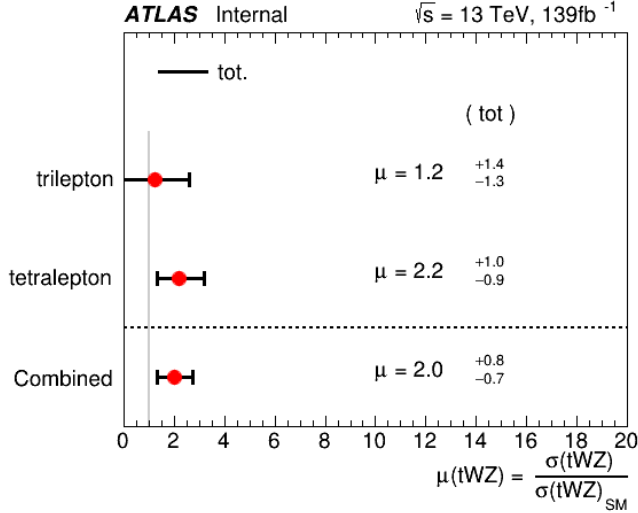


Figure 4.42: The best-fit values of $\mu(tWZ)$ from the fit for the trilepton channel, tetralepton channel and both channels combined are shown. The y-axis shows the channels in which the fitting procedure was performed. The signal strength $\mu(tWZ)$ is shown on the x-axis. The nominal signal strengths are represented by the red dots. The total uncertainty associated with the best-fit $\mu(tWZ)$ value is shown by the black error bars.

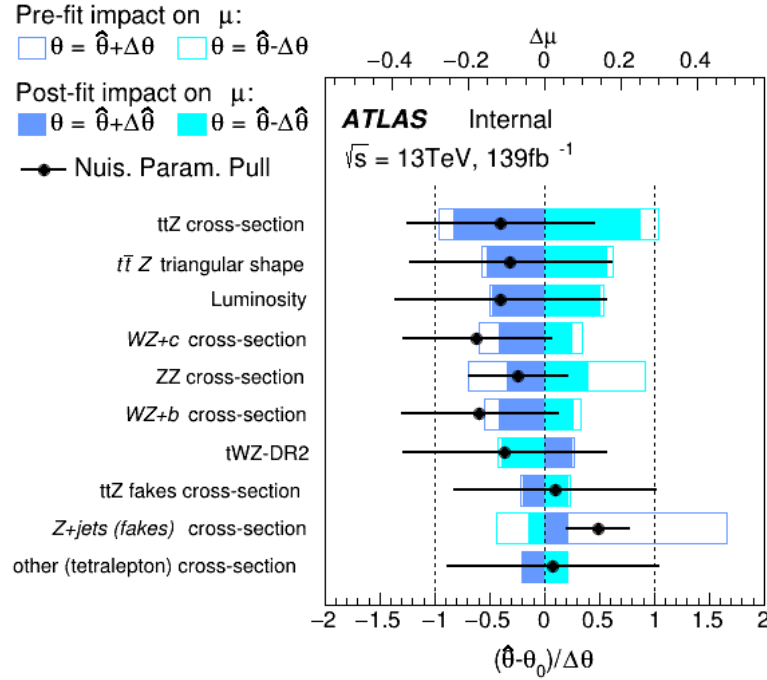


Figure 4.43: A ranking plot showing the impact of the systematic uncertainties (top 10) on the POI, $\mu(tWZ)$, in the combined fit across both the tri- and tetralepton channels is shown. $\hat{\theta}$ is the best-fit value of the nuisance parameter. $\Delta\hat{\theta}$ and $\Delta\theta$ are the post-fit and pre-fit uncertainties respectively. The post-fit and pre-fit impact of each nuisance parameter on $\mu(tWZ)$ are shown with the solid and lined rectangles respectively. The empty and solid blue rectangles correspond to the pre-fit and post-fit impacts on $\mu(tWZ)$ respectively. These impacts are shown on the upper axis ($\Delta\mu$). On the lower axis, the nuisance parameter pull, $\frac{\hat{\theta} - \theta_0}{\Delta\theta}$, is shown (θ_0 is the nominal pre-fit value of the nuisance parameter). The nuisance parameter pull is indicated by the black points, with their relative post-fit errors ($\frac{\Delta\hat{\theta}}{\Delta\theta}$) shown by the black horizontal error bars.

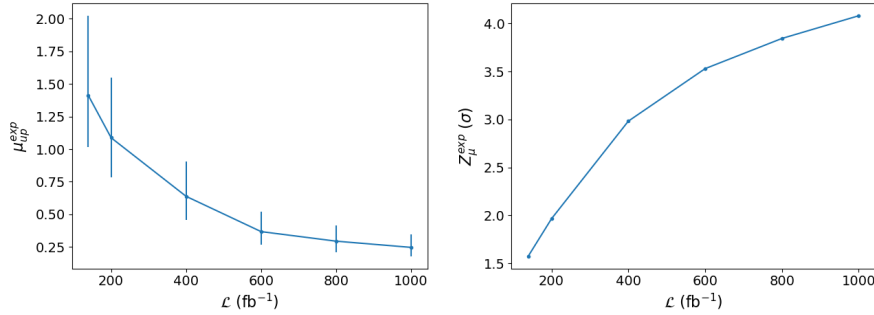


Figure 4.44: The expected upper limit (left) and significance (right) for combined fully blinded fits to the ASIMOV dataset across both the tri- and tetralepton channels for a range integrated luminosities are shown. **Left:** The integrated luminosity, \mathcal{L} , is shown on the x-axis. The expected upper limit, μ_{up}^{exp} , is shown on the y-axis. The vertical lines represent the total uncertainty ($\pm 1\sigma$) on the expected upper limit. **Right:** The integrated luminosity, \mathcal{L} , is shown on the x-axis. The expected significance, Z_μ^{exp} , is shown on the y-axis. The vertical lines represent the total uncertainty ($\pm 1\sigma$) on the expected significance.

In Figure 4.44, the expected upper limit and significance for combined fully blinded fits to the ASIMOV dataset across both the tri- and tetralepton channels for a range integrated luminosities are shown.

As we increase the total integrated luminosity, the sensitivity of tWZ increases. The increase in sensitivity is shown by the decrease of the expected upper limit and the increase of the expected significance with increasing integrated luminosity. It can be noted that a 3σ expected significance is achieved at $\mathcal{L} \sim 400\text{fb}^{-1}$, indicating evidence for observation of tWZ . The 5σ significance 'discovery' standard is above our 1000fb^{-1} luminosity range of study. Furthermore, these plots show that the sensitivity of tWZ is hindered by the low amount of events we observe, rather than the systematic effects. This is evident since increasing the luminosity, therefore increasing the number of events we see in the detector, directly causes a steady increase in sensitivity.

Chapter 5

Conclusion and Outlook

Appendix A

Appendix

A.1 Pre-Fit Plots

A.1.1 tWZ OF SR

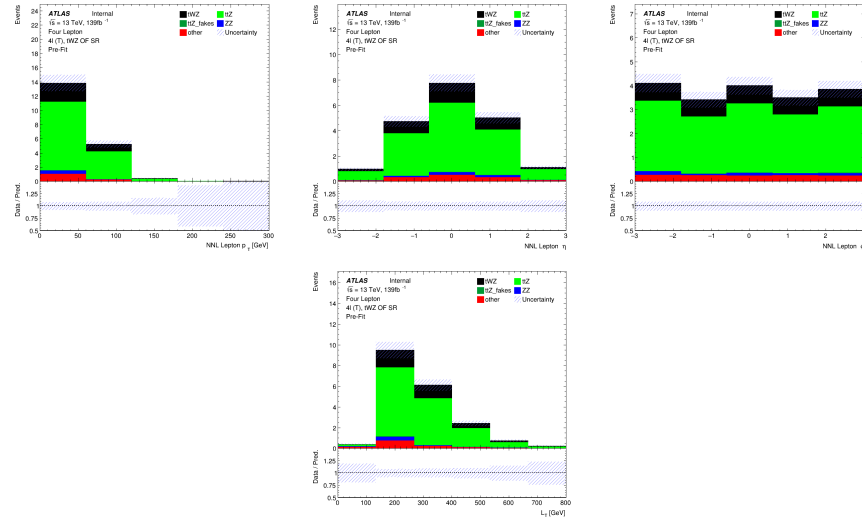


Figure A.1: Top row: MC predictions for p_T , η and ϕ for next-to-next-to-leading (NNL) leptons in the tWZ OF SR region (*blinded*). Bottom row: MC predictions for L_T (scalar sum of lepton p_T) in the tWZ OF SR region (*blinded*)

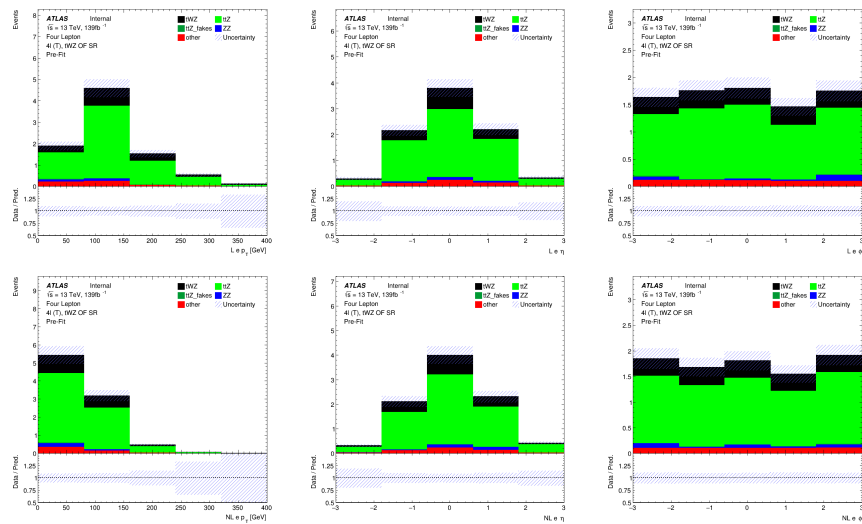


Figure A.2: MC predictions for p_T , η and ϕ for leading (L) electrons (top row) and next-to-leading (NL) electrons (bottom row) in the tWZ OF SR region (*blinded*)

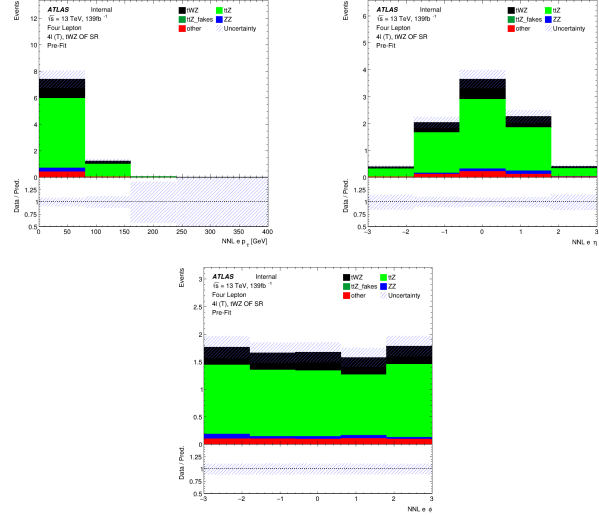


Figure A.3: MC predictions for p_T , η (top row) and ϕ (bottom row) for next-to-next-to-leading (NNL) electrons in the tWZ OF SR region

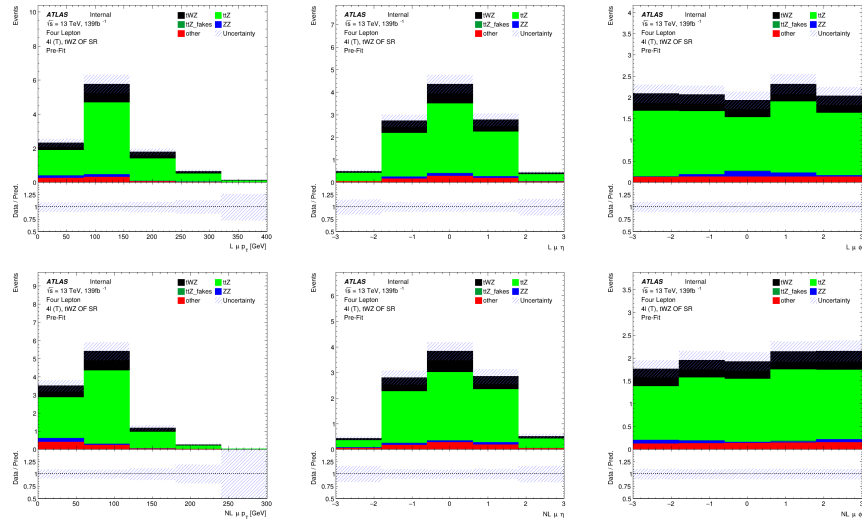


Figure A.4: MC predictions for p_T , η and ϕ for leading (L) muons (top row) and next-to-leading (NL) muons (bottom row) in the tWZ OF SR region (*blinded*)

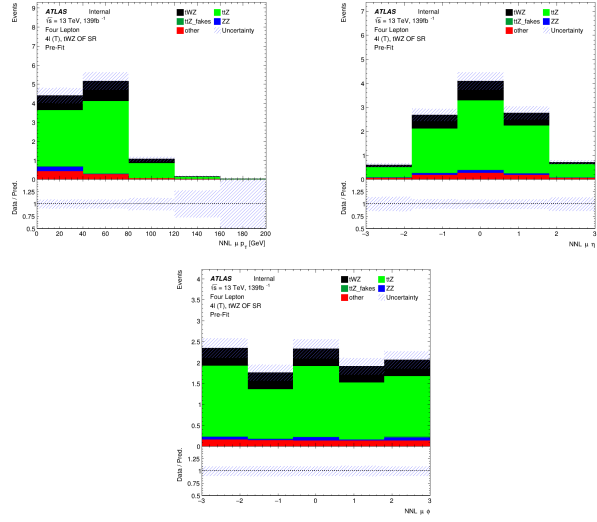


Figure A.5: MC predictions for p_T , η (top row) and ϕ (bottom row) for next-to-next-to-leading (NNL) muons in the tWZ OF SR region (*blinded*)

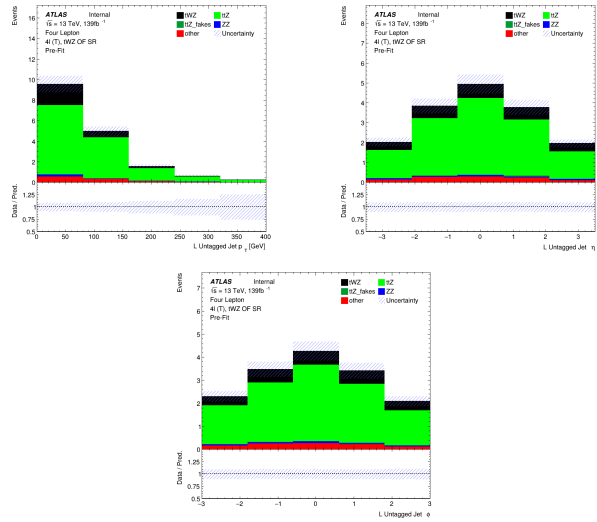


Figure A.6: MC predictions for p_T , η (top row) and ϕ (bottom row) for untagged jets in the tWZ OF SR region (*blinded*)

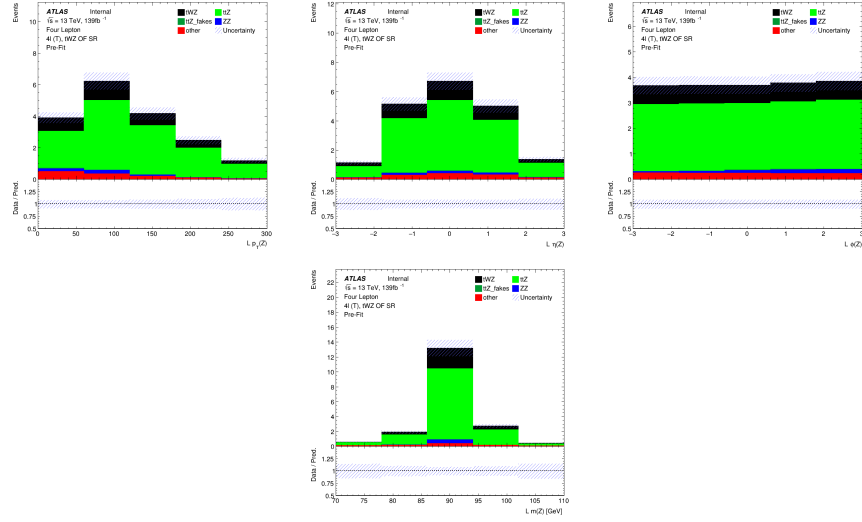


Figure A.7: MC predictions for p_T , η , ϕ (top row) and mass (m_Z) (bottom row) of the leading reconstructed Z candidate (OSSF lepton pair with $|m_{\text{OSSF}} - m(Z)| < 30 \text{ GeV}$) in the tWZ OF SR region (*blinded*)

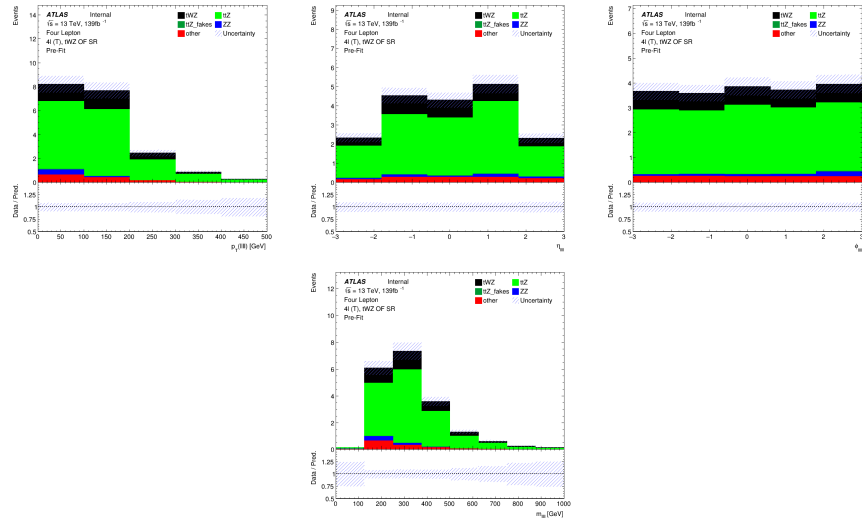


Figure A.8: MC predictions for p_T , η , ϕ (top row) and mass (bottom row) of the lepton system ($\ell\ell\ell\ell$) in the tWZ OF SR region (*blinded*)

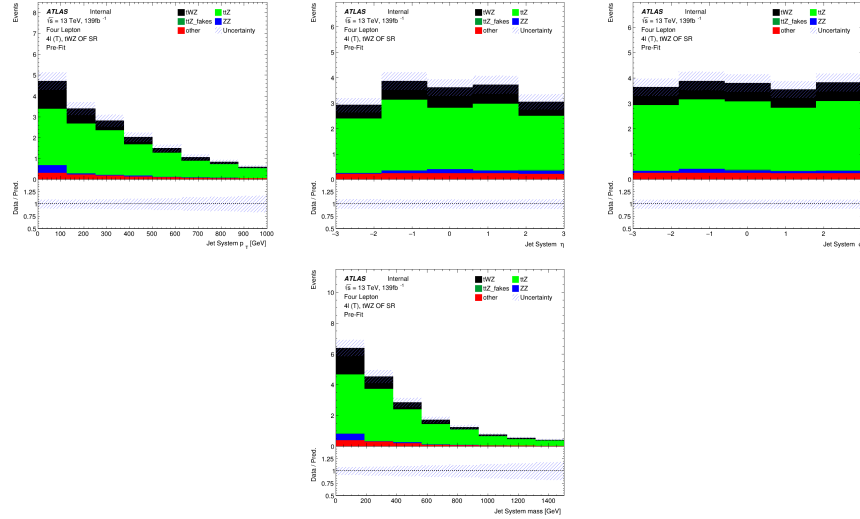


Figure A.9: MC predictions for p_T , η , ϕ (top row) and mass (bottom row) of the jet systems in the tWZ OF SR region (*blinded*)

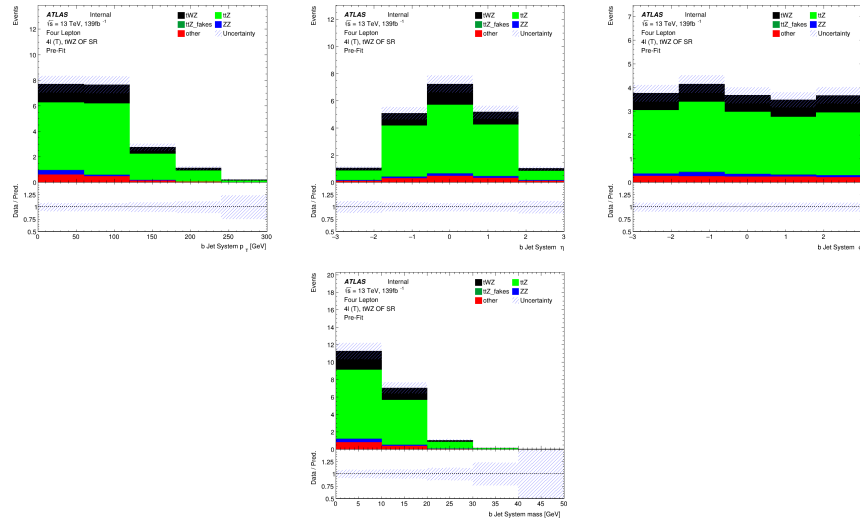


Figure A.10: MC predictions for p_T , η , ϕ (top row) and mass (bottom row) of the b-tagged jet systems in the tWZ OF SR region (*blinded*)

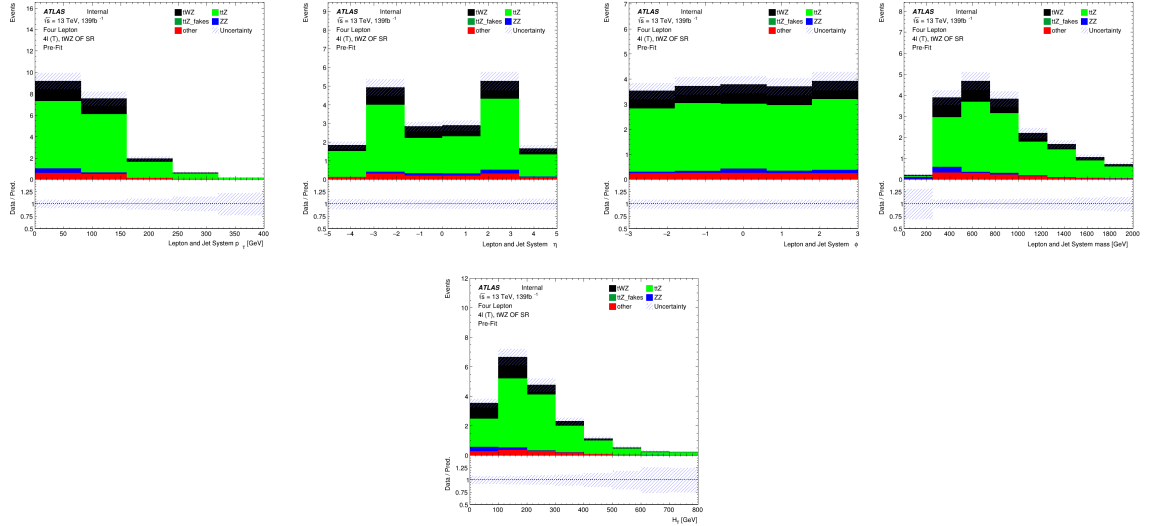


Figure A.11: MC predictions for p_T , η and ϕ (top row) and mass (bottom left) for the lepton + jet systems ($\ell\ell\ell\ell + \text{jets}$) in the tWZ OF SR region (*blinded*). Bottom right: MC predictions for H_T (scalar sum of jet p_T and lepton p_T) in the tWZ OF SR region (*blinded*)

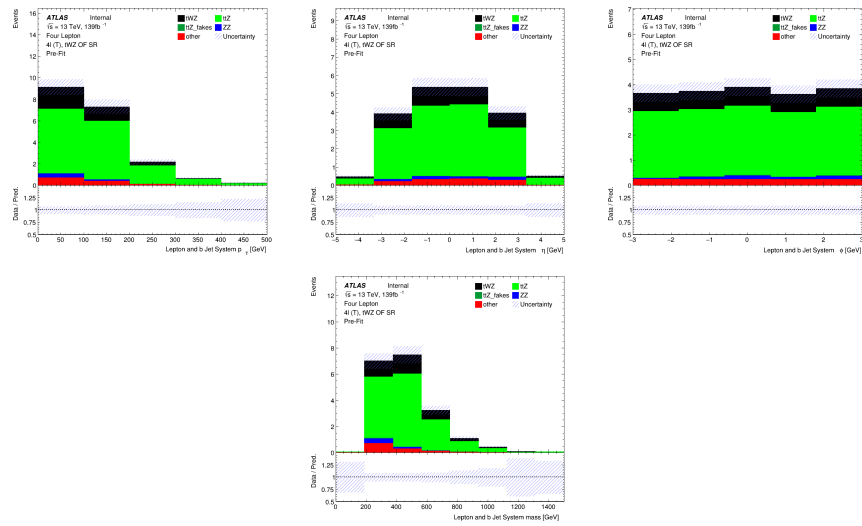


Figure A.12: MC predictions for p_T , η , ϕ (top row) and mass (bottom row) of the lepton + b-tagged jet systems ($\ell\ell\ell\ell + \text{b-tagged jets}$) in the tWZ OF SR region (*blinded*)

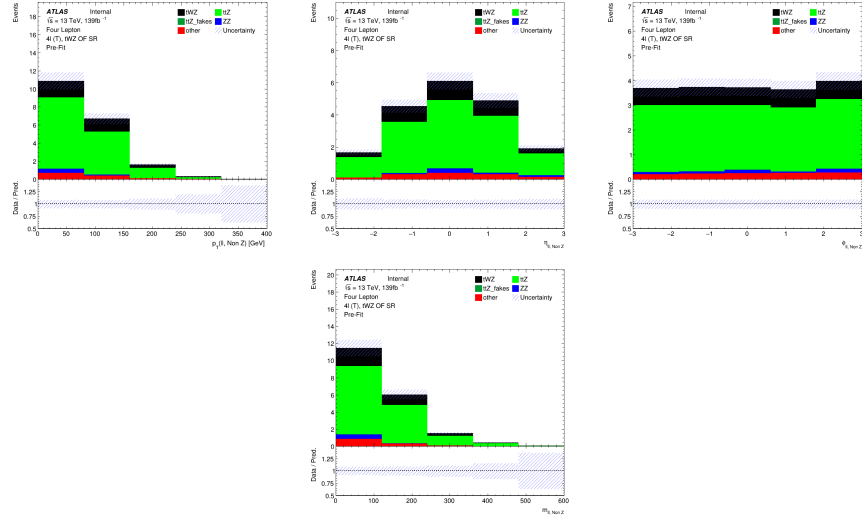


Figure A.13: MC predictions for p_T , η , ϕ (top row) and mass (bottom row) of reconstructed Non Z leptons (lepton pairs which don't originate from a Z candidate) in the tWZ OF SR region (*blinded*)

A.1.2 tWZ SF SR

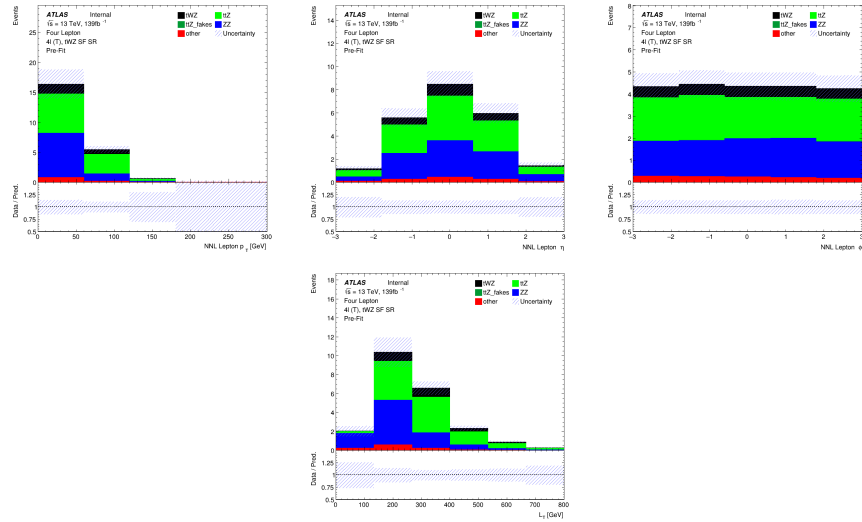


Figure A.14: Top row: MC predictions for p_T , η and ϕ for next-to-next-to-leading (NNL) leptons in the tWZ SF SR region (*blinded*). Bottom row: MC prediction for L_T (scalar sum of lepton p_T) in the tWZ SF SR region (*blinded*)

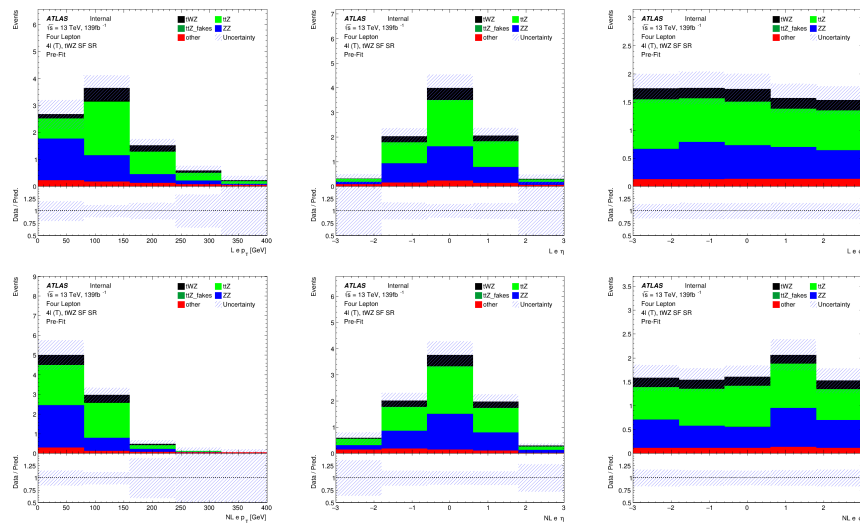


Figure A.15: MC predictions for p_T , η and ϕ for leading (L) electrons (top row) and next-to-leading (NL) electrons (bottom row) in the tWZ SF SR region (*blinded*)

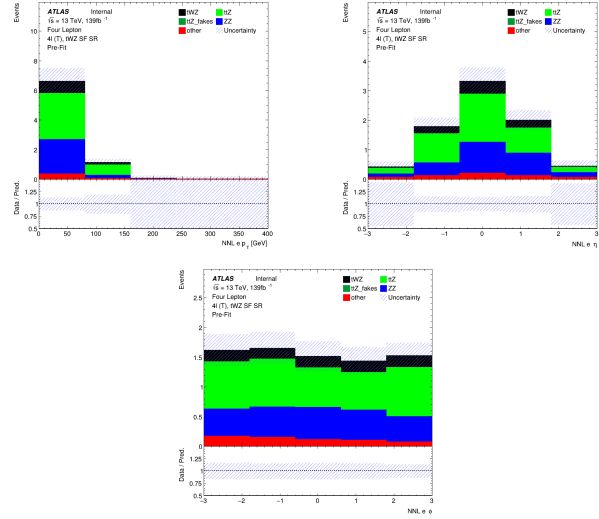


Figure A.16: MC predictions for p_T , η (top row) and ϕ (bottom row) for next-to-next-to-leading (NNL) electrons in the tWZ SF SR region

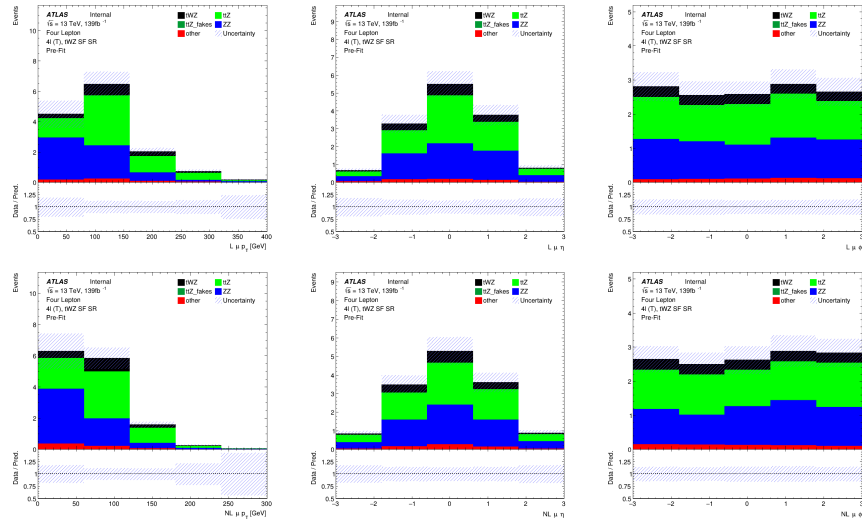


Figure A.17: MC predictions for p_T , η and ϕ for leading (L) muons (top row) and next-to-leading (NL) muons (bottom row) in the tWZ SF SR region (*blinded*)

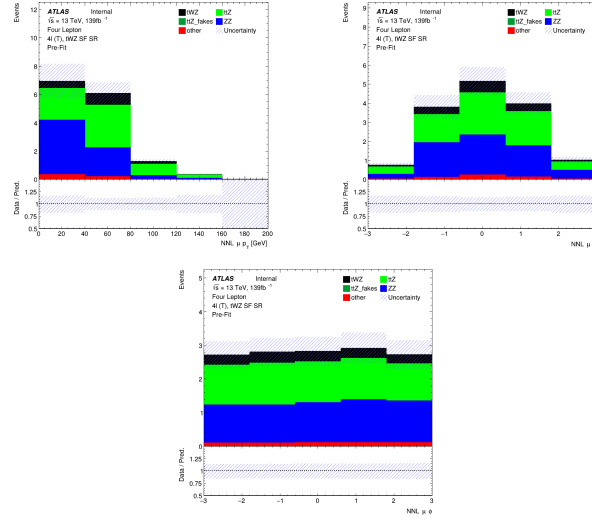


Figure A.18: MC predictions for p_T , η (top row) and ϕ (bottom row) for next-to-next-to-leading (NNL) muons in the tWZ SF SR region (*blinded*)

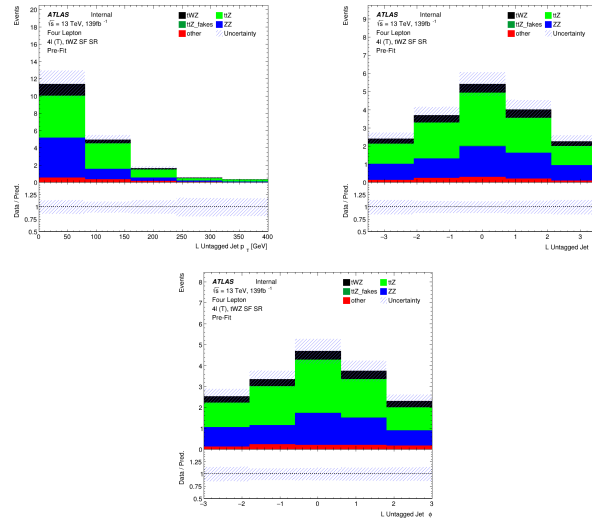


Figure A.19: MC predictions for p_T , η (top row) and ϕ (bottom row) for untagged jets in the tWZ SF SR region (*blinded*)

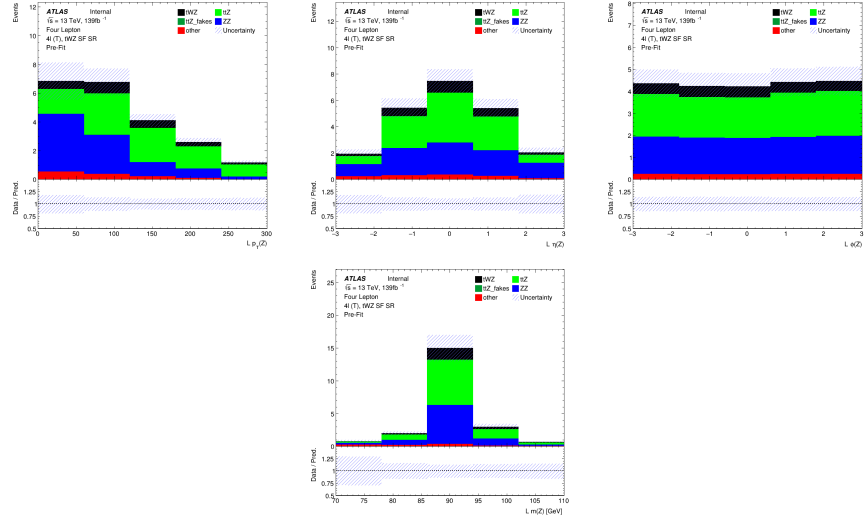


Figure A.20: MC predictions for p_T , η , ϕ (top row) and mass (m_Z) (bottom row) of the leading reconstructed Z candidate (OSSF lepton pair with $|m_{\text{OSSF}} - m(Z)| < 30 \text{ GeV}$) in the tWZ SF SR region (*blinded*)

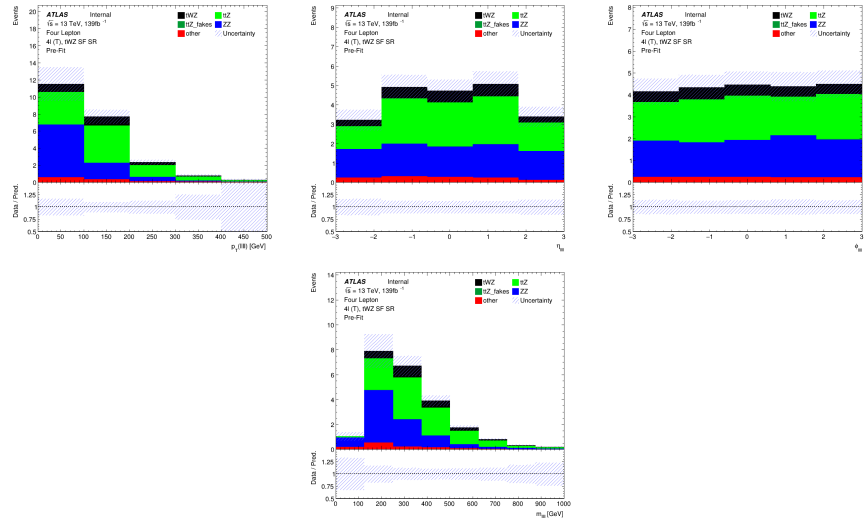


Figure A.21: MC predictions for p_T , η , ϕ (top row) and mass (bottom row) of the lepton system ($\ell\ell\ell\ell$) in the tWZ SF SR region (*blinded*)

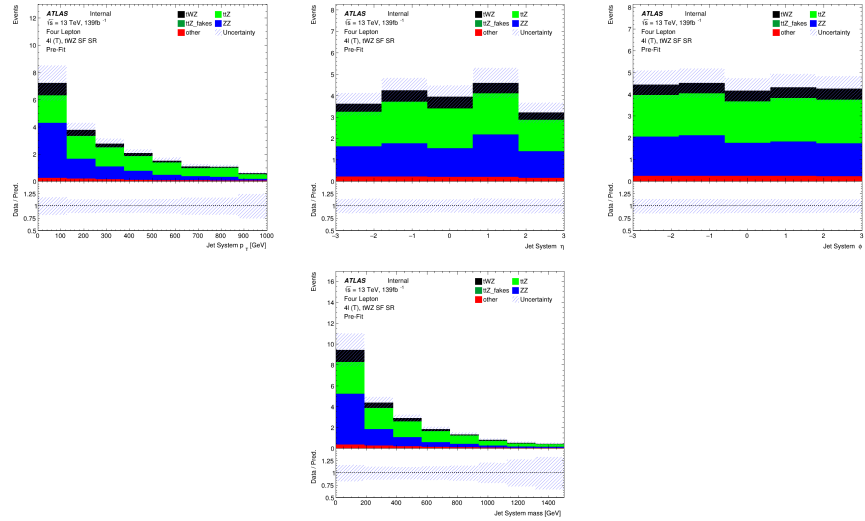


Figure A.22: MC predictions for p_T , η , ϕ (top row) and mass (bottom row) of the jet systems in the tWZ SF SR region (*blinded*)

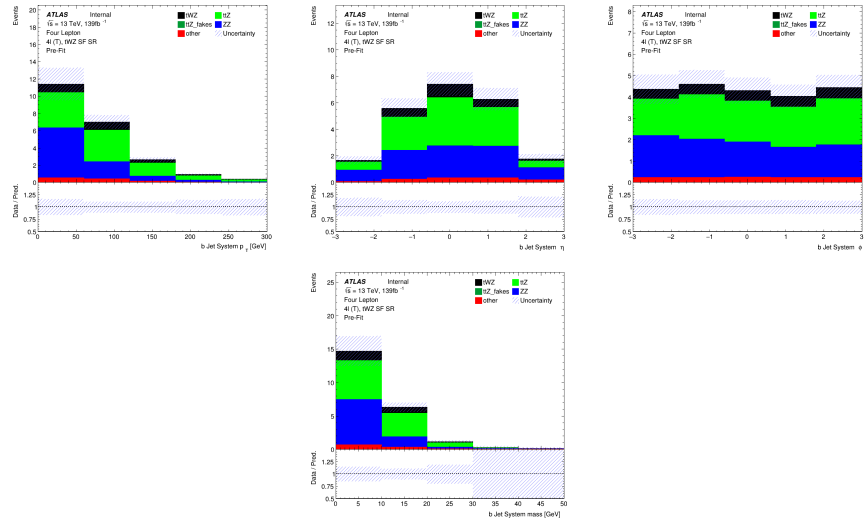


Figure A.23: MC predictions for p_T , η , ϕ (top row) and mass (bottom row) of the b-tagged jet systems in the tWZ SF SR region (*blinded*)

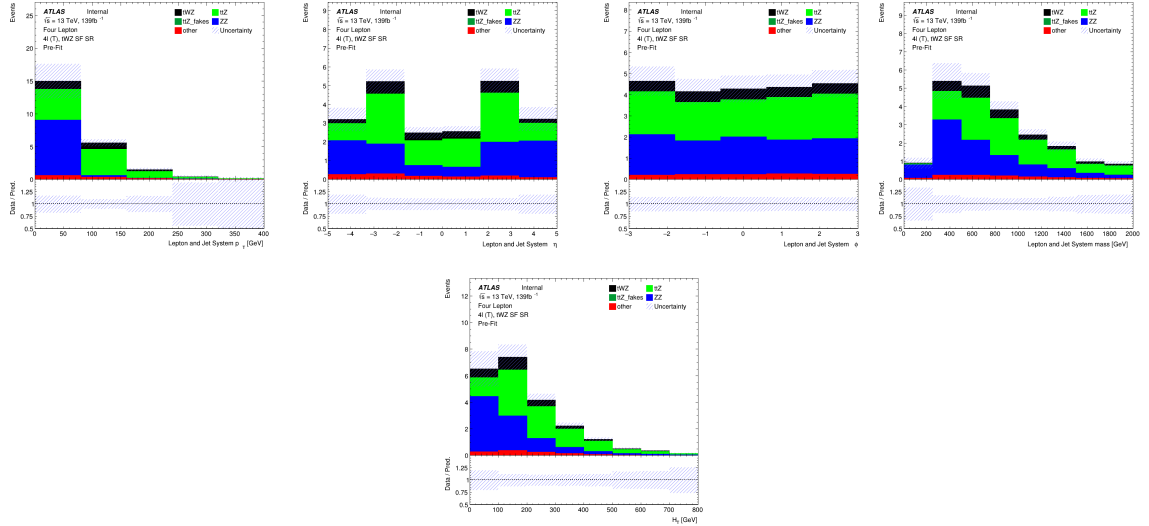


Figure A.24: MC predictions for p_T , η and ϕ (top row) and mass (bottom left) for the lepton + jet systems ($\ell\ell\ell\ell$ + jets) in the tWZ SF SR region (*blinded*). Bottom right: MC predictions for H_T (scalar sum of jet p_T and lepton p_T) in the tWZ SF SR region (*blinded*)

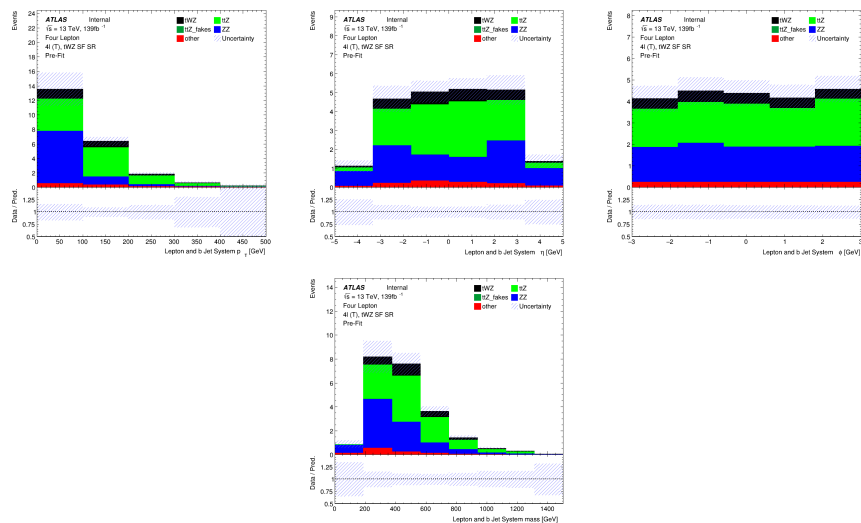


Figure A.25: MC predictions for p_T , η , ϕ (top row) and mass (bottom row) of the lepton + b-tagged jet systems ($\ell\ell\ell\ell$ + b-tagged jets) in the tWZ SF SR region (*blinded*)

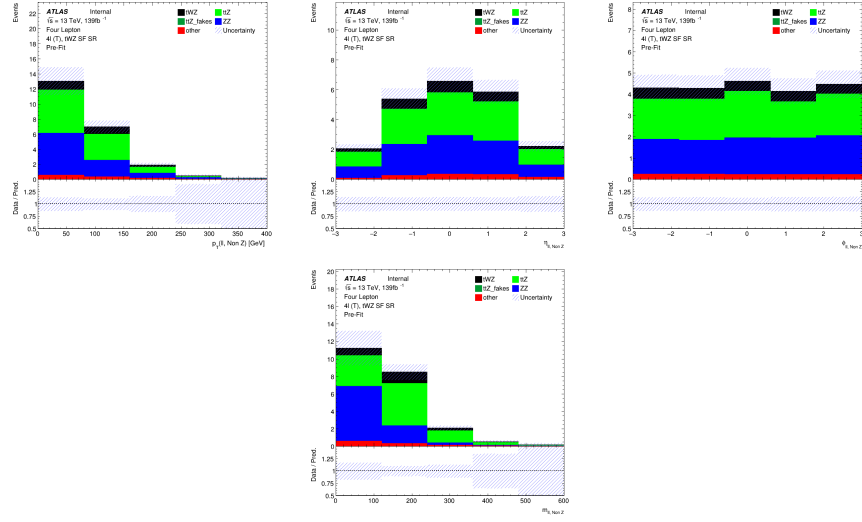


Figure A.26: MC predictions for p_T , η , ϕ (top row) and mass (bottom row) of reconstructed Non Z leptons (lepton pairs which don't originate from a Z candidate) in the tWZ SF SR region (*blinded*)

A.1.3 $t\bar{t}Z$ CR

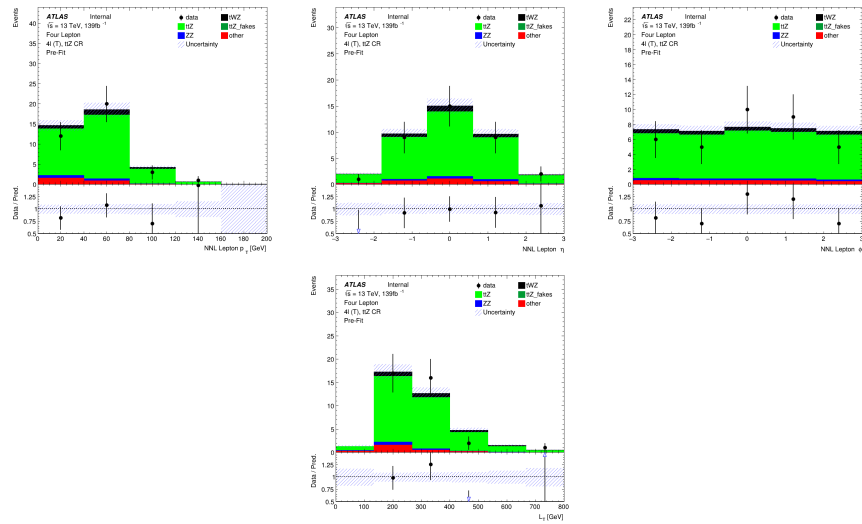


Figure A.27: Top row: MC predictions for p_T , η and ϕ for next-to-next-to-leading (NNL) leptons in the $t\bar{t}Z$ CR region . Bottom row: MC predictions for L_T (scalar sum of lepton p_T) in the $t\bar{t}Z$ CR region

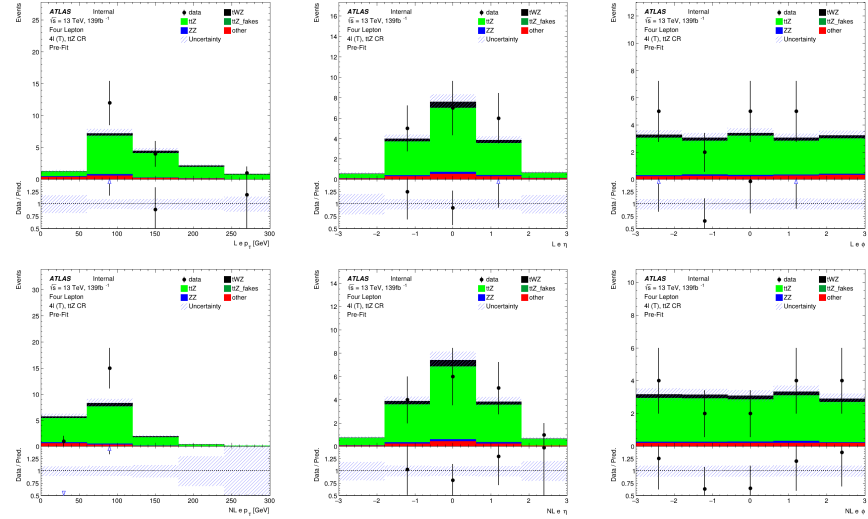


Figure A.28: MC predictions for p_T , η and ϕ for leading (L) electrons (top row) and next-to-leading (NL) electrons (bottom row) in the $t\bar{t}Z$ CR region

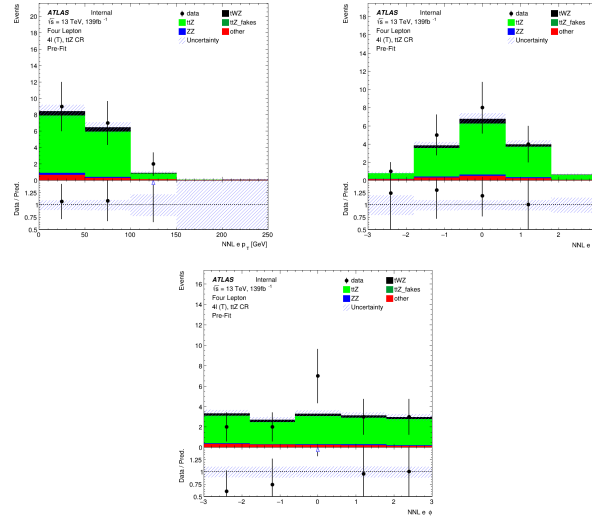


Figure A.29: MC predictions for p_T , η (top row) and ϕ (bottom row) for next-to-next-to-leading (NNL) electrons in the $t\bar{t}Z$ CR region

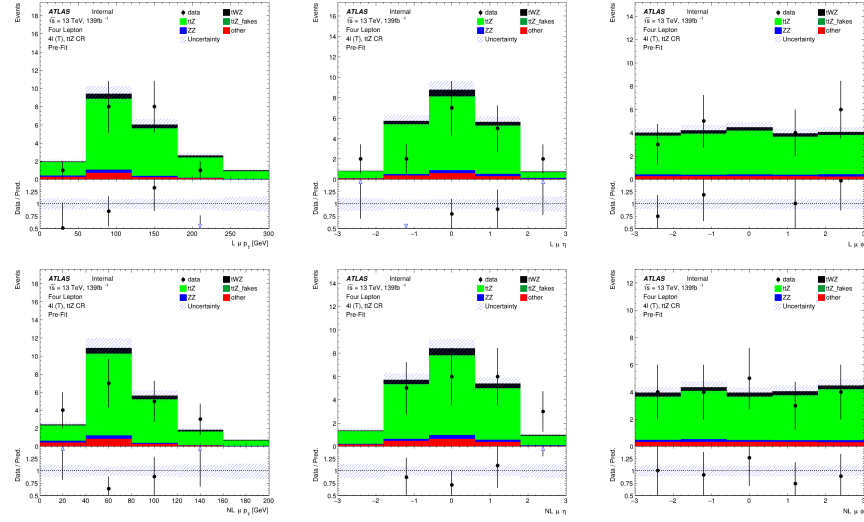


Figure A.30: MC predictions for p_T , η and ϕ for leading (L) muons (top row) and next-to-leading (NL) muons (bottom row) in the $t\bar{t}Z$ CR region

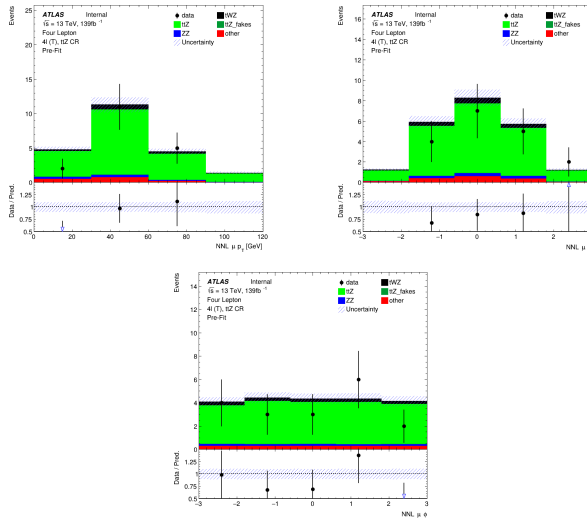


Figure A.31: MC predictions for p_T , η (top row) and ϕ (bottom row) for next-to-next-to-leading (NNL) muons in the $t\bar{t}Z$ CR region

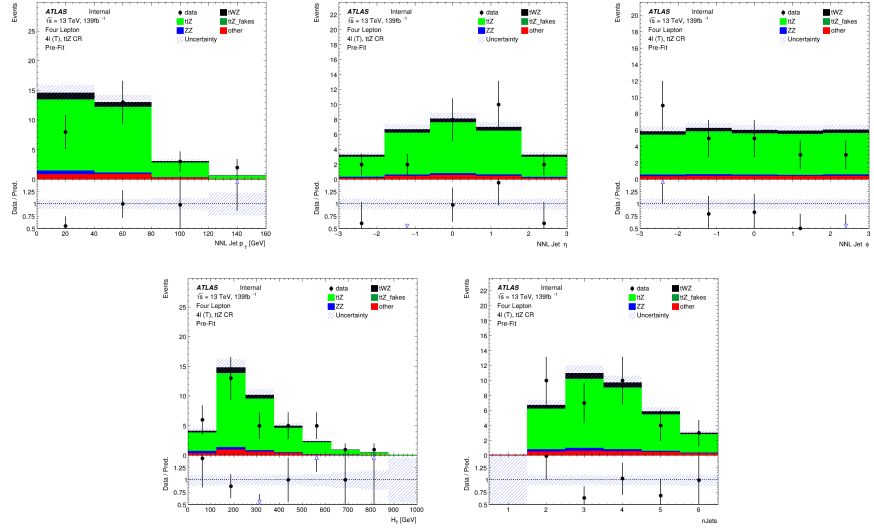


Figure A.32: Top row: MC predictions for p_T , η and ϕ for next-to-next-to-leading (NNL) jets in the $t\bar{t}Z$ CR region . . Bottom row: MC predictions for H_T (scalar sum of Jet p_T) (left) and the Number of jets (right) in the $t\bar{t}Z$ CR region

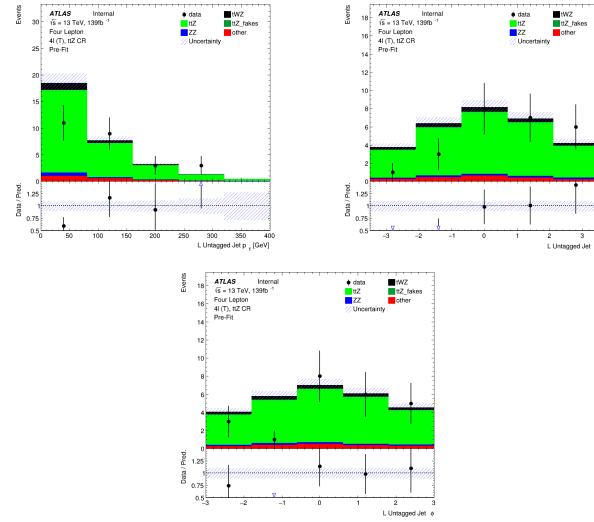


Figure A.33: MC predictions for p_T , η (top row) and ϕ (bottom row) for untagged jets in the $t\bar{t}Z$ CR region

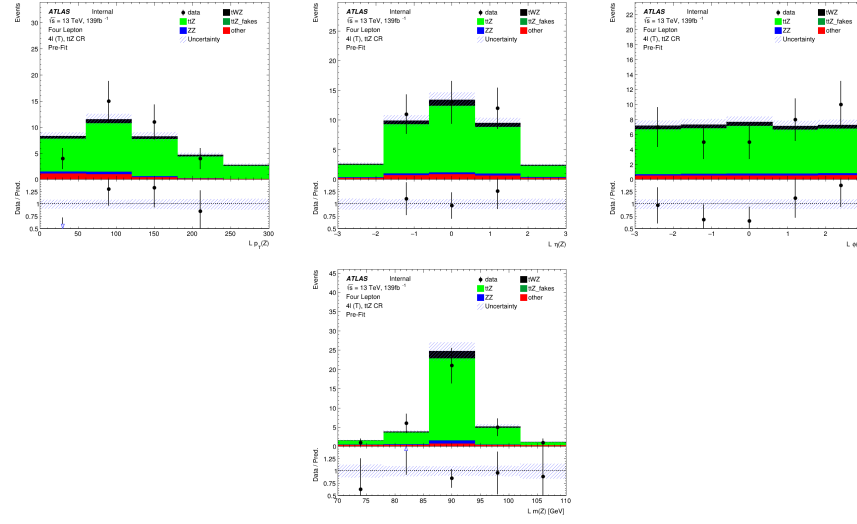


Figure A.34: MC predictions for p_T , η , ϕ (top row) and mass (m_Z) (bottom row) of reconstructed leading Z candidates (OSSF lepton pair with $|m_{\text{OSSF}} - m(Z)| < 30 \text{ GeV}$) in the $t\bar{t}Z$ CR region

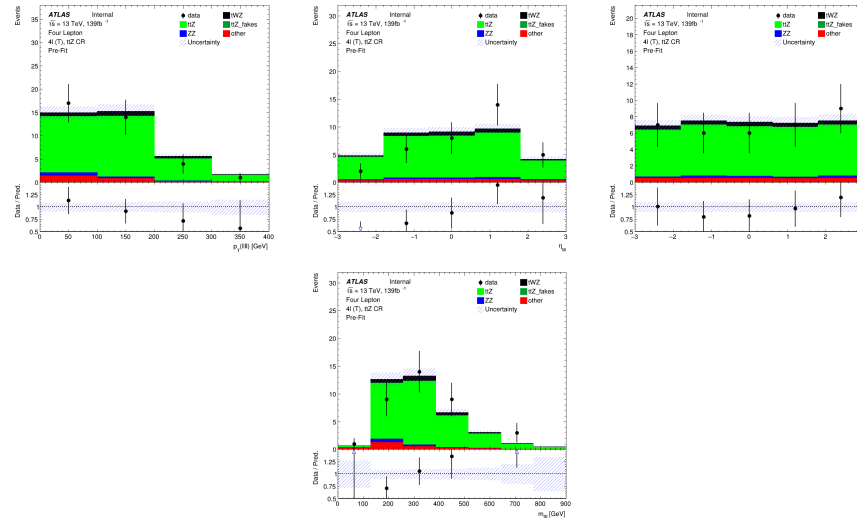


Figure A.35: MC predictions for p_T , η , ϕ (top row) and mass (bottom row) of the lepton system ($\ell\ell\ell\ell$) in the $t\bar{t}Z$ CR region

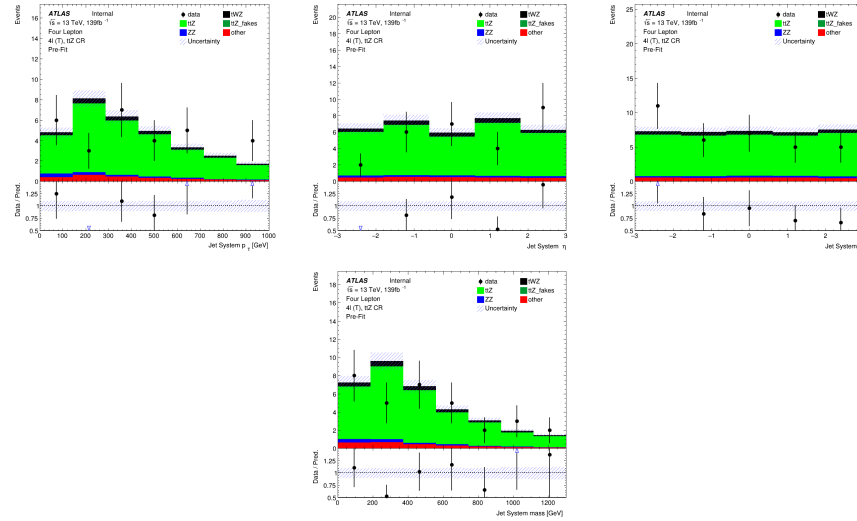


Figure A.36: MC predictions for p_T , η , ϕ (top row) and mass (bottom row) of the jet systems in the $t\bar{t}Z$ CR region

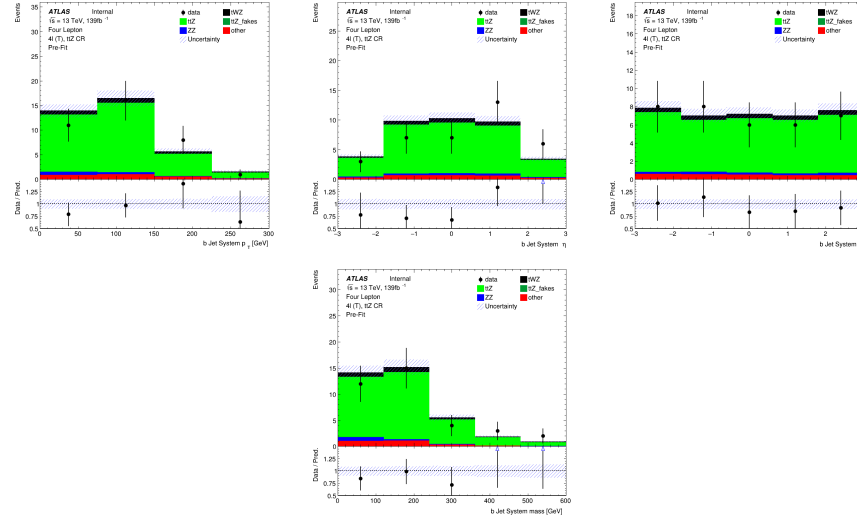


Figure A.37: MC predictions for p_T , η , ϕ (top row) and mass (bottom row) of the b-tagged jet systems in the $t\bar{t}Z$ CR region

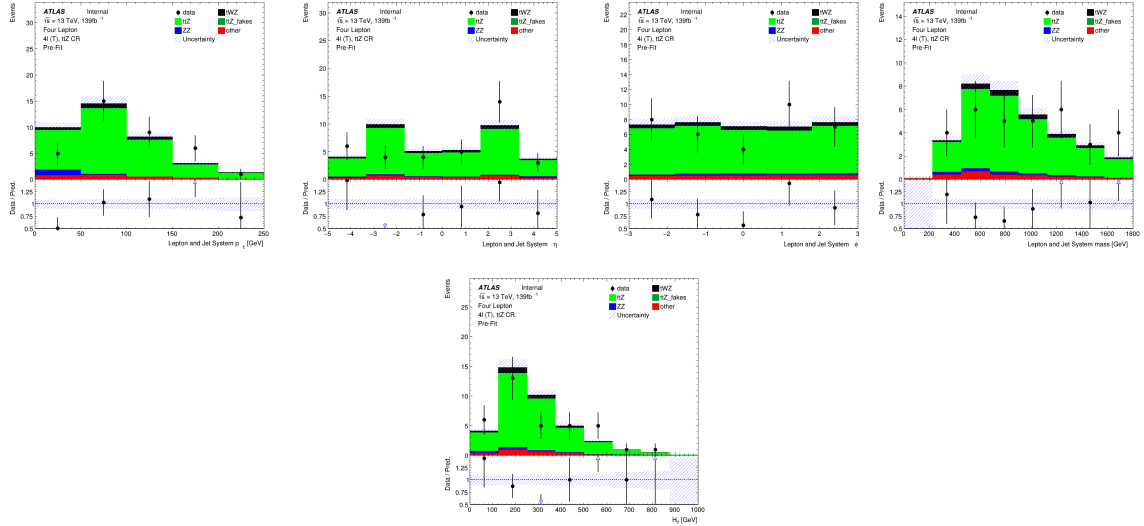


Figure A.38: MC predictions for p_T , η and ϕ (top row) and mass (bottom left) for the lepton + jet systems ($\ell\ell\ell\ell$ + jets) in the $t\bar{t}Z$ CR region . Bottom right: MC predictions for H_T (scalar sum of jet p_T and lepton p_T) in the $t\bar{t}Z$ CR region

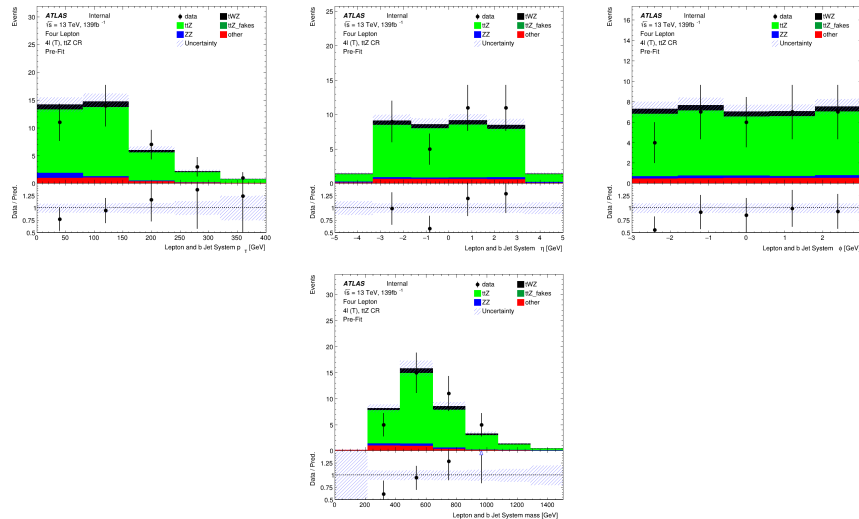


Figure A.39: MC predictions for p_T , η , ϕ (top row) and mass (bottom row) of the lepton + b-tagged jet systems ($\ell\ell\ell\ell$ + b-tagged jets) in the $t\bar{t}Z$ CR region

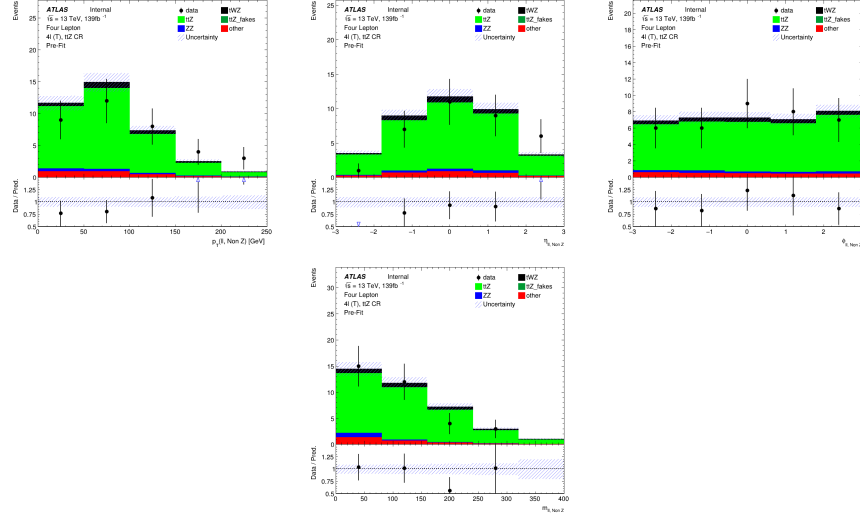


Figure A.40: MC predictions for p_T , η , ϕ (top row) and mass (bottom row) of reconstructed Non Z leptons (lepton pairs which don't originate from a Z candidate) in the $t\bar{t}Z$ CR region

A.1.4 ZZb CR

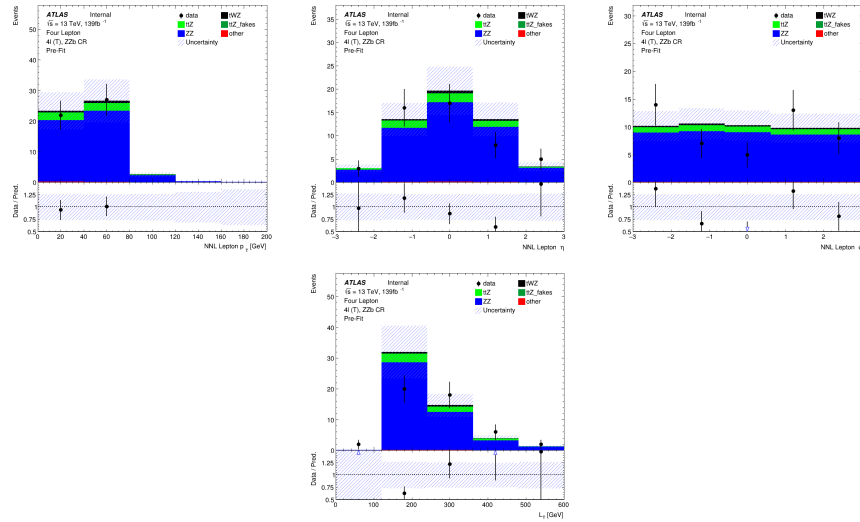


Figure A.41: Top row: MC predictions for p_T , η and ϕ for next-to-next-to-leading (NNL) leptons in the ZZb CR region . Bottom row: MC predictions for L_T (scalar sum of lepton p_T) in the ZZb CR region

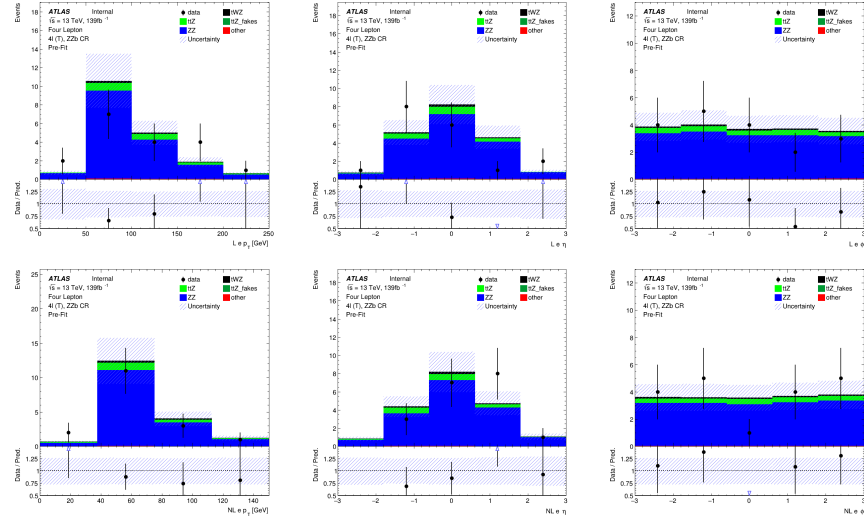


Figure A.42: MC predictions for p_T , η and ϕ for leading (L) electrons (top row) and next-to-leading (NL) electrons (bottom row) in the ZZb CR region

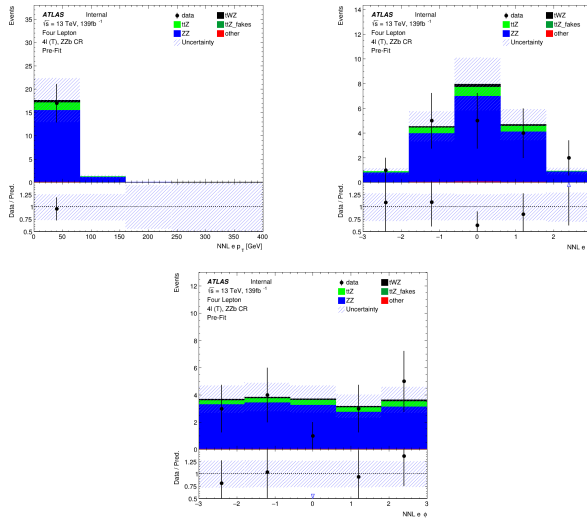


Figure A.43: MC predictions for p_T , η (top row) and ϕ (bottom row) for next-to-next-to-leading (NNL) electrons in the ZZb CR region

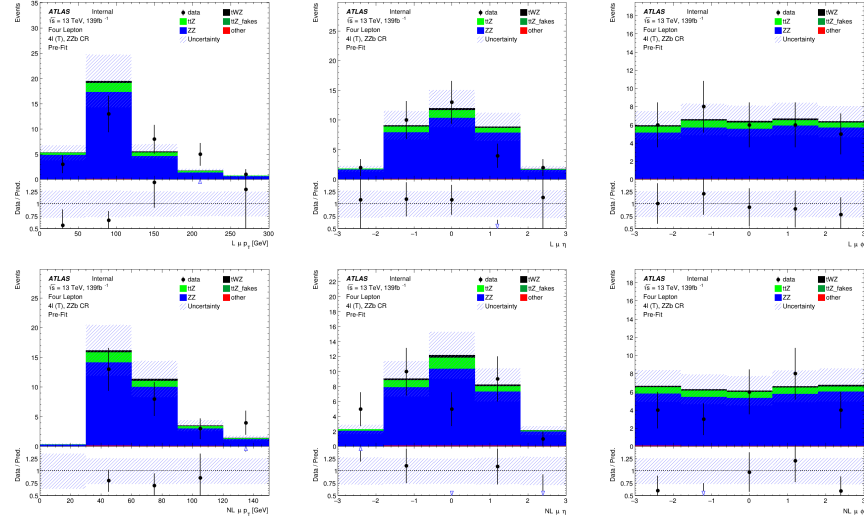


Figure A.44: MC predictions for p_T , η and ϕ for leading (L) muons (top row) and next-to-leading (NL) muons (bottom row) in the ZZb CR region

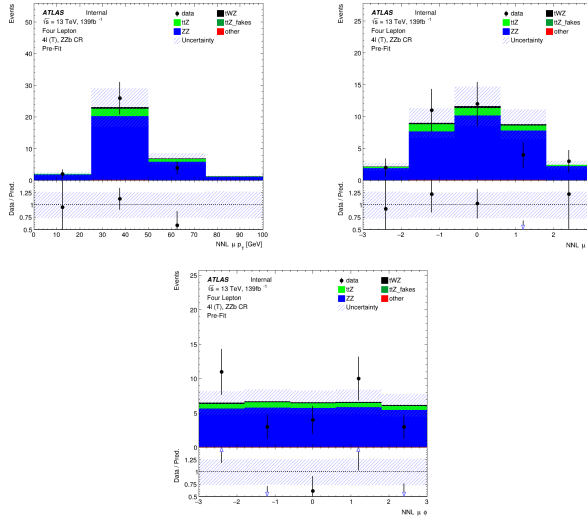


Figure A.45: MC predictions for p_T , η (top row) and ϕ (bottom row) for next-to-next-to-leading (NNL) muons in the ZZb CR region

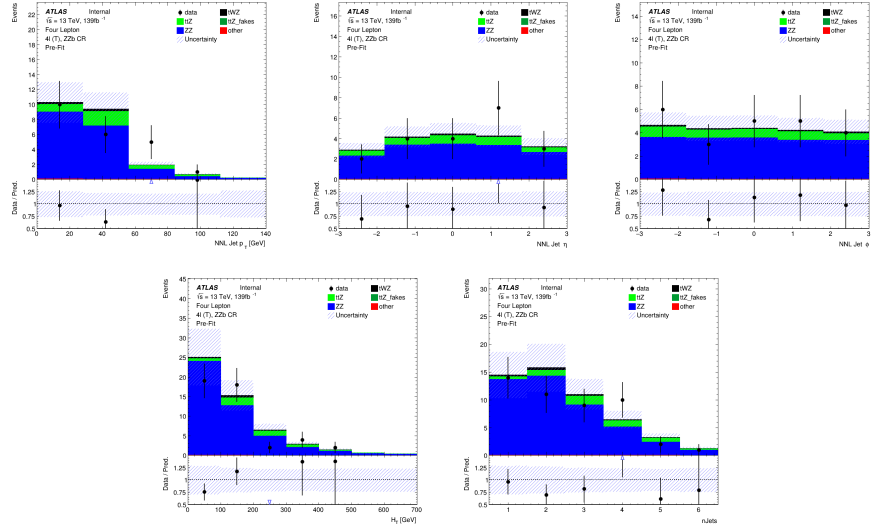


Figure A.46: Top row: MC predictions for p_T , η and ϕ for next-to-next-to-leading (NNL) jets in the ZZb CR region . . Bottom row: MC predictions for H_T (scalar sum of Jet p_T) (left) and the Number of jets (right) in the ZZb CR region

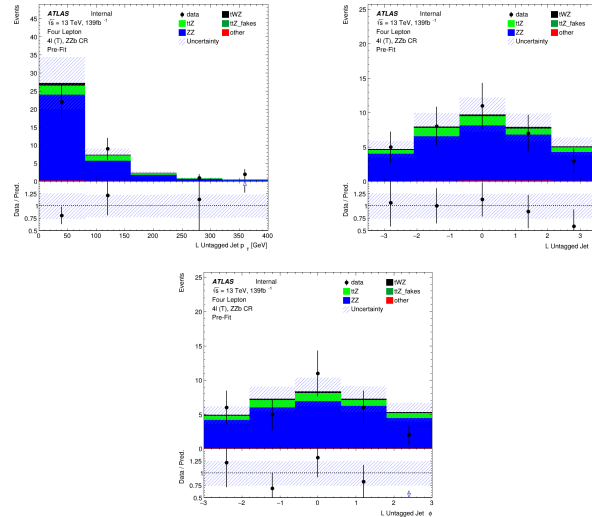


Figure A.47: MC predictions for p_T , η (top row) and ϕ (bottom row) for untagged jets in the ZZb CR region

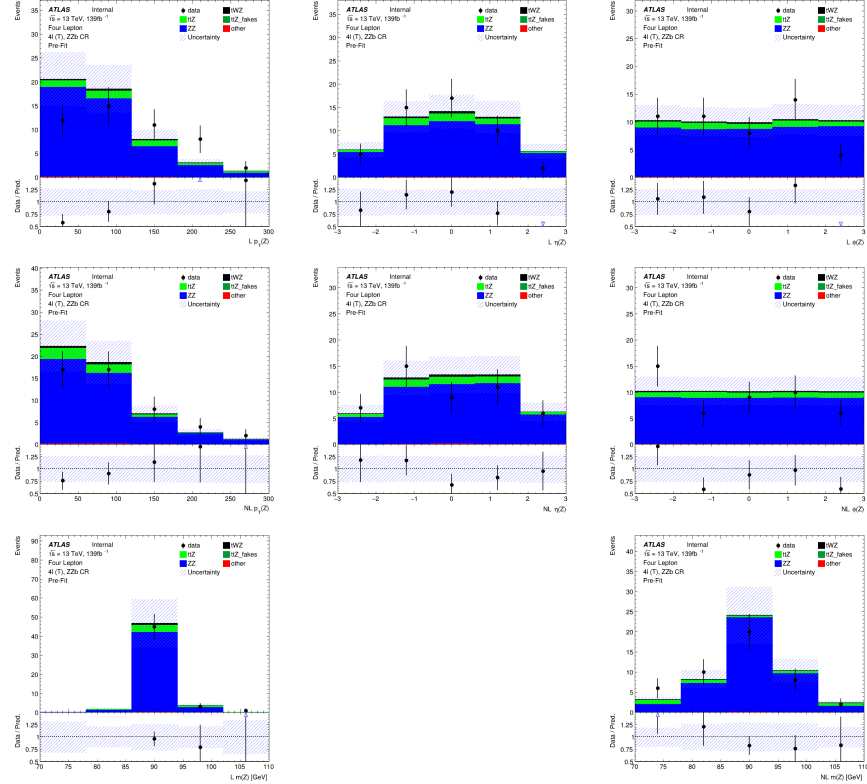


Figure A.48: MC predictions for p_T , η , ϕ of the leading (top row), next-to-leading (middle row) and mass (m_Z) (bottom row) of reconstructed Z candidates (OSSF lepton pair with $|m_{\text{OSSF}} - m(Z)| < 30 \text{ GeV}$) in the ZZb CR region

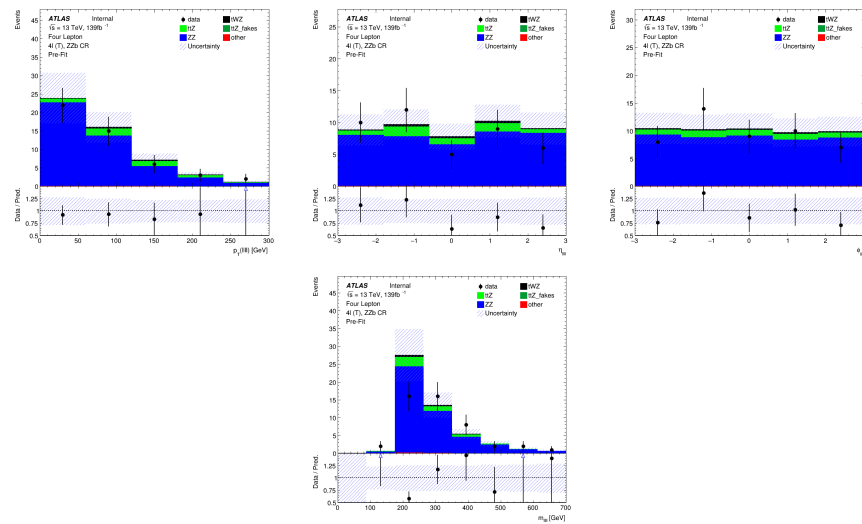


Figure A.49: MC predictions for p_T , η , ϕ (top row) and mass (bottom row) of the lepton system ($\ell\ell\ell\ell$) in the ZZ CR region

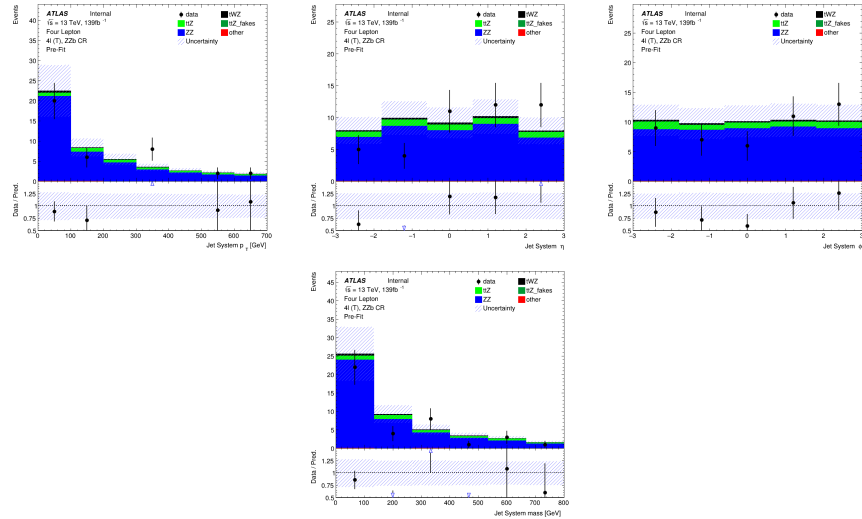


Figure A.50: MC predictions for p_T , η , ϕ (top row) and mass (bottom row) of the jet systems in the ZZb CR region

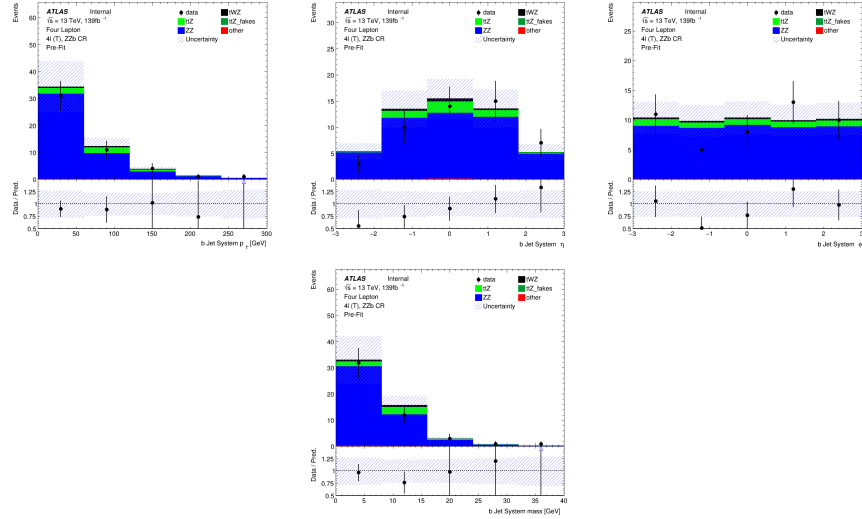


Figure A.51: MC predictions for p_T , η , ϕ (top row) and mass (bottom row) of the b-tagged jet systems in the ZZb CR region

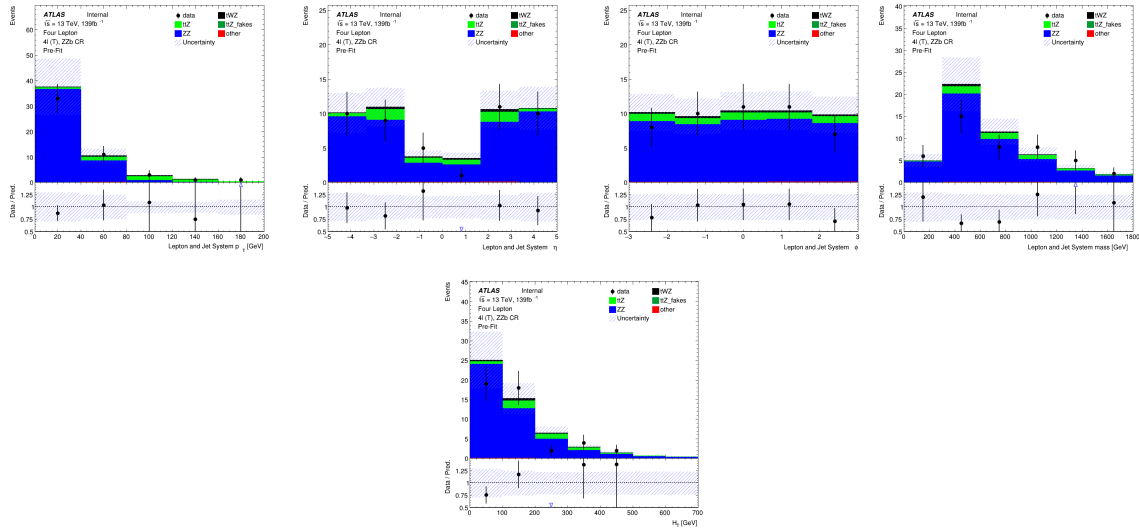


Figure A.52: MC predictions for p_T , η and ϕ (top row) and mass (bottom left) for the lepton + jet systems ($\ell\ell\ell\ell + \text{jets}$) in the ZZb CR region . Bottom right: MC predictions for H_T (scalar sum of jet p_T and lepton p_T) in the ZZb CR region

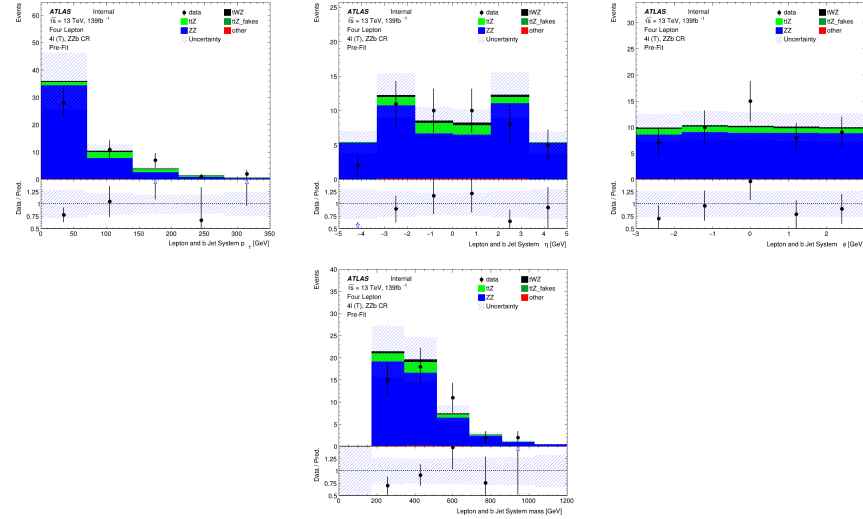


Figure A.53: MC predictions for p_T , η , ϕ (top row) and mass (bottom row) of the lepton + b-tagged jet systems ($\ell\ell\ell\ell + \text{b-tagged jets}$) in the ZZb CR region

A.1.5 $(tWZ)_\text{fake}$ CR

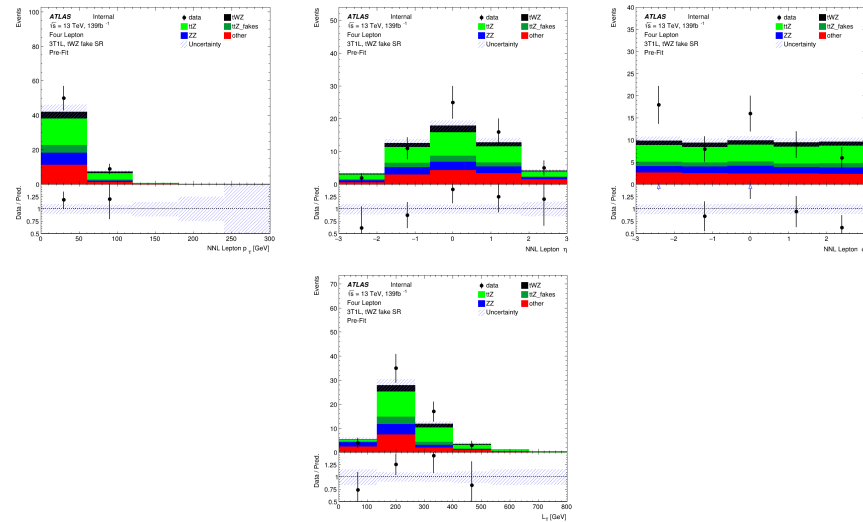


Figure A.54: Top row: MC predictions for p_T , η and ϕ for next-to-next-to-leading (NNL) leptons in the $(tWZ)_\text{fake}$ CR region . Bottom row: MC predictions for L_T (scalar sum of lepton p_T) in the $(tWZ)_\text{fake}$ CR region

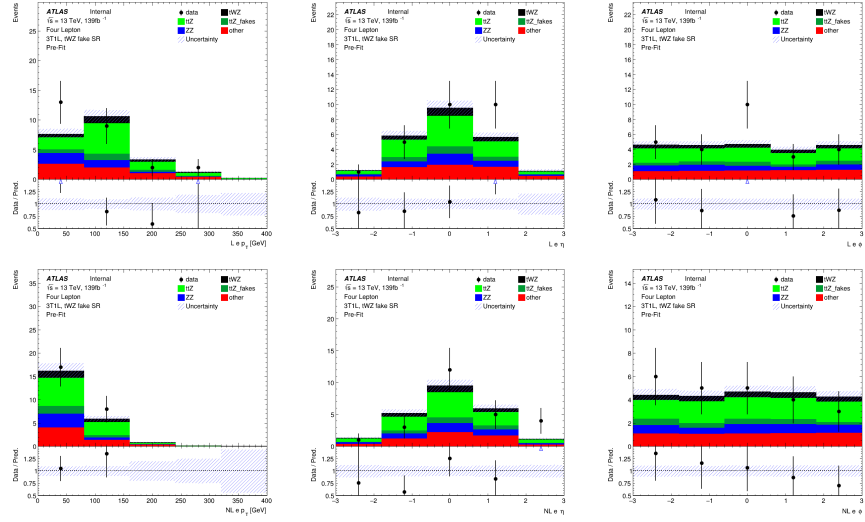


Figure A.55: MC predictions for p_T , η and ϕ for leading (L) electrons (top row) and next-to-leading (NL) electrons (bottom row) in the $(tWZ)_{\text{fake}}$ CR region

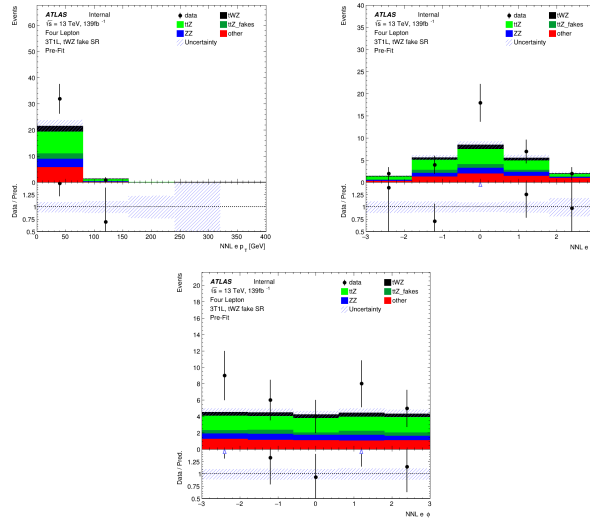


Figure A.56: MC predictions for p_T , η (top row) and ϕ (bottom row) for next-to-next-to-leading (NNL) electrons in the $(tWZ)_{\text{fake}}$ CR region

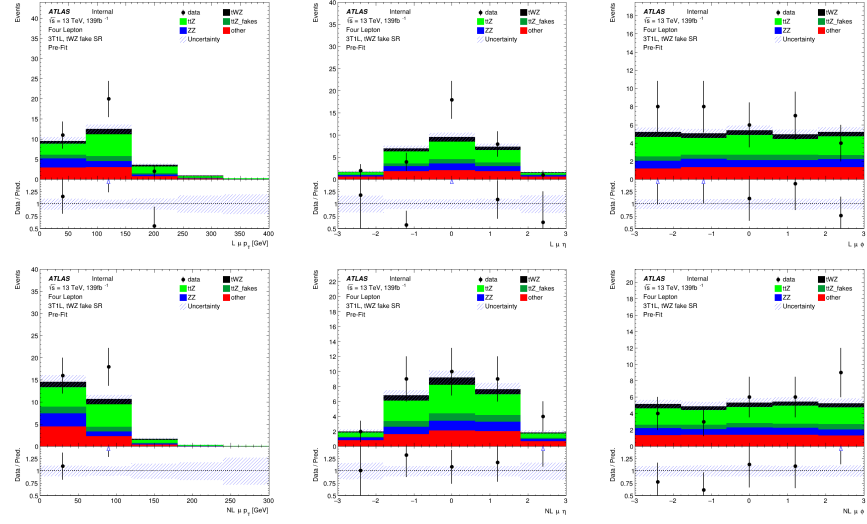


Figure A.57: MC predictions for p_T , η and ϕ for leading (L) muons (top row) and next-to-leading (NL) muons (bottom row) in the $(tWZ)_{\text{fake}}$ CR region

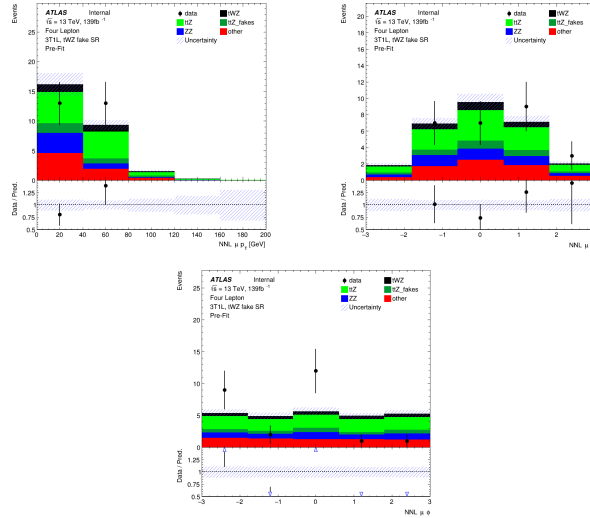


Figure A.58: MC predictions for p_T , η (top row) and ϕ (bottom row) for next-to-next-to-leading (NNL) muons in the $(tWZ)_{\text{fake}}$ CR region

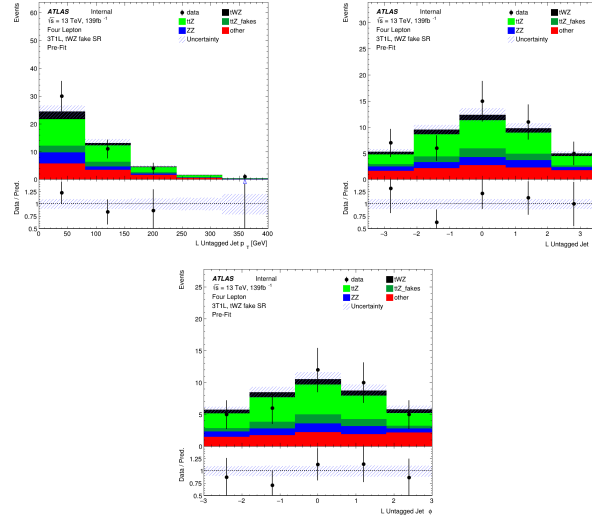


Figure A.59: MC predictions for p_T , η (top row) and ϕ (bottom row) for untagged jets in the $(tWZ)_{\text{fake}}$ CR region

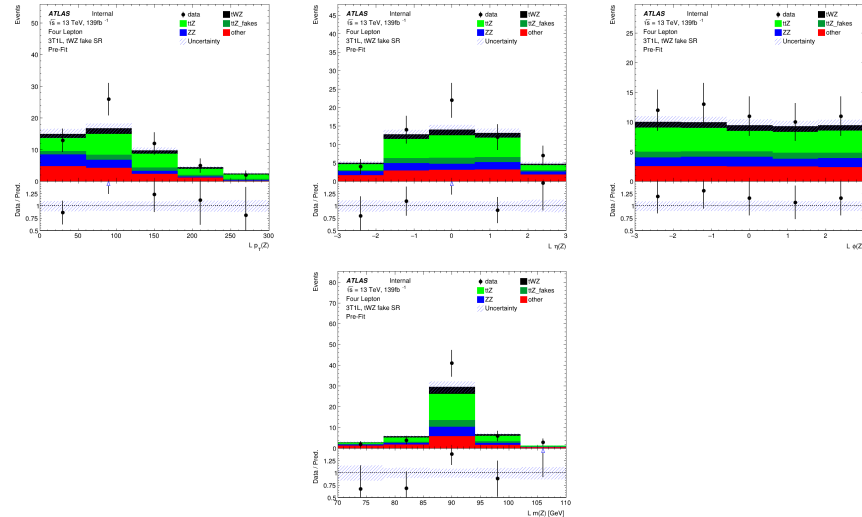


Figure A.60: MC predictions for p_T , η , ϕ (top row) and mass (m_Z) (bottom row) of the leading reconstructed Z candidate (OSSF lepton pair with $|m_{\text{OSSF}} - m(Z)| < 30 \text{ GeV}$) in the $(tWZ)_{\text{fake}}$ CR region

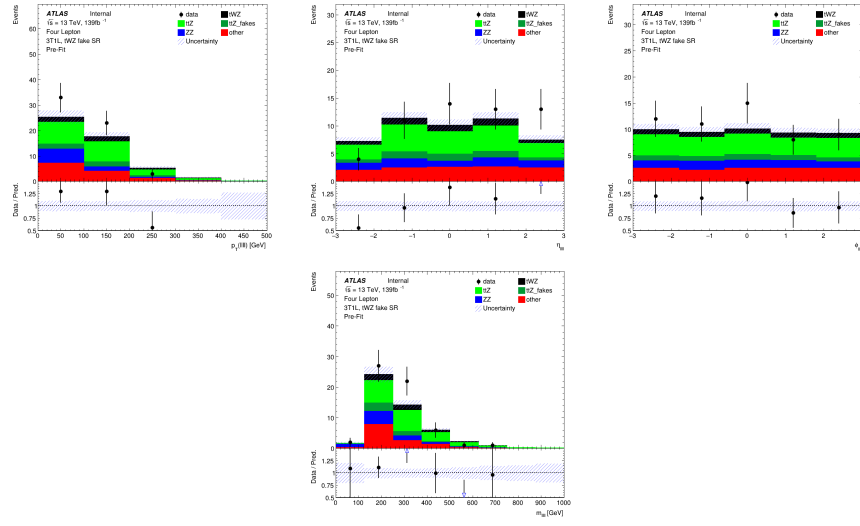


Figure A.61: MC predictions for p_T , η , ϕ (top row) and mass (bottom row) of the lepton system ($\ell\ell\ell\ell$) in the $(tWZ)_{\text{fake}}$ CR region

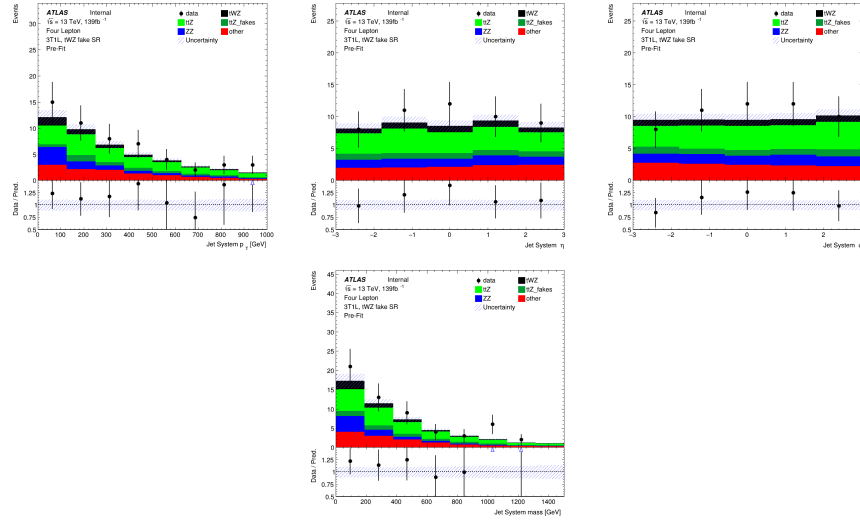


Figure A.62: MC predictions for p_T , η , ϕ (top row) and mass (bottom row) of the jet systems in the $(tWZ)_{\text{fake}}$ CR region

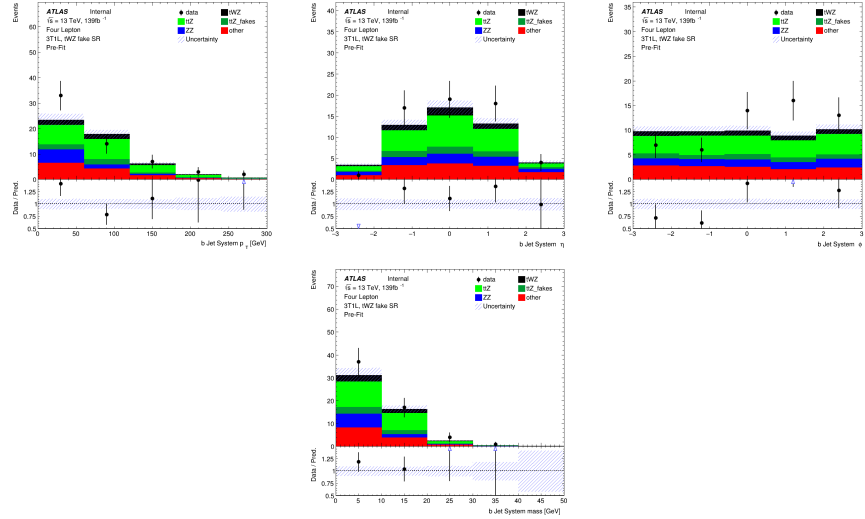


Figure A.63: MC predictions for p_T , η , ϕ (top row) and mass (bottom row) of the b-tagged jet systems in the $(tWZ)_{\text{fake}}$ CR region

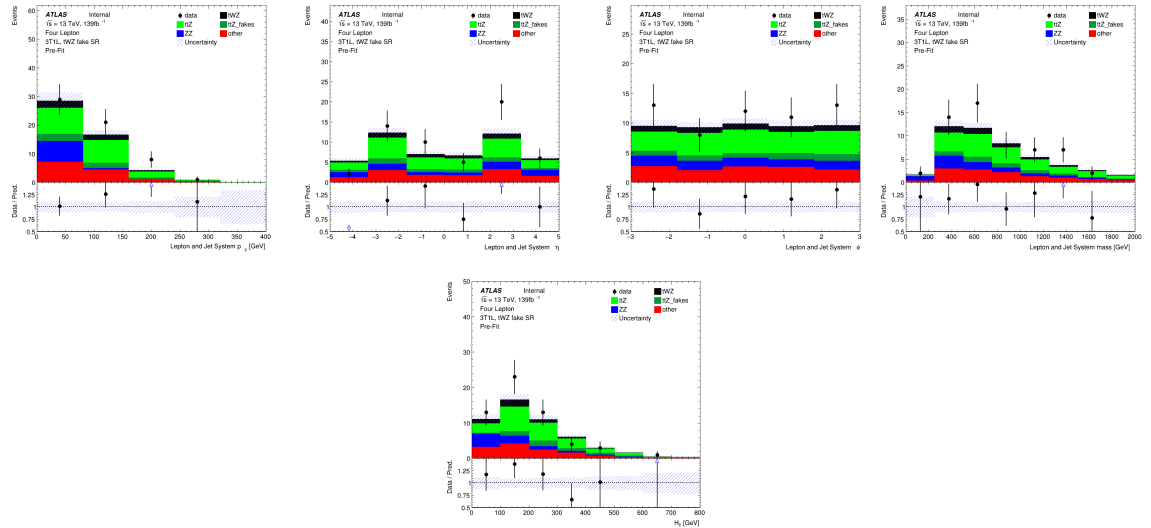


Figure A.64: MC predictions for p_T , η and ϕ (top row) and mass (bottom left) for the lepton + jet systems ($\ell\ell\ell\ell + \text{jets}$) in the $(tWZ)_{\text{fake}}$ CR region . Bottom right: MC predictions for H_T (scalar sum of jet p_T and lepton p_T) in the $(tWZ)_{\text{fake}}$ CR region

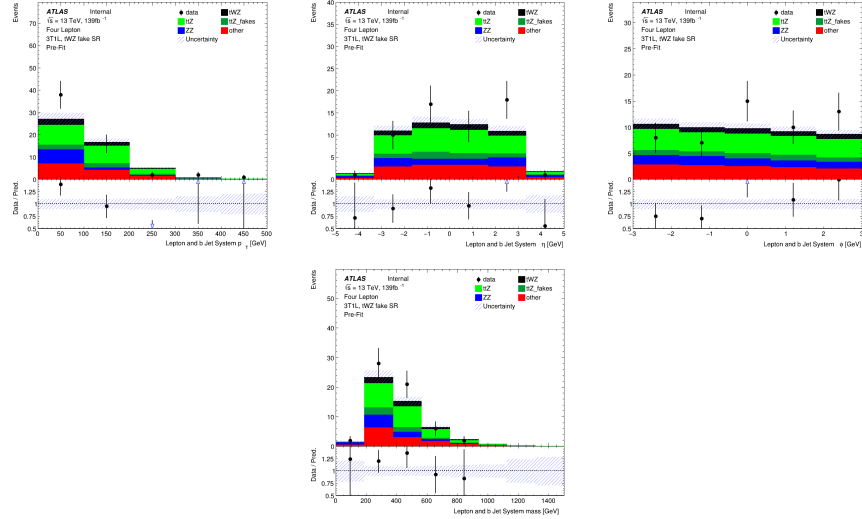


Figure A.65: MC predictions for p_T , η , ϕ (top row) and mass (bottom row) of the lepton + b-tagged jet systems ($\ell\ell\ell\ell + \text{b-tagged jets}$) in the $(tWZ)_\text{fake}$ CR region

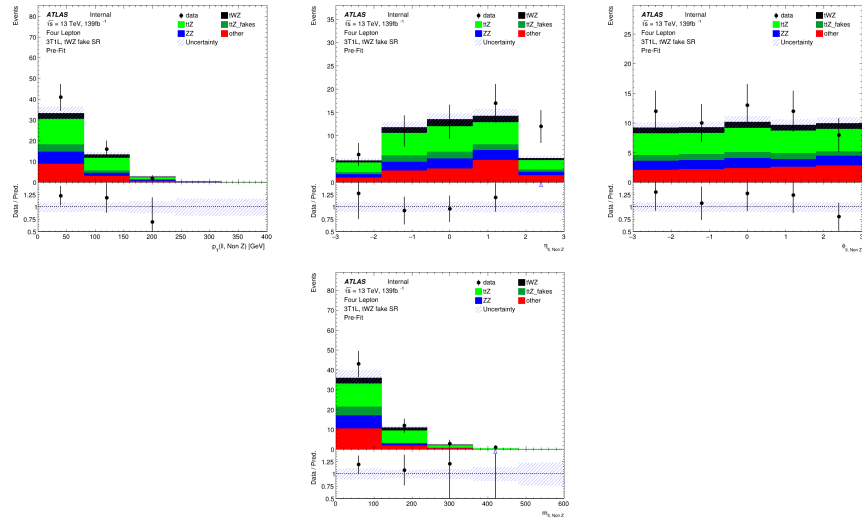


Figure A.66: MC predictions for p_T , η , ϕ (top row) and mass (bottom row) of reconstructed Non Z leptons (lepton pairs which don't originate from a Z candidate) in the $(tWZ)_\text{fake}$ CR region

Bibliography

- [1] M. Aaboud et al. “Electron reconstruction and identification in the ATLAS experiment using the 2015 and 2016 LHC proton–proton collision data at $\sqrt{s} = 13$ TeV”. In: *The European Physical Journal C* 79.8 (Aug. 2019). ISSN: 1434-6052. DOI: 10.1140/epjc/s10052-019-7140-6. URL: <http://dx.doi.org/10.1140/epjc/s10052-019-7140-6>.
- [2] M. Aaboud et al. “Measurement of the $t\bar{t}Z$ and $t\bar{t}W$ cross sections in proton-proton collisions at $\sqrt{s} = 13$ TeV with the ATLAS detector”. In: *Phys. Rev. D* 99 (7 Apr. 2019), p. 072009. DOI: 10.1103/PhysRevD.99.072009. URL: <https://link.aps.org/doi/10.1103/PhysRevD.99.072009>.
- [3] Aaboud, M. and Aad, G. and Abbott, B. and Abbott, D. C. and Abdinov, O. and Abed Abud, A. and Abhayasinghe, D. K. and Abidi, S. H. and AbouZeid, O. S. and et al. “Measurement of ZZ production in the $\ell\ell\nu\nu$ final state with the ATLAS detector in pp collisions at $s \sqrt{s} = 13$ TeV”. In: *Journal of High Energy Physics* 2019.10 (Oct. 2019). ISSN: 1029-8479. DOI: {10.1007/jhep10(2019)127}. URL: %7Bhttp://dx.doi.org/10.1007/JHEP10(2019)127%7D.
- [4] G. Aad et al. “Muon reconstruction performance of the ATLAS detector in proton–proton collision data at $\sqrt{s} = 13$ TeV”. In: *The European Physical Journal C* 76.5 (May 2016). ISSN: 1434-6052. DOI: 10.1140/epjc/s10052-016-4120-y. URL: <http://dx.doi.org/10.1140/epjc/s10052-016-4120-y>.
- [5] Shunichi Akatsuka and Shion Chen. *Isolation WPs summary: PLV + LowPtPLV*. Oct. 2019. URL: https://indico.cern.ch/event/854783/contributions/3595486/attachments/1929380/3195230/PLV_Summary.pdf.
- [6] ATLAS Collaboration. “ATLAS b -jet identification performance and efficiency measurement with $t\bar{t}$ events in pp collisions at $sqrts = 13$ TeV”. In: *Eur. Phys. J. C* 79 (2019), p. 970. DOI: 10.1140/epjc/s10052-019-7450-8. arXiv: 1907.05120 [hep-ex].
- [7] ATLAS Collaboration. *Calibration of light-flavour b -jet mistagging rates using ATLAS proton–proton collision data at $sqrts = 13$ TeV*. ATLAS-CONF-2018-006. 2018. URL: <https://cds.cern.ch/record/2314418>.
- [8] ATLAS Collaboration. “Electron and photon performance measurements with the ATLAS detector using the 2015–2017 LHC proton-proton collision data”. In: *JINST* 14 (2019), P12006. DOI: 10.1088/1748-0221/14/12/P12006. arXiv: 1908.00005 [hep-ex].
- [9] ATLAS Collaboration. “Identification and rejection of pile-up jets at high pseudorapidity with the ATLAS detector”. In: *Eur. Phys. J. C* 77 (2017), p. 580. DOI: 10.1140/epjc/s10052-017-5081-5. arXiv: 1705.02211 [hep-ex].
- [10] ATLAS Collaboration. *Measurement of b -tagging efficiency of c -jets in $t\bar{t}$ events using a likelihood approach with the ATLAS detector*. ATLAS-CONF-2018-001. 2018. URL: <https://cds.cern.ch/record/2306649>.
- [11] ATLAS Collaboration. “Measurements of b -jet tagging efficiency with the ATLAS detector using $t\bar{t}$ events at $sqrts = 13$ TeV, TeV”. In: *JHEP* 08 (2018), p. 089. DOI: 10.1007/JHEP08(2018)089. arXiv: 1805.01845 [hep-ex].
- [12] ATLAS Collaboration. “Muon reconstruction and identification efficiency in ATLAS using the full Run 2 pp collision data set at $sqrts = 13$ TeV”. In: (2020). arXiv: 2012.00578 [hep-ex].
- [13] ATLAS Internal. *Electron Efficiencies for Analyses*. 2021. URL: <https://twiki.cern.ch/twiki/bin/viewauth/AtlasProtected/ElectronEfficienciesForAnalysis>.
- [14] ATLAS Internal. *Electron Efficiency Correlation Model*. 2021. URL: <https://twiki.cern.ch/twiki/bin/view/AtlasProtected/ElectronEfficiencyCorrelationModel>.

- [15] ATLAS Internal. *Jet Vertex Tagger for Run 2 in reco and analysis*. 2021. URL: <https://twiki.cern.ch/twiki/bin/view/AtlasProtected/JetVertexTaggerTool>.
- [16] ATLAS Internal. *Muon Efficiencies for Analyses*. 2021. URL: <https://twiki.cern.ch/twiki/bin/view/AtlasProtected/MuonEfficienciesForAnalysis>.
- [17] G. Avoni et al. “The new LUCID-2 detector for luminosity measurement and monitoring in ATLAS”. In: *JINST* 13.07 (2018), P07017. DOI: 10.1088/1748-0221/13/07/P07017.
- [18] Thomas Calvet. *Automatic binning implementation in TTHFitter - Htop(bb)*. URL: https://indico.cern.ch/event/455289/contributions/1953694/attachments/1209081/1762963/Calvet_binning_Htop-160108.pdf.
- [19] CERN Yellow Reports: Monographs. *CERN Yellow Reports: Monographs, Vol. 10 (2020): High-Luminosity Large Hadron Collider (HL-LHC): Technical design report*. en. 2020. DOI: 10.23731/CYRM-2020-0010. URL: <https://e-publishing.cern.ch/index.php/CYRM/issue/view/127>.
- [20] Shion Chen. *Track isolation variable for the PFlow WPs*. Oct. 2019. URL: https://indico.cern.ch/event/854783/contributions/3595529/attachments/1926980/3190772/IFF_20191003_PflowWPs.pdf.
- [21] CMS Collaboration. *Measurements of $pp \rightarrow ZZ$ production cross sections and constraints on anomalous triple gauge couplings at $\sqrt{s} = 13$ TeV*. 2020. arXiv: {2009.01186} (hep-ex).
- [22] Federico Demartin et al. “tWH associated production at the LHC”. In: *Eur. Phys. J. C* 77.1 (2017), p. 34. DOI: 10.1140/epjc/s10052-017-4601-7. arXiv: 1607.05862 [hep-ph].
- [23] *Electron identification efficiency in data for electrons with $E_T > 30\text{GeV}$* . URL: https://atlas.web.cern.ch/Atlas/GROUPS/PHYSICS/PAPERS/EGAM-2018-01/fig_16.png.
- [24] Steve Farrell. *Overlap Removal Tools, FTAG/Hbb Workshop*. URL: https://indico.cern.ch/event/631313/contributions/2683959/attachments/1518878/2373377/Farrell_ORTools_ftaghbb.pdf.
- [25] *GoodRunListsForAnalysisRun2*. URL: <https://twiki.cern.ch/twiki/bin/viewauth/AtlasProtected/GoodRunListsForAnalysisRun2>.
- [26] Particle Data Group et al. “Review of Particle Physics”. In: *Progress of Theoretical and Experimental Physics* 2020.8 (Aug. 2020). 083C01. ISSN: 2050-3911. DOI: 10.1093/ptep/ptaa104. eprint: <https://academic.oup.com/ptep/article-pdf/2020/8/083C01/33653179/ptaa104.pdf>. URL: <https://doi.org/10.1093/ptep/ptaa104>.
- [27] *IFFTruthClassifier GitLab Repository*. URL: <https://gitlab.cern.ch/ATLAS-IFF/IFFTruthClassifier/-/tree/master>.
- [28] *IFFTruthClassifier Lepton Categories*. URL: <https://gitlab.cern.ch/ATLAS-IFF/IFFTruthClassifier/-/tree/master#3-details-about-the-lepton-categories>.
- [29] V. Khachatryan et al. “Measurement of the ZZ production cross section and $Z \rightarrow \ell^+\ell^-\ell^+\ell^-$ branching fraction in pp collisions at $\sqrt{s} = 13\text{TeV}$ ”. In: *Physics Letters B* 763 (2016), pp. 280–303. ISSN: 0370-2693. DOI: <https://doi.org/10.1016/j.physletb.2016.10.054>. URL: <https://www.sciencedirect.com/science/article/pii/S0370269316306256>.
- [30] Thomas McCarthy. *Macro developed to compare t/W/Z reconstruction performance (2ℓ , 3ℓ , 4ℓ)*. URL: https://indico.cern.ch/event/986357/contributions/4172907/attachments/2169451/3666801/reco_performance_macro_20210112.pdf.
- [31] Thomas McCarthy and Florian Fischer. *Exploiting full/partial $t\bar{t}$ reconstruction for background suppression in 2ℓ* . URL: https://indico.cern.ch/event/955360/contributions/4016465/attachments/2102418/3534816/top_reco_bkgd_suppression_2L_20200915.pdf.
- [32] *Monte Carlo to Monte Carlo scale factors for flavour tagging efficiency calibration*. Tech. rep. ATL-PHYS-PUB-2020-009. Geneva: CERN, May 2020. URL: <https://cds.cern.ch/record/2718610>.
- [33] *MuonSelectionTool, ATLAS TWiki*. URL: <https://twiki.cern.ch/twiki/bin/view/Atlas/MuonSelectionTool>.
- [34] O Oncel. *Search for Single Top Quark Production in Association with a W and a Z Boson in the 3 Lepton Final State with the ATLAS Experiment at 13 TeV*. URL: <https://cds.cern.ch/record/2625170>.
- [35] *Option to force a shape withing an error band by hand - TRF documentation*. URL: https://trexfitter-docs.web.cern.ch/trexfitter-docs/model_building/shape/.

- [36] *Pileup jet recommendations*. URL: <https://twiki.cern.ch/twiki/bin/view/AtlasProtected/PileupJetRecommendations>.
- [37] *Recommended isolation working points*. URL: <https://twiki.cern.ch/twiki/bin/view/AtlasProtected/RecommendedIsolationWPs>.
- [38] *Scikit-Learn GradientBoostingClassifier Documentation*. URL: <https://scikit-learn.org/stable/modules/generated/sklearn.ensemble.GradientBoostingClassifier.html>.
- [39] *TopRecoObjTwikiModel*. URL: <https://twiki.cern.ch/twiki/bin/view/AtlasProtected/TopRecoObjTwikiModel>.
- [40] *TRExFitter*. URL: <https://twiki.cern.ch/twiki/bin/viewauth/AtlasProtected/TtHFitter>.
- [41] *TRExFitter: Mixed data and MC fit*. URL: <https://trexfitter-docs.web.cern.ch/trexfitter-docs/AdvancedTutorial2020/Mixed/>.